



HAL
open science

On the long-term stability of foams: strength of an armored bubble and emergence of global disorder

Nicolas Taccoen

► **To cite this version:**

Nicolas Taccoen. On the long-term stability of foams: strength of an armored bubble and emergence of global disorder. *Soft Condensed Matter* [cond-mat.soft]. Ecole Doctorale de l'Ecole Polytechnique, 2015. English. NNT: . tel-01325134

HAL Id: tel-01325134

<https://hal.science/tel-01325134>

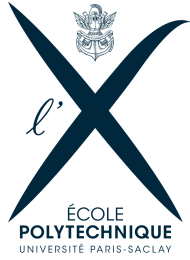
Submitted on 5 Jun 2016

HAL is a multi-disciplinary open access archive for the deposit and dissemination of scientific research documents, whether they are published or not. The documents may come from teaching and research institutions in France or abroad, or from public or private research centers.

L'archive ouverte pluridisciplinaire **HAL**, est destinée au dépôt et à la diffusion de documents scientifiques de niveau recherche, publiés ou non, émanant des établissements d'enseignement et de recherche français ou étrangers, des laboratoires publics ou privés.



Distributed under a Creative Commons Attribution - NonCommercial 4.0 International License



École Polytechnique
Laboratoire d'Hydrodynamique

Thèse présentée pour obtenir le grade de
DOCTEUR DE L'ÉCOLE POLYTECHNIQUE

Spécialité : Mécanique

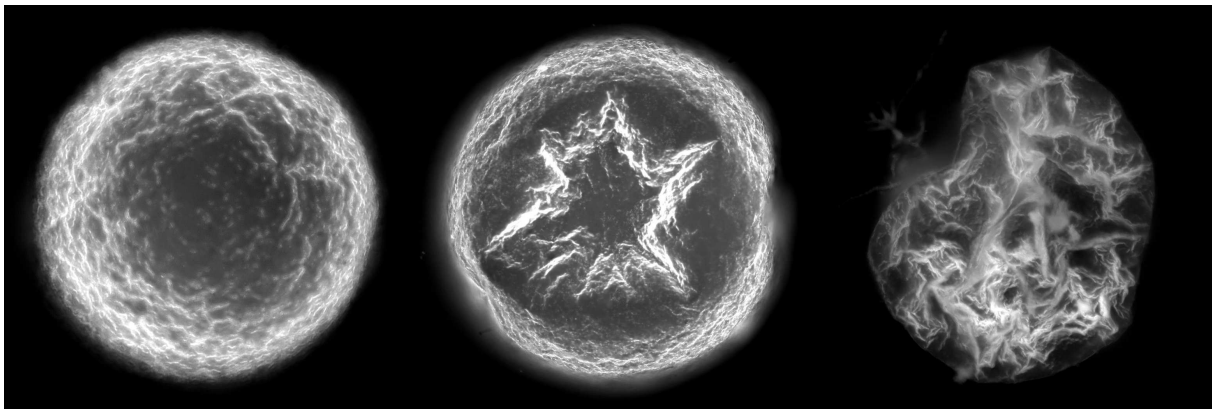
par

Nicolas Taccoen

On the long-term stability of foams: strength of an armored bubble and emergence of global disorder

Thèse soutenue le 4 décembre 2015 devant le jury composé de

Manouk Abkarian	rapporteur	Université de Montpellier 2
Élise Lorenceau	rapporteur	Université Paris-Est
Marie-Caroline Jullien	examinateur	ESPCI ParisTech
François Graner	président	Université Paris 7
Deniz Z. Gunes	invité	Nestlé Research Center
Charles N. Baroud	directeur de thèse	École Polytechnique



On the long-term stability of foams: strength of an armored bubble and emergence of global disorder

Nicolas Taccoen

The image on cover shows epifluorescence micrographs of air-in-water bubbles coated with an armor of fluorescent polystyrene particles (\varnothing 500 nm). The radii of these bubbles is about $100 \mu\text{m}$. The left one is spherical, the middle one has undergone buckling, and the right one is completely crumpled. More details can be found in section [3.2](#) of this thesis.

Résumé

Une mousse est un ensemble de bulles de gaz, enchâssées dans une matrice continue. Elles sont omniprésentes dans de nombreux domaines industriels. En agro-alimentaire, une crème glacée peut contenir jusqu'à 30% d'air, ce qui donne au produit sa texture aérienne et onctueuse. Mousseur un produit cosmétique altère sa rhéologie, lui permettant de mieux s'appliquer sur la peau. Le volume apparent est aussi augmenté, limitant ainsi le gaspillage de produit. Incorporer de l'air dans un matériaux de construction lui confère d'excellentes propriétés d'isolation thermique et acoustique, tout en l'allégeant et en réduisant son coût. Néanmoins, les bulles composant une mousse sont des objets dynamiques, pour lesquels il n'existe pas d'état d'équilibre. Soit elles gonflent, soit elles se dissolvent et disparaissent, mais elles ne peuvent pas rester stationnaires. Ceci est à l'origine d'un processus de déstabilisation des mousses, dans lequel le gaz des petites bulles diffuse dans les plus grosses. Ce phénomène, appelé mûrissement d'Ostwald (MO), explique en partie la faible durée de vie des mousses. La première partie de cette thèse s'attache à comprendre fondamentalement les mécanismes physiques expliquant la stabilisation des mousses par des particules solides, une méthode éprouvée pour bloquer le MO. Nous réduisons l'étude de la mousse à celle d'une unique bulle sphérique, couverte d'une monocouche de particules colloïdales. L'environnement de la bulle au sein de la mousse est simulé en variant la pression autour d'elle, tout en observant son comportement. Il apparaît que l'armure colloïdale est capable de bloquer la dissolution du gaz jusqu'à une certaine pression seuil, au delà de laquelle la coque s'effondre. Ce flambage est initié par des dislocations locales et provoque la dissolution complète de la bulle. La pression seuil de rupture varie avec le rayon R de la bulle selon $\Delta P_{collapse} \propto R^{-1}$, mais ne dépend pas du diamètre des particules. Ces résultats sont en désaccord avec la théorie élastique généralement utilisée pour décrire les interfaces couvertes. Nous proposons donc un nouveau modèle, fondé sur un équilibre énergétique entre le gain de dissolution du gaz, et le coût capillaire de déplacement individuel des particules à l'interface. Ce modèle prédit bien le comportement de $\Delta P_{collapse}$, son insensibilité à la taille des particules, et l'apparition des dislocations locales. Enfin, nous appliquons cette nouvelle compréhension microscopique à un modèle classique de MO, montrant ainsi que dans une mousse particulaire, les plus petites bulles se dissolvent, car la résistance de l'armure augmente moins vite que la contrainte imposée par la mousse environnante. Le dispositif expérimental et le cadre théorique peuvent être appliqués à des particules et des armures plus complexes. Dans la seconde partie du travail, nous prenons du recul afin d'observer la déstabilisation par MO d'une mousse monodisperse stabilisée par un tensioactif. Il s'agit d'une mousse modèle constituée d'une monocouche de bulles arrangées en réseau hexagonal 2D, dans une puce microfluidique. Environ 30'000 bulles peuvent ainsi être suivies individuellement. La mousse initialement monodisperse se déstabilise vers un état polydisperse, autosimilaire, comme la théorie classique le prédit. Nous allons plus loin en classifiant les bulles en deux populations, une désordonnée, et une ordonnée, qui conserve l'ordre cristallin hexagonal initial. La transition vers le désordre peut ainsi être vue comme la succession de deux processus: (i) nucléation-croissance de zones de désordre qui envahissent progressivement la mousse, (ii) évolution homogène vers l'autosimilarité. Un modèle est enfin développé pour rendre compte de la vitesse d'invasion du désordre. Ces deux approches fournissent de précieuses informations utiles à la conception de mousse particulières, tant au niveau d'une bulle qu'à l'échelle macroscopique de la mousse.

Mots clés : interface, microfluidique, colloïde, mousse, bulle, mûrissement

Abstract

A foam consists in a collection of gas bubbles, embedded in a continuous matrix. Their uses are numerous and they are ubiquitous in various industrial domains. In food products, ice-creams incorporate up to 30% of air bubbles, which gives the product an aerated, smooth, creamy texture. In cosmetics, foaming a product changes its rheology, thickening it for a better feel on the skin. It also increases the apparent volume, limiting waste. In construction, a foamed material offers superior heat and acoustic insulation, while being lightweight and cheap. However, the bubbles composing the foam are dynamic objects that cannot exist in an equilibrium state. They either grow and rise or shrink and disappear, but they cannot stay stationary. This is at the origin of a coarsening process in which the gas of small bubbles diffuses to larger ones. Called Ostwald ripening (OR), it partly explains the relatively short life expectancy of foams. In the first part of this thesis, new insight is gained on the fundamental physical processes at the origin of the stabilisation of foams by solid particles, a method that has been proved to block OR. We reduce the problem of foam stability to the study of the behavior of one single spherical bubble coated with a monolayer of particles. The behavior of this armored bubble is monitored while the ambient pressure around it is varied, in order to simulate the dissolution stress resulting from the surrounding foam. We find that the colloidal shell is able to block the dissolution up to a critical stress after which it buckles. This collapse is triggered by local dislocations and leads to the complete dissolution of the bubble. The critical value of the ambient pressure that leads to the failure depends on the bubble radius, with a scaling of $\Delta P_{collapse} \propto R^{-1}$, but does not depend on the particle diameter. These results disagree with the elastic models generally used to describe particle-covered interfaces. Instead, the experimental measurements are accounted for by an original theoretical description that equilibrates the energy gained from the gas dissolution with the capillary energy cost of displacing the individual particles. The model recovers the short-wavelength instability, the scaling of $\Delta P_{collapse}$, and the insensitivity to particle diameter. Finally, we use this new microscopic understanding to predict the aging of particle-stabilised foams, by applying a classical OR model. We find that the smallest armored bubbles should fail, as the dissolution stress on these bubbles increases more rapidly than the armor strength. Both the experimental and theoretical results can readily be generalized to more complex particle interactions and shell structures. In the second part of the work, we take a step back and observe the destabilisation through OR of a monodisperse foam, stabilized only with surfactant. This model foam consists in a monolayer of bubbles, arranged in a 2D hexagonal lattice, in a microfluidic chamber. The setup allows for the individual localisation and radius measurement of all the $\approx 30'000$ bubbles of the foam. The initially monodisperse foam undergoes a transition and destabilizes toward a polydisperse self-similar state, as predicted by standard theory. Our setup allows a more detailed description of the transition, by classifying the bubbles into a disordered population and an ordered one, retaining the initial crystalline hexagonal order. We break down the global foam transition into two successive processes. First, disorder regions randomly nucleate and grow, progressively invading the foam, then the disorder homogeneously increases until the self-similar regime is reached. We also develop a model to describe the growth rate of disorder. These two complementary approaches yield valuable informations, useful for the engineering of stable foams, both at the microscale of a single bubble, and at the macroscale of the foam.

Key words: interface, microfluidic, colloid, foam, bubble, ripening

Remerciements

Au début de la réalisation de ce doctorat, en septembre 2012, j'avais dans l'idée qu'un travail de thèse devait se commencer sans en connaître la fin à l'avance. Je remercie donc en premier lieu Charles, pour m'avoir guidé et formé tout au long de ce chemin de recherche, qui a finalement abouti au présent manuscrit, dont nous n'avions effectivement pas prévu le contenu à l'époque.

Je remercie ensuite Caroline, qui m'a appris toutes les bases des techniques expérimentales dont je me suis servie ces trois dernières années, et qui n'a pas cessé de m'aider pour nombre d'expériences.

Je remercie également Etienne et Rémi, qui m'ont accueilli au labo et montré nombres de ficelles microfluidiques, et m'ont plus tard permis de découvrir les coulisses de la naissance d'une startup de biotechnologie, avec Clément, Magali et Barbara.

Je remercie ensuite tous les membres de l'équipe (récemment rebaptisée $P\mu B$): Gabriel, Raphaël, Cyprien, Sébastien, Micaela, Morgane et Irma, pour la stimulation et la motivation qu'ils m'ont apporté, par leur bonne humeur mais aussi par les excellentes discussions scientifiques.

Je n'oublie pas non plus les stagiaires qui m'ont accompagné quelques temps, avec qui j'ai eu plaisir à travailler: Jean-Phillipe, Loris et Elie.

Je remercie aussi tous ceux sans qui l'activité du LadHyX ne serait pas possible, et qui m'ont tous aidé au quotidien: Sandrine, Thérèse, Delphine, Magali, Dany, Toaï et Antoine.

Je remercie également ceux avec qui j'ai eu la chance de collaborer : Deniz Gunes, qui a apporté le point de vue industriel de Nestlé et a su voir l'intérêt potentiel de ces petites bulles armurées ; Benjamin Dollet, pour ses connaissances inépuisables sur la complexe physique des mousses ; et François Lequeux, pour son aide précieuse sur la modélisation de ce que nous avons observé. Et bien entendu, je remercie mon Jury de thèse, pour avoir accepté d'évaluer mon travail, et pour la discussion animée qui a suivi ma soutenance.

Je remercie enfin tous les membres du LadHyX pour l'ambiance inimitable de convivialité et d'émulation scientifique qui y règne, et qui ont rendu cette période de thèse agréable. J'ajoute une mention spéciale à Avin et Julien, qui ont toujours su m'aider et m'orienter, et avec qui il était toujours sympathique de discuter. J'ajoute une deuxième

mention spéciale à Gaétan, Timothée, Manu, Camille et Romain, pour les projets que l'on qualifiera "d'annexes" au travail de recherche à proprement parler, tels que l'escalade, la course en forêt, et les usinages et bricolages en tous genres.

J'ai également une pensée pour tous mes amis qui ont eu la chance de rédiger leur thèse en même temps que moi, et avec qui il était facile d'en discuter les déboires. Je pense en particulier au groupe 14 ; à Léopold et Hugo, qui m'ont accueilli dans leurs labos parisiens les derniers week-end où l'X semblait beaucoup trop loin ; mais aussi à Eunok, Matthieu et Chakri, avec qui nous avons fortement ralenti l'activité du LadHyX en soutenant tous les quatre la même semaine.

Finalement, je remercie mes parents et mon frère, pour m'avoir soutenu pendant ces trois années, et surtout de s'être intéressé à ce sur quoi je travaillais, ainsi que pour l'intendance du pot de thèse.

Enfin, je remercie Celia, pour la relecture attentive de ce manuscrit, et pour sa présence pendant ces années de thèse.

Je vous souhaite une excellente lecture.

Contents

Introduction	1
I Mechanical strength of an armored bubble	7
1 Context	9
1.1 Trapping of a solid particle on an interface	9
1.2 What is the elasticity of particle coated interfaces ?	11
1.3 Adsorption of particles on gas-in-liquid bubbles.	12
1.4 Particle stabilized foams	13
1.5 Open questions and contribution of this thesis	16
1.6 Outline of Part I	16
2 Materials and Methods	17
2.1 Fabrication of the microfluidic chip	17
2.1.1 Conventional soft lithography	17
2.1.2 Micromachining of a mold	18
2.1.3 Surface state of the channel	21
2.2 Production of a single air bubble by gradient of confinement	22
2.3 Particles	24
2.3.1 Colloidal beads used	24
2.3.2 Fabrication of ellipsoidal particles	24
2.4 Imaging and control	25
3 Experiments with armored bubbles	27
3.1 Producing and monitoring an armored bubble in microfluidics	27
3.1.1 Covering the air bubble	29
3.1.2 Trapping and monitoring the bubble	33
3.2 Measurement of armor resistance	35

3.2.1	Progression of a typical experiment	36
3.2.2	Buckling of the armor	37
3.2.3	Mechanical strength characterization of armors	38
3.2.4	Onset of buckling	40
3.2.5	Bubble inflation and cracks opening	43
3.3	Armor with ellipsoidal colloids	44
3.4	Effect of surfactant on armor strength	45
3.4.1	Effect of surfactant on the failure mode of the shell	45
3.4.2	Effect of SDS concentration	46
3.4.3	Possible interpretation	46
4	Interpretation of the behavior of colloidal armors	51
4.1	Control of the bubble dissolution	52
4.1.1	Gibbs theory of bubble nucleation	52
4.1.2	Calculation of R_{eq}	53
4.1.3	Expression of the free energy of the dissolving bubble	55
4.2	Comparison to models of elastic shell	57
4.3	Modeling the armor behavior	58
4.3.1	Dissolution energy	58
4.3.2	Shell deformation energy	59
4.4	Synthesis and model final prediction	62
4.5	Prediction of the behavior of the armor within a foam	64
4.5.1	Lemlich model	64
4.5.2	Comparison with armor strength	66
5	Outlooks	71
5.1	Connection to other studies	71
5.2	Perspectives	75
5.2.1	Explore more complex shells	75
5.2.2	Deepen the understanding of the coverage	76
5.3	Conclusion	77
II	Emergence of disorder in a monodisperse foam	79
6	Monodisperse foam coarsening	81

7	Setup and experimental procedure	85
7.1	Microfluidic device	85
7.2	Experimental procedure	87
7.3	Image analysis	88
8	Nucleation and growth of disorder	91
8.1	Aging of a monodisperse foam	92
8.2	Long-time regime	93
8.3	Order-disorder transition	94
8.4	Classification in 2 sub-populations	95
8.5	Characterisation of the bubbles subsets	97
8.6	Model of the disorder invasion	103
	8.6.1 Constant invasion rate	103
	8.6.2 Variable invasion rate	104
8.7	Conclusion	109
9	Future work	111
9.1	Single bubble tracking	111
9.2	Induced defect	113
9.3	Grain boundary	113
9.4	Further experiments	114
	General conclusion	119
	Bibliography	122

Introduction

In January 2013, the city of Caloundra, on the Sunshine Coast near Brisbane in Australia, was submerged by a flood of sea foam that completely filled the streets (figure 1). The city was paralyzed by this unusual phenomenon for several days. The origin of this huge amount of froth is unclear, but it was the consequence of the conjunction of strong winds, and the presence in the sea water of certain types of plankton, that produced a particularly stable and abundant foam.



Figure 1: The streets of Caloundra under several meters of sea foam. Source: ITN News

Nevertheless, foams do not usually cause so much problems, but rather have a lot of interesting properties that are exploited in various applications. For instance, one of the most common places where to find foams is in the bathroom. A foamy soap or shampoo provides confort and pleasure to the user, but it also increases the surface of skin that can be covered with a given amount of product. This covering capability is linked to the rheological properties of foams: they are yield stress fluids that can stay on a surface unless submitted to a shear stress [1], as for instance in the case of shaving foam on the cheeks, before it is swept away by the razor's blade. This property is put to good use in other domains, such as chemical or radioactive decontamination. Once foamed, the decontamination solution can efficiently coat the surfaces to treat, and act

for a longer time. Finally, the thermal insulation qualities of foams can be combined with their rheology when used as firefighting foams. Indeed, a foamed fire extinguishing agent has a double effect: by coating the fuel, the foam insulates it from the heat source and cuts the fire's oxygen supply (see figure 2).



Figure 2: A fire extinguishing foam used on a burning hydrocarbon tank. Foams are particularly useful in that case since they cover the liquid fuel, rather than sinking into it, as water would do. Photo: Mattias Georgsson.

A lot of foams are also edible. These food foams are often associated with beverages such as cider, beer or soda. The dissolved CO_2 they contain nucleates into bubbles as the pressure drops when the container is opened. The bubbles rise and form a foam at the top of the glass, which is a part of the consumer's experience. But a variety of other products are also aerated [2], because the presence of air bubbles in a culinary preparation brings a sensation of lightness and onctuousity. This is especially true in ice-creams, where the size and the repartition of air bubbles in the frozen mix determines the texture of the ice-cream [3]. Furthermore, foamed food presents advantages not only for the consumer, but also for the producer, who can control the cost of a given volume of product: the air introduced in the preparation is free (however, the process to introduce the bubbles in the preparation is not).

Foams can also be found in the walls of buildings. Indeed introducing air bubbles in construction materials such as concrete is a process that has been known for a long time [4]. As for food products, introducing air bubbles within concrete or cement lower the production cost, but it also greatly reduces the density of the material, to such a

point that it is possible to make concrete float (see figure 3(b)). Moreover, the presence of air in the material strongly reduces its thermal conductivity, in comparison with that of conventional concrete. This enhanced thermal insulation is one of the main selling points for cellular concrete (see figure 3(a)). Research on this type of material is still a topical subject, in order to achieve controlled structures and bubble sizes [5].

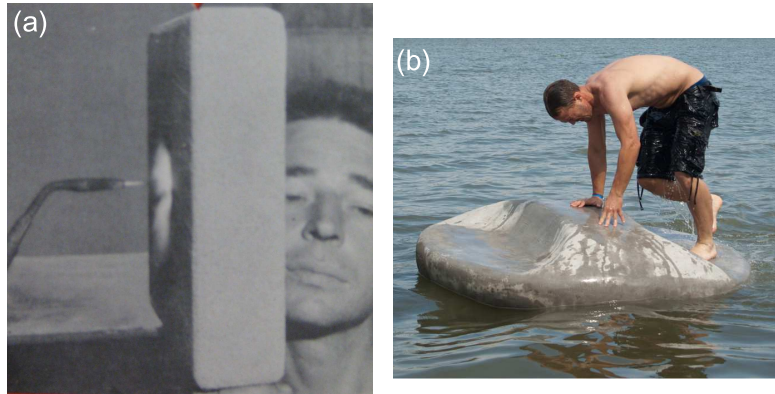


Figure 3: **(a)** 1950 advertisement for the Thermo-Con cellular concrete [4]. It demonstrates the thermal insulation capability of foamed concrete: a person can press his cheek (without apparent burn) against a slab of concrete, the other side of which being heated with a blow-torch. **(b)** Floating concrete island (AB Concrete Design)

Finally, exotic materials can be obtained by introducing gas bubbles into molten aluminium. Once the metal solidifies, one obtains a porous structure similar to that of a sponge [6]. This material is very lightweight, and has very good shock absorption capabilities, similarly to the polystyrene foam used in bike helmets. The energy of the projectile is very efficiently dissipated in the metallic foam, because of its highly tortuous structure. These materials are very promising for aerospace applications (see figure 4).

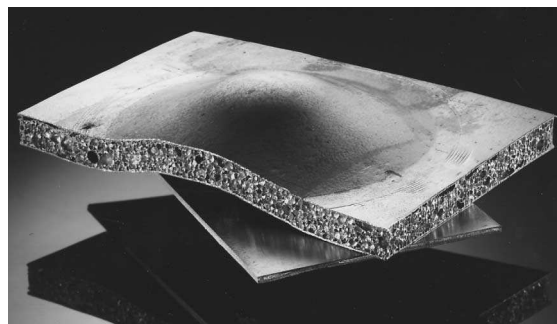


Figure 4: An aluminium foam sandwiched between two steel panels. This structure is manufactured by Fraunhofer and Studiengesellschaft Stahlanwendungen.

Given these numerous applications, the stability of a foam against aging is therefore

a major issue, since it determines the ability to control the material properties and their evolution in time. Foams suffer from three major aging processes [7] that alter their structure over time.

Firstly, foams are dispersions of gas bubbles in liquids. In pure water for example, when two gas bubbles come into contact, they merge together to reduce their total interfacial energy. This is known as coalescence, and it is the first destabilisation process of a foam. It can be easily prevented by dissolving surfactant molecules in the liquid. These molecules are amphiphilic, which means they are composed of a molecular head that is hydrophilic, attached to a molecular chain, the tail, that is hydrophobic. In consequence, these molecules adsorb on the air-water interface to satisfy their ambivalent nature. Bubbles whose interfaces are coated with surfactant cannot coalesce because the polar heads of the surfactant at their surfaces repulse each other. This repulsion can be steric or electrostatic, and its magnitude defines the stabilizing power of the surfactant.

The second aging process of a foam is drainage. It is due to the density contrast between the gas and the liquid. By buoyancy, the bubbles tend to rise and the liquid tends to flow toward the bottom of the foam. The liquid films separating the bubbles near the top of the foam are thus progressively depleted and may rupture if they become too thin. This can be prevented by using surfactant whose heads show a strong enough repulsion to stop the film thinning, or by increasing the viscosity of the fluid to slow down the drainage.

Finally, gas can be transferred by diffusion from, small bubbles to larger ones. This transfer is due to the Laplace pressure difference existing between bubbles of different sizes. In consequence, small bubbles, where pressure is higher, become smaller and large bubbles, where pressure is lower, become larger. This phenomenon leads to the coarsening and destabilization of the foam. This last process is known as Ostwald ripening. It is the slowest of the three aging processes, because it is driven by diffusion, but also the most difficult to counteract. Indeed, gas diffuses through the surfactant layer, and cannot be stopped.

Solid foams are of course not affected by these problems, since their continuous matrix is rigid. However, most of the time, solid foams are created by solidification of a liquid foam. That is why, even if the final material is a solid foam, it is important to control the foam aging.

In this thesis, we are more particularly interested in Ostwald ripening. We will tackle this issue in two ways: firstly, by shedding light on a well known, but still not completely understood, method to block Ostwald ripening, and secondly by unraveling the complex gas exchanges that take place between bubbles during the ripening of a foam.

In the first part, I will focus on foam stabilized by solid particles. It is well known

that coating the bubbles constituting a foam with an armor of solid particles is a very efficient way to block Ostwald ripening [8, 9]. The particles armor provides some rigidity to the interface, which blocks the shrinkage of the bubbles. However, the mechanical properties of these colloidal-armor remain mysterious, since it is difficult to observe and probe such tiny (typically $100 \mu m$) objects precisely. I will demonstrate an experimental microfluidic setup that enables both the production of a single armored bubble, and its trapping in a controlled environment, for an extended monitoring of its behavior. The quantitative measurements obtained show the unusual mechanical properties of armored bubbles, that are accounted for by a model that we develop.

In the second part, I will take a step back and present a detailed analysis of the first instants of the coarsening of a monodisperse foam. Indeed, the long time regime of Ostwald ripening are well described in the literature [10, 11]. In particular, the evolution of the bubbles size distribution is well known. However, the transient regime that leads to this final state when the initial state is monodisperse (ie. all the bubbles have the same size) is less understood. I will show that the transition is characterized by a nucleation-growth process of disordered zones, in the initially very ordered foam. The growth speed is measured, and described by a theoretical model, which gives a complete view of the evolution of the structure of the foam during the initiation of Ostwald ripening.

Part I

Mechanical strength of an armored bubble

1

Context

In this chapter, we present the background knowledge on systems involving solid particles and fluid interfaces separating two phases (gas or liquid). Firstly, the mechanism of particle adsorption on an interface is explained. Secondly we focus on the state-of-the-art in terms of characterization of planar interfaces coated with those adsorbed particles. Secondly, we present the work done on armored bubbles, as well as the questions that remain open. Finally, we turn our attention to the ability of adsorbed particles to stabilize liquid foams.

1.1 Trapping of a solid particle on an interface

The first quantitative analysis of colloidal particles adsorbed on a fluid interface was reported by P. Pieranski, in an article from 1980 [12]. Motivated by the recent progress made in two-dimensional phase transition, the aim of the study was to find an experimental system in which the crystalline order of particles, arranged in a 2D lattice, could be directly observed. The idea was to trap a collection of microscopic particles (\varnothing 246 nm) at a flat air-water interface. The arrangement of the colloids was thus constrained in a 2D plane. The author showed for the first time that the adsorbing energy of a microscopic bead on a fluid interface was orders of magnitudes higher than the thermal

agitation, which justified the use of the term 'trap'. More precisely, he calculated the surface energy E_γ of a partially wetted particle, piercing the interface, as a function of the depth of penetration z of the particle:

$$E_\gamma = \pi a z (\gamma_{sv} - \gamma_{sl} - \gamma_{lv}) + \pi z^2 \gamma_{lv}, \quad (1.1)$$

where γ_{sv}, γ_{sl} and γ_{lv} are the surface energies respectively of the solid-vapor, solid-liquid and liquid-vapor interfaces, and a is the radius of the particle.

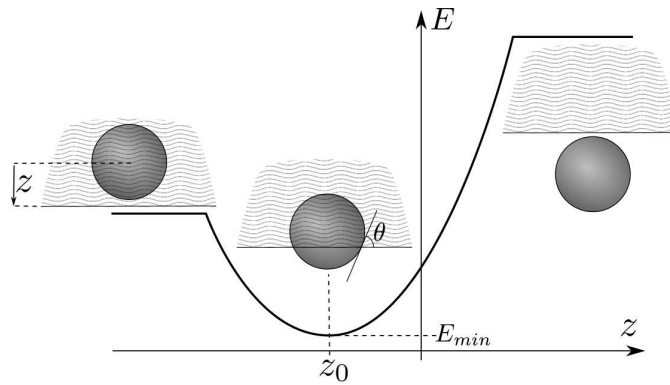


Figure 1.1: Energy profile of a bead adsorbed on a fluid interface, as a function of its depth of penetration z .

This energy is plotted in figure 1.1. It has a parabolic shape, with a minimum for a certain depth of penetration. This equilibrium position corresponds to the case when the interface intersects the solid sphere with the solid-liquid Young-Dupré contact angle θ . The order of magnitude of the energy required to pull the particle out of the energy well is $(1 - \cos \theta)^2 \gamma a^2$. In the most favorable case of $\theta = 90^\circ$, and for a $1 \mu m$ particle adsorbed on an air water interface, the desorption energy is $\approx 7^{-14}$ J, which is 10^7 higher than the thermal energy kT at $25^\circ C$. This proves that the particles are irreversibly adsorbed on the interface, so that they can only move in-plane.

This strong attachment of partially wetting particles on the interface is at the origin of all the work on particle covered interfaces. When the interface becomes too crowded with particles, and since they cannot desorb from the interface, the nature of the interface changes. Due to the solid nature of the particles, a particle-laden interface under compression cannot freely decrease its surface area anymore, although it must comply with the externally imposed deformation. The way it does so has been the starting question of several studies, the first one being:

1.2 What is the elasticity of particle coated interfaces ?

One way to measure the properties of these interfaces is to use a Langmuir trough, a conventional method to measure the interfacial elasticity properties of surfactants. It consists of a tank filled with liquid, one boundary of which is mobile. The interfacial area can thus be modified, compressing the layer of grain adsorbed on the interface. The first reported experiment with particles was done by Sheppard *et al.* in 1967 [13], but three decades passed until other groups started to recently tackle this problem again [14, 15, 16]. These studies describe the buckling of a layer of particles sprinkled on a water surface. The experimental setup is sketched in figure 1.2(a). As the layer is compressed, the particles are progressively more and more packed, and they finally jam at some point. If the layer is further compressed beyond jamming, it undergoes a buckling transition, wrinkles and undulations appear, as shown on figure 1.2. This layer morphology can be found both in the case of air-water interface [15] and oil-water interface [14], and for particles of various sizes.

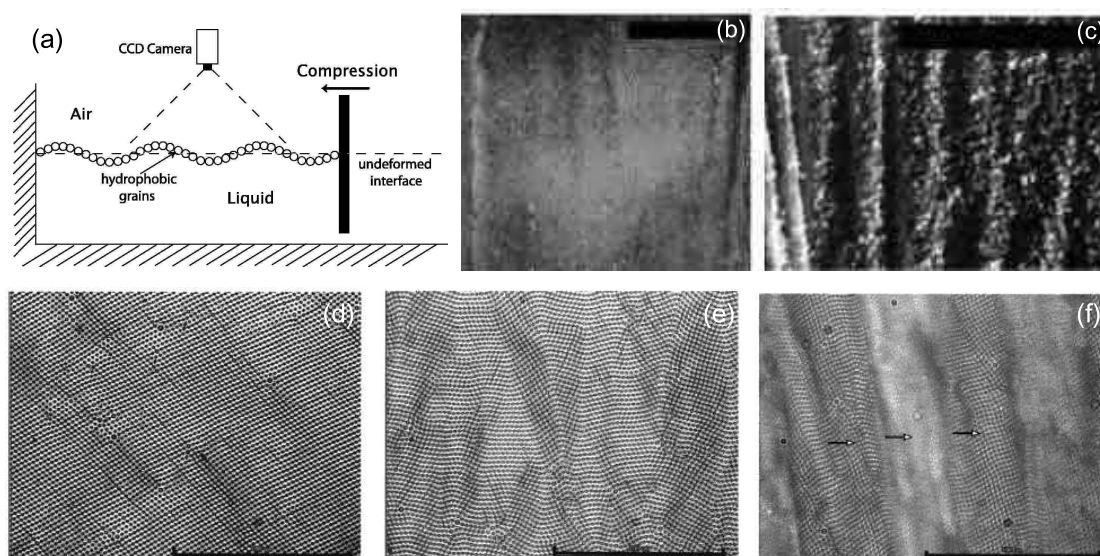


Figure 1.2: (a) Scheme of the Langmuir trough experiment with a monolayer of adsorbed grains. (b) Polystyrene particles with mean diameter $300\mu m$ and (c) lycopodium particles with mean diameter $30\mu m$ on an air water interface. Scale bars are 5mm. Adapted from [15]. (d-f) Increasing compression of a layer of polystyrene particles with mean diameter $2.6\mu m$, at an octane/water interface. Scale bars are $100\mu m$. Adapted from [14].

These experiments reveal the solid-like nature of particle-laden interfaces. The analysis carried out by Vella *et al.* [15] uses an elastic analogy to link the wavelength of the

buckling patterns to an equivalent elastic modulus of the composite material realised by the capillary trapped beads. This apparent young modulus E_γ scales like γ/a , a being the radius of the particles, an expression which fits well their experimental data. However, a crucial assumption of the model is that the weight of the liquid underneath the granular layer provides the restoring force that prevents it from deforming. The elasticity of the material thus arises from gravity, which render this model unable to describe a gravity-free case. For instance bubbles encountered in usual foams are typically much smaller than the capillary length. They are thus spherical and the effects of gravity are negligible at the scale of a single bubble.

1.3 Adsorption of particles on gas-in-liquid bubbles.

The first observation of a particle-stabilized air-in-water bubble is attributed to Walter Ramsden in 1903 [17]. He describes the crystallisation of certain proteins and organic molecules at an air-water interface. The interface of the bubble is thus covered either with a rather continuous film as in the case of albumin, or a granular layer, as in the case of saponin (a class of surfactant molecule found in certain plants). In both cases, he describes both the solid like properties and elastic nature of the covered interface:

Bubbles of solution of egg-albumin, caseinogen and saponin exhibit remarkable phenomena, which show that the bubble-film as a whole is very imperfectly elastic and is covered with solid membranes. Egg-albumin are deformed on collapse by the formation of persistent folds of solid proteid in the bubble-film. Bubbles of pure saponin solution, containing 0.01 per cent. or more of saponin, fall on collapse into innumerable shimmering folds containing isolated curved rods of solid saponin, [...]. The collapsing bubble assumes extraordinary shapes, with sharp angles [...]. Walter Ramsden, 1903 [17]

The author already noticed the wrinkling of the coated interface in the case of a granular coating of solid saponin particles. This wrinkling and folding gives rise to unusual bubble shapes, a photography of which is unfortunately not available in the original paper.

Recently, there has been a regain of interest for these objects, thanks in part to the rise of new experimental techniques. Indeed, a method of choice for the study of these kind of small objects is to use microfluidic techniques. Subramaniam *et al.* [18] designed an elegant microfluidic chip on which a flow-focusing geometry used at high flowrate give the particles a sufficient speed to force their adsorption on the air-water interface. The interface is thus progressively coated, and an armored bubble periodically detaches from the air thread when enough particles packed at the tip of the thread (see figure 1.3).

Another approach was used by Park *et al.* [19], who took advantage of a chemical modification of the particles surface. They used particles made of a copolymer of polystyrene and polyacrylic acid. The later carries carboxylic acid groups which take an ionic carboxylate form at high pH, and a neutral carboxylic acid form at high pH. The principle of the armor assembly is thus to disperse the particle in a basic solution, to ensure a good dispersion of the particles while their surface is charged by the carboxylate groups. Pure CO₂ bubbles are then injected via a T-junction in the microchannel. This gas is very soluble in water, and its dissolution rapidly decreases the pH of the solution in the proximity of the bubble. Consequently, the carboxylate groups are protonated and lose their ionic character, which renders the beads surface more hydrophobic, promoting their adsorption at the gas-liquid interface. This method enables the serial production of monodisperse armored bubbles, but is limited to certain combinations of gas and particles chemistry.

Subramaniam *et al.* used their microfluidic production device to investigate the properties of armored bubbles in another article [20]. Notably, they showed that a stress applied on the shell can induce a plastic rearrangement of the beads, so that the bubble takes and maintain a non spherical shape.

The capacity of armors to block the dissolution of the gas inside the bubble was studied by Abkarian *et al.* , experimentally and numerically [21]. The authors observed the dissolution of armored bubbles submersed in degased water. While bare bubbles rapidly dissolve, the dissolution of armored ones is blocked, and the colloidal shell deforms under the subsequent 'dissolution pressure' (this term is explained in detail in the next chapter). The wrinkled shapes observed by Ramsden appear when the particles are significantly smaller than the bubble, while a faceting of the armor is observed when $a/R \approx 0.1$, R being the radius of the bubble (see figure 1.4).

Other groups have investigated the mechanical properties of spherical particle-laden interfaces, but in the case of liquid droplets, as surrogates for gas bubbles [22, 16, 23, 24, 25].

1.4 Particle stabilized foams

The ability of the colloidal shell to arrest gas dissolution is at the origin of the outstanding stability of particle-stabilized foams. The gas dissolves until the particles jam, preventing the bubble within the foam from decreasing their volume, thus blocking Ostwald ripening.

Substituting the usual surfactant with solid particles thus increases the lifetime of foams, which have lead numerous groups to study these systems [26, 27, 28, 29, 30, 31].

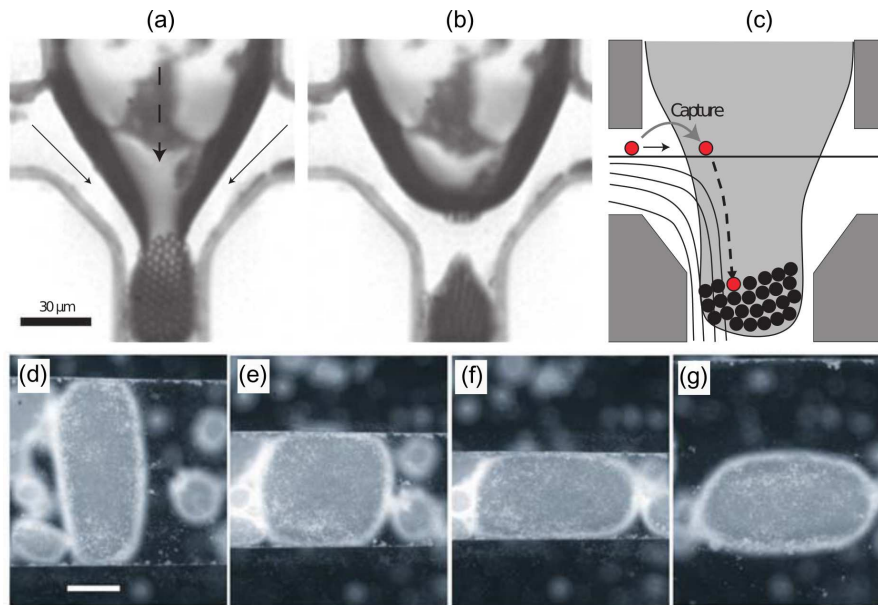


Figure 1.3: **(a)** Armored bubble in formation at the flow focusing junction. An air thread is pushed in the middle (dashed arrow) and is pinched by a flow of colloidal dispersion in the lateral channels (solid arrows). **(b)** When the tip of the thread is sufficiently loaded with particles, it detaches and form an armored bubble. **(c)** Skeetch of the trajectories of the particles from the bulk liquid to the interface. **(d-g)** Armored bubble being squeezed between to glass slides. It deforms from a prolate ellipsoid shape to an oblate shape through a plastic rearrangement of the beads. Scale bars are $200 \mu m$. Adapted from [18].

These studies demonstrated that the aeration of dispersions of suitable particles lead to the formation of foams, with a shelf life of several weeks or even months. As shown above, the depth of the energy well in which an interfacially adsorbed particle is trapped, depends on the contact angle of the liquid on the solid particle, and is maximum at 90° . Therefore, the particles must be wisely chosen, with a contact angle not too far from 90° , to ensure a sufficiently strong adsorbtion.

Figure 1.5 shows a picture of such a foam, stabilized solely with hydrophobised silica nanoparticles. Indeed, native silica is too hydrophilic to adsorb on an air-water interface. It is necessary to chemically graft hydrophobic groups on its surface, to enhance adsorbtion. The sample exhibits the visual characteristics of a foam: the bubbles diffuse the incoming light, giving it its white color, and the sample can hold its pyramidal shape under gravity, a signature of the existence of a yield-stress, characteristic of liquid foams [1].

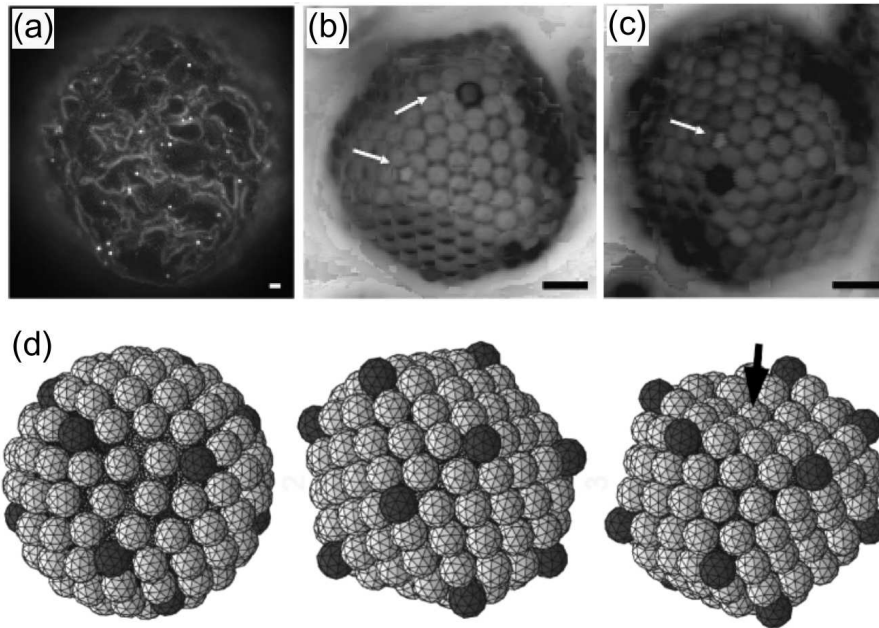


Figure 1.4: (a) Wrinkled shell blocking the dissolution of the gas. (b-c) Faceted armored bubbles. Scale bars are $8 \mu m$. (d) Results of Surface Evolver simulations of armored bubbles. As its internal volume is deflated, it takes a faceted shape. Adapted from [21].



Figure 1.5: An aqueous foam stabilized by silica nanoparticles. Scale bar is 1 cm

1.5 Open questions and contribution of this thesis

Systems involving interfacially adsorbed particles have been studied for a long time, at a variety of scales, from a single particle to the complete architecture of a foam. While the mechanics of adsorption and stabilisation has been investigated [8], there is still a lack of understanding in the origin of the stability of armored bubbles.

In particular, all of the above studies on armored bubbles only lead to qualitative description of their behavior, and lack quantitative measurements of their mechanical properties. For instance, the concentration of dissolved gas in the degassed water in [21] is not controlled, so that it is impossible to know to what extent the armor is able to block the dissolution. More quantitative measurements have been done on droplets, but they might not be relevant for the case of gas bubbles and foams, since a gas is much more soluble in water than another liquid immiscible phase, such as oil. Furthermore, the description as a planar elastic sheet might not be sufficient to account for the behavior of spherical armored bubbles, due to the predominant role of gravity forces in the elastic behavior of the granular layer in the planar case. Finally, there is no obvious link between the ability of a given colloidal shell to stabilize a bubble, and the stability of this same bubble within a real foam.

I will present in this manuscript experiments giving access to precise quantitative measurements on individual armored bubbles, and I will build a more adapted model to account for their behavior.

1.6 Outline of Part I

In the next chapter, we investigate the fate of a colloid-armored bubble as its environmental conditions are varied. Thanks to recently developed microfluidic tools [32, 33], that rely on channels with non-parallel floor and ceiling, a single bubble is produced into a quiescent fluid, and held stationary for observation. We first show an efficient way of adsorbing colloidal beads at the air-water interface of the bubble to produce the armor. Then we describe a method to precisely control the dissolution of the bubble and the resulting compressive stress applied on the armor. This enables us to quantitatively measure the maximum dissolution stress that an armor can withstand, while observing its behavior. A theoretical model of the shell mechanics is then developed to account for the experimental observations. Finally, we show the implications of the mechanical stability of a single armored bubble for a large population of such objects, that is to say a particle-stabilized foam.

2

Materials and Methods

2.1 Fabrication of the microfluidic chip

2.1.1 Conventional soft lithography

Conventional microfabrication techniques commonly used in microfluidics rely on the fabrication of a master mold, of which a replica is made, using a suitable material. The most widely used material for this purpose is a silicone elastomer, the polydimethylsiloxane (PDMS). The one we use is manufactured by Dow Corning under the trade name Sylgard 184 and consists in two parts: a base of PDMS linear chains terminated by reactive groups, and a heat-activated curing agent that binds the chains together to form a 3D reticulated network. It has excellent replication capabilities, and its use is as simple as pouring it over the master mold, and baking it between 70°C and 150°C, for 15 min to 2h. The negative replica of the mold constitutes the first half of the microchip, in which entry holes are punched, and which is then bonded to a glass slide after a 35 s air-plasma treatment. This process has been known for a long time and is extremely convenient for fast prototyping design at the laboratory scale [34].

This is the replication method that we use here, but the fabrication of the master mold differs from what is commonly done. The simplest method to obtain a micron-sized imprint of a microchannel (ie: a mold) is to use optical lithography. In this method, a

layer of photosensitive material is deposited on a flat substrat, and is illuminated with UV light through a mask, whose transparent areas have the geometry of the desired channel. The process can be repeated through a second mask after deposition of a new layer of photosensitive material to obtain 3D shapes. The unexposed material is then dissolved using the appropriate chemical, which directly yields the mold. The main drawback of this technique is that the layer by layer deposition of resin leads more to a stack of 2D designs, rather than to a true 3D shape. For example, it is impossible using this method to obtain a smooth slope of continuously increasing thickness, which is what is needed in the design of our micro channels.

2.1.2 Micromachining of a mold

We circumvent this issue by taking advantage of micromachining methods that allow the fabrication of molds with more complex geometries. A block of metal is micromilled using a CNC machine (Minitech) with high precision in its three translationnal degrees of freedom ($1\ \mu m$). The geometry of the mold is drawn using a 3D software (Rhinceros) and the tool path used by the micromilling machine is computed by a computer assisted machining plugin (RhinoCAM).

A few rules must essentially be followed to obtain a mold with a geometry as close to the initial design as possible.

Feeding speed and spindle rotation The principle of milling is to feed the part to machine against a rotating tool. The sharp teeth of the tool cut the metal and remove small bits of material called chips. The geometry of the tool defines the geometry of the cut part. We use end mill tools, that cut grooves of rectangular sections with sharp right angles, as shown in figure 2.1(a).

The advance per tooth f_z is the distance covered by the tool during $1/z$ rotation of the tool, z being the number of teeth on the tool. As depicted in figure 2.1(b), this distance defines the thickness of the chip of metal that is cut by one tooth. Thus, f_z must be set to the nominal values required by the tool manufacturer. Indeed, if the chip is thicker than the nominal value, the stress on the material and on the tool becomes too large, which might either break the tool, or reduce the precision of the cut. On the other hand, if the chip is thinner, the tooth will rather scratch than cut the metal, which leads to a poor surface state.

The advance per tooth is set by a combination of two machining parameters, tunable by the user. The first parameter is n , the rotation speed of the spindle holding the tool, in rotations per minute (rpm). The setup we use has a maximum rotation speed of 60'000 rpm. The second parameter is the feeding speed V_f , which is the speed at which

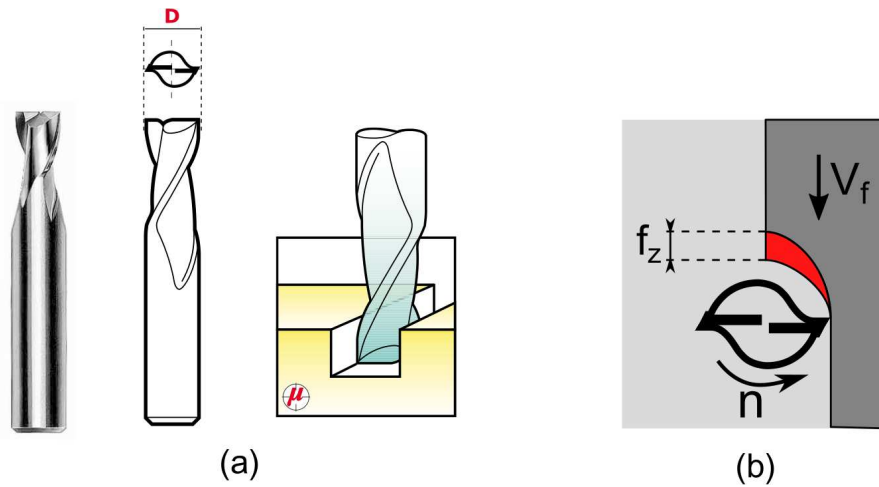


Figure 2.1: **(a)** Picture and drawing of a 3 mm end mill tool with 2 teeth. The drawing on the right shows the operation of the tool and the section of the groove created. Adapted from Magafor documentation. **(b)** Sketch showing the chip in red. It is defined by the area cut by the incoming tooth as the part is fed against the tool, from top to bottom (V_f). The light gray area is the region already machined, while the darker gray represents the region to be machined, thicker.

the table on which the part is fixed moves. Its maximum value is 1800 m/min. The relationship from the definition of f_z is

$$f_z = \frac{V_f}{zn} \text{ (in mm)} \quad (2.1)$$

For each tool diameter, a value of f_z is prescribed by the tool's manufacturer. Thus, for the largest tool, the limiting parameter is the maximum feeding speed, and for the smallest tools, the limiting factor is the maximum rotation speed. The following table sums up the optimal parameters for commonly used tools, which all have $z = 2$ teeth.

Tool \varnothing (mm)	f_z (mm)	V_f (m/min)	n (rpm)
3	0.05	1800	18'000
1	0.02	1800	45'000
0.15	0.003	360	60'000
0.05	0.001	120	60'000

It appears that small tools work much slower than larger ones, that is why it is optimal to reduce their use as much as possible to avoid excessive machining times.

Materials The easiest metals to machine are aluminium, and brass, which is an alloy of copper and zinc. We chose brass because of its ease of machining and because it

is harder than aluminium, which allows for thinner mold structure without risk of deformation. During the machining process, cutting oil is sprayed on the part to ensure a good lubrication and avoid tool overheating.

Machining strategy The typical machining process is sketched in figure 2.2. Metal must be removed from the stock part (ie: the raw metal piece) to expose the desired part geometry. The first step consists in successive passes of large depth (10% of the tool diameter) to quickly remove a thick layer of metal. This leaves a rough shape of the desired part with an excess of metal of $\approx 10 \mu m$. The sloped areas are roughed by step machining, with tool path parallel to the slope, which leaves a stair shape just above the desired slope line. The roughing step enables the quick removal of a thick layer of metal but it leads to a flawed part. Firstly, the surface state is rather bad, and the roughness is not acceptable for use as a microfluidic mold. Indeed, deeper passes cut thicker metal chips, which is the source of higher cutting stresses in the material, and explains the rough surface state obtained. Secondly, at the edges of the machined patterns, residual metal can build up and form burrs (see figure 2.2(b)). The part is cleaned by a finishing step with low depth passes (1% of the tool diameter) that removes very thin layers of material at once. This kind of machining yields a smoother surface, with a root mean square roughness $< 100 nm$. The profile of the slope area is refined by cutting lines parallel to the slope and typically $3 \mu m$ apart. The result is a succession of very thin steps, extremely close to a continuous slope.

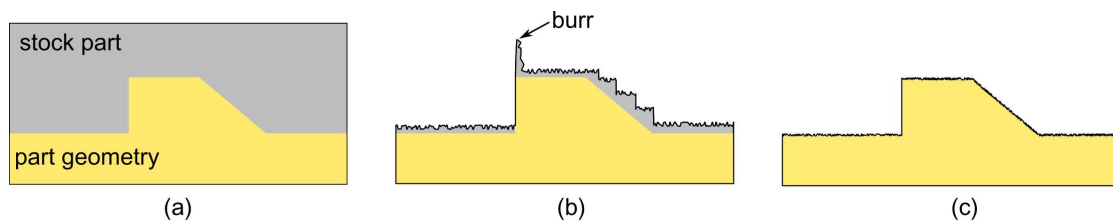


Figure 2.2: Micromilling steps. **(a)** Initial stock part with the desired geometry highlighted in yellow. **(b)** Roughed part. **(c)** Finished part.

This last finishing step can be repeated with multiple tools of different diameters, depending on the size of the patterns on the mold. Indeed, the minimum radius of curvature reachable for an internal angle is equal to the radius of the tool used. Smaller feature such as narrow channels and injectors require the use of a smaller tool diameter. Typically in our case, the roughing step and large areas machining is done using a 3 mm end mill (see figure 2.1(a)), then a 1 mm tool is used for a first refinement, and finally a 0.15 mm or 0.25 mm tool for the smallest features. Smaller tools enable a

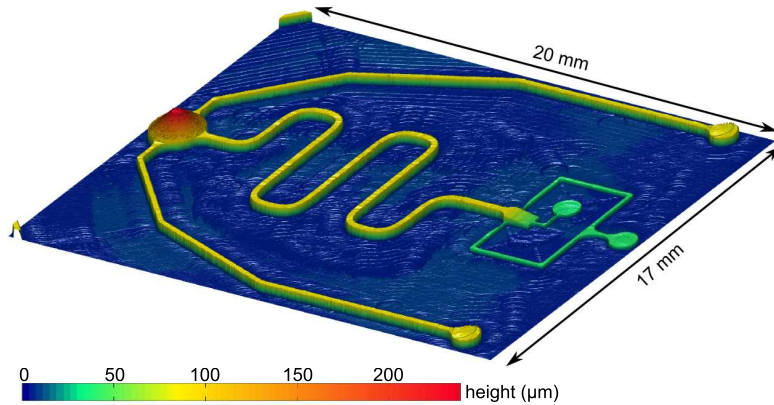


Figure 2.3: 3D profile of the mold. The height of the central channel is $80\mu\text{m}$ and its width is $300\mu\text{m}$. The slope of the bubble injector is 4%.

higher precision for the replication of small features, but it is at the expense of longer machining time as explained above. Furthermore, smaller tools are more likely to break and are more expensive than larger ones.

Final geometry

The part is analyzed using an optical profilometer (Zygo), as shown on figure 2.3. Multiple acquisitions are stitched together to obtain a complete 3D profile of the brass mold.

2.1.3 Surface state of the channel

The working principle of the wedged injector relies on the hypothesis of total wetting of the outer phase on the channel's wall (see section 2.2). This is particularly difficult to achieve in our case, since the experiments must be performed without any trace of surfactant in solution, which would hinder the adsorption of particles on the interface (as shown in section 3.4). The most commonly used method to render the glass and PDMS inside the channel hydrophilic is to use plasma treatment, which is already a part of the fabrication process. After curing the PDMS, the channel is closed with a flat glass slide, which is covalently bonded to the PDMS after a 35 s air-plasma treatment. The contact with plasma strongly oxidizes the glass and PDMS, which creates hydroxyl surface groups (-OH), whose presence renders the surface very hydrophilic. This hydrophilicity is preserved if the channel is filled with distilled water just after the plasma treatment.

However, the PDMS has a tendency to recover its native hydrophobicity over time, which is characterized by a contact angle value of $\approx 110^\circ$. This is due to the mobility

of the low molecular weight (LMW) unreacted polymer chains that remain in the bulk material after curing [35]. These chains slowly migrate from the bulk to the surface of the PDMS, where they react with the hydrophilic (-OH) groups, canceling the hydrophilicity. A method to limit this phenomenon is to thermally age the PDMS after curing, to react the LMW chains and immobilize them into the bulk [36]. Therefore, the PDMS chips are cured at least 24h before being bonded to glass and stored under water to prevent drying, which preserve the hydrophilicity. This treatment is necessary since the deep vacuum inside the plasma chamber removes the dissolved gas from the PDMS. It is then necessary to let the channel reequilibrate with air atmospheric pressure for 6-12h before any bubble dissolution experiment can be performed.

2.2 Production of a single air bubble by gradient of confinement

To produce an armored bubble, a single air in water bubble needs first to be generated. The conventional microfluidic methods usually deployed to produce bubbles or droplet are T-junction or flow-focusing [37, 38] channel geometries. These methods have proved efficient when a high throughput production of droplets or bubbles is needed. However, the performances are poor at low flowrate, and it is difficult to use them to produce single objects. This is especially true with air, whose flowrate is difficult to control because of its large compressibility. Indeed, a plug of air inside a microfluidic chip considerably increases the hydraulic capacitance of the system [39]. In consequence, the time to establish a steady flow considerably increases, rendering the fine control of the flowrate very difficult. We circumvent this problem by taking advantage of a tool developed in the lab, that enables the production of bubbles or droplets in a quiescent fluid at very low flowrate [33]. This bubble production device is based on the curvature imbalance that arises when a thread of non-wetting liquid flows into a Hele-Shaw cell with non parallel floor and ceiling. As shown in figure 2.4, a tongue of non wetting fluid (in our case, air) first expands in a reservoir initially filled with a wetting liquid (in our case, de-ionized (DI) water). The tongue then destabilizes and detaches from the injector, forming the bubble.

Breakage mechanism Dangla *et al.* [33] observed that with this geometry, droplets or bubbles of definite size are produced, even at very low injection flowrate, which led them to assume a quasistatic regime, in which the fluid is at mechanical equilibrium at all times. In this situation, the Laplace's law imposes that the mean curvature of the air-water interface should remain constant, except in the region where it is pressed

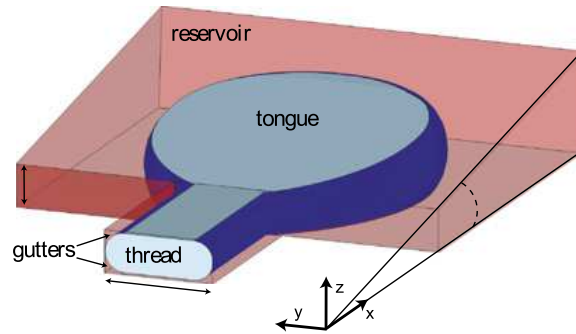


Figure 2.4: Geometry of the bubble production unit. An air thread (in blue) is pushed into a wedged chamber initially filled with water (in pink). As it is pushed, the thread of air expands into a circular flat tongue. From Dangla et al. [33]

against a wall of the channel. Yet, the geometry imposed by the channel differ in the inlet and reservoir region. The mean curvature of the surface can be decomposed into two contributions, κ_{\perp} and κ_{\parallel} , respectively the curvature in the directions perpendicular and parallel to the plane of the wedged Hele-Shaw cell.

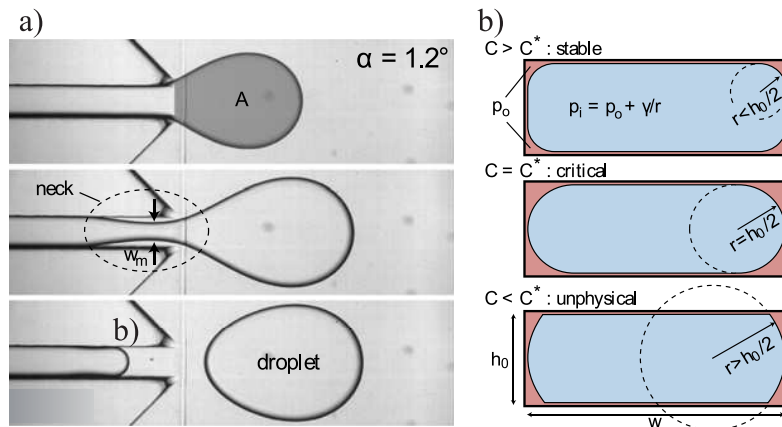


Figure 2.5: **(a)** Destabilization of the tongue. At a critical value of injected volume, the thread pinches and the droplet/bubble detaches. **(b)** Cross section of the thread as the tongue curvature decreases (from top to bottom). From Dangla et al. [33]

As fluid is progressively injected, the curvature in the tongue decreases in two ways. First, the volume increase leads the forming droplet to increase its radius R , so that $\kappa_{\parallel} \propto 1/R$ decreases. Second, the wedged geometry of the reservoir leads to an increase of its thickness h , and $\kappa_{\perp} \propto 1/h$ decreases as well. To satisfy Laplace's law, the curvature in the thread must decrease in the same way. At first, there is no parallel curvature component in this region, so the only curvature is given by the corners of the interface, near the gutter of the injection channel (see figure 2.5(b,top)). As the curvature in

the tongue decreases, this curvature must also decrease up to a critical value where it equals the inverse of the half-channel thickness (figure 2.5(b,middle)). Past this point, it cannot decrease furthermore without falling into the unphysical situation described in figure 2.5(b,bottom). In order to cope with the curvature of the tongue, the threads bends inwards, adding a negative κ_{\parallel} to the thread's mean curvature. This correspond to the necking event showed in figure 2.5(a,middle). Eventually, the neck size will be reduced until it destabilizes via Rayleigh-Plateau instability, thus forming the drop.

It is worth noting that the case depicted in (figure 2.5(b,bottom)) is unphysical given the assumption of a perfect wetting of the external phase on the walls of the channel. If this condition is relaxed, this situation corresponds to a dewetting of the external phase, or equivalently a wetting of the internal phase. If this occurs, the thread possesses a very large reservoir of curvature, the formation of the neck is greatly retarded and the droplet may never detach from the inlet. This explains why, in the present case of bubble production, a proper wetting of the external water phase on the surfaces of the microfluidic channel is crucial.

2.3 Particles

2.3.1 Colloidal beads used

The particles used for the experiments were yellow-green fluorescent polystyrene (PS) microbeads, charge-stabilized by covalently bonded carboxylate groups . They were washed 3 times with distilled water by centrifugation-sonication cycles and finally redispersed in DI-water with 0.5 M sodium chloride (pH=7) to a final solid concentration of 0.5% w/w. Salty water was used in order to screen the electrostatic repulsion between the particles and the interface [8], to facilitate adsorption. In our experiments, we used three different particles diameters, 0.5, 1.1 (Fluospheres, Life Technologies) and 4.5 μm (Fluoresbrite, Polysciences).

2.3.2 Fabrication of ellipsoidal particles

In order to evaluate the effect of the particle shape on armor properties, ellipsoidal colloids are fabricated. We choose to use the particles described above and to deform them to reach the desired shape. This has the benefit of ensuring that the particles retain the same chemical properties, in particular the water contact angle θ . We apply a protocol described previously to stretch our polystyrene microbeads [40]. This protocol is schemed in figure 2.6.

First, the PS particles are dispersed in an aqueous solution of polyvinyl alcohol (PVA), a water soluble polymer. Then the solution is cast on a flat substrate and let

air-dried at room temperature overnight. The resulting film is then mounted on an extensible frame, and the assembly is immersed in a silicon oil bath heated at 170°C . This temperature is above the glass transition temperature both of PS and PVA, so that the film can be stretched to the desired elongation thanks to the mobile frame. The elongated film is then cooled down and residual silicon oil is rinsed with isopropyl alcohol. The PVA film is redissolved in a DI water/isopropyl alcohol (IPA) mixture to redisperse the elongated particles, which are washed by multiple centrifugation/redispersion cycles in DI water. This process yields prolate PS ellipsoids, whose aspect ratio is proportionnal to the elongation applied on the PVA film. We perform scanning electron microscopy on dried samples of dispersion, as shown in figure 2.7. The dimensions (major and minor axis) of the colloidal ellipsoids were directly measured on these images. The maximum aspect ratio reached is 3.5, and is limited by the size of the extensible frame.

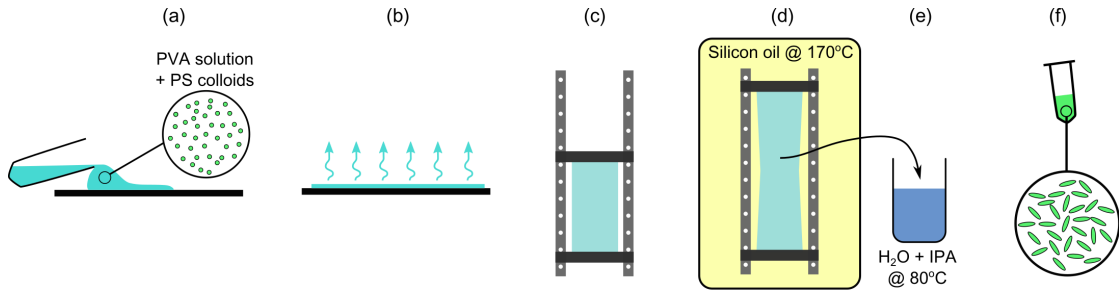


Figure 2.6: **(a)** The PVA solution containing the dispersed PS spheres is cast on a plate. **(b)** It is air-dried, which yields a PVA film with embedded PS colloids. **(c)** The dried film is cut and mounted on an extensible frame. **(d)** The frame is immersed in hot silicon oil, extended, and removed from the oil bath while maintaining the extension. **(e)** The film is washed in IPA and redissolved in a 50/50 v/v mixture of DI water and IPA at 80°C . **(f)** After several centrifugation/redispersion cycles, a dispersion of ellipsoidal colloids in water is obtained.

The quality of the cleaning protocol is tested by submitting $1\mu\text{m}$ particles to the thermal treatment in the PVA film but without elongation. The resulting particles are spherical, and their behavior is the same as the initial untreated particles when used in armor bubble experiments..

2.4 Imaging and control

The experiments in the microfluidic chip are monitored using an inverted Nikon microscope. Multiple types of illuminations are used, including brightfield, phase contrast, and epifluorescence. The images are acquired with an Insight Spot camera or a Photron

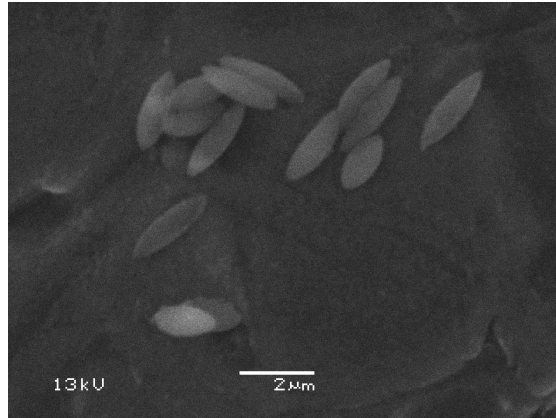


Figure 2.7: SEM micrograph of ellipsoids deposited by air-drying the dispersion obtained at the end of the protocol.

SA3 fast camera. Thresholding image analysis and the subsequent data extraction is performed under Matlab software.

For certain images, focus stacks are acquired either manually or using the motorization of the z-axis of the microscope. These stacks are then reconstructed into images with an extended depth of field using Nikon Elements or Adobe Photoshop softwares. These highly detailed images enable a qualitative description of the colloidal shells.

The flow in the microfluidic channels are driven by Cetoni Nemesys syringe pumps and Scientific Glass Engineering Analytical Science glass syringes, connected to the PDMS chip *via* polytetrafluoroethylene (PTFE) tubing. The internal pressure of the chip is controlled using an external Fluigent MFCS pressure controller.

Finally, the temperature is an important parameter and must be regulated to ensure the accuracy of the measurements. The microfluidic chip is therefore placed on a heated microscope stage (Warner Instrument), maintained at 50.0° throughout the experiment. An aluminium foil wrapped around the setup minimize the thermal perturbations due to the convection in the ambient air.

3

Experiments with armored bubbles

3.1 Producing and monitoring an armored bubble in microfluidics

In this section, we present the operation of the microfluidic device used in our experiment. A bright-field top view of the chip is shown in figure 3.1, where its three main parts are highlighted. First (I), a wedged injector produces a single bubble on demand, according to the principles described earlier. Then (II), the bubble is pushed through a long coating channel, where its interface is coated with adsorbed colloidal particles. The coating mechanisms are explained in the next paragraph. Finally (III), we show how the armored bubble is trapped in a controlled environment observation chamber, to monitor its behavior under various conditions.

The progression of the bubble in the chip is shown in figure 3.2, which corresponds to the movie 1. The bubble is produced at the wedged inlet, and then journeys through the coating channel, before being released in the conical chamber.

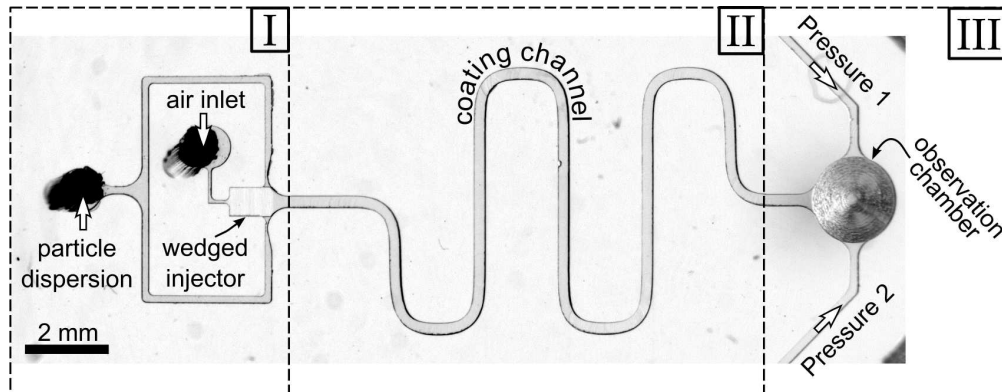


Figure 3.1: Bird's eye view of the microfluidic chip used in the experiments. **(I)** Area of bubble production, with air and particle dispersion injectors. **(II)** Coating channel, to force the adsorption of particles at the air water interface and build the armor. **(III)** Conical observation chamber, connected to two independent outlets of a pressure controller.

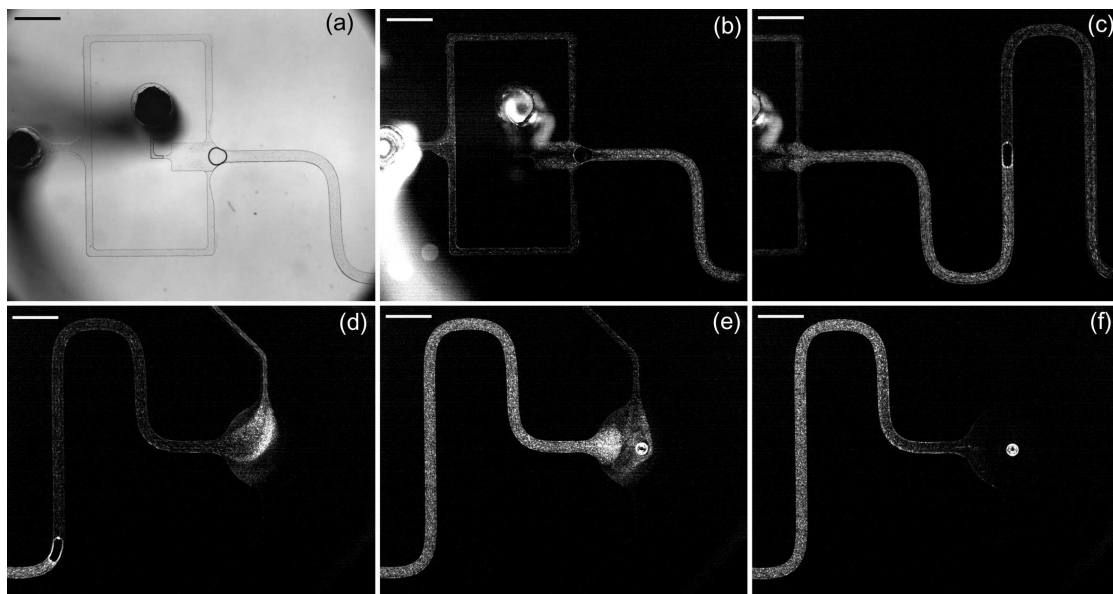


Figure 3.2: **(a)** $t=0$ s. Bubble in the wedged injection chamber, in brightfield illumination. **(b)** Same as **(a)**, in epifluorescence. The particles appear in white. **(c-d)** $t=4-12$ s. The bubble is pushed through the coating channel. **(e)** $t=21$ s. The partially armored bubble is released in the conical chamber. **(f)** $t=24$ s. The particles still in suspension, not adsorbed on the interface are washed away by flow from the side channels. Scale bars are 1 mm.

3.1.1 Covering the air bubble

After its formation, the bubble moves along the gradient of confinement and reaches the rightmost extremity of the wedged injector, at the entrance of the coating channel. The bubble is then pushed by a flow of colloidal dispersion injected via two side injectors. The channel has been initially filled with particle dispersion, so that the bubble is surrounded by suspended particles. The flow of colloidal dispersion forces the bubble to travel inside the coating channel, where the armoring by colloidal beads takes place. Figure 3.3 shows the evolution of the bubble as it travels along the coating channel. The images are composites of bright-field and epifluorescence micrographs, where particles appear in green. The bubble has very few particles adsorbed on its surface at the entrance of the channel (figure 3.3(a)). As it progresses in the coating channel, particles gather at the rear of the bubble, gradually building the armor (figure 3.3(b,c)).

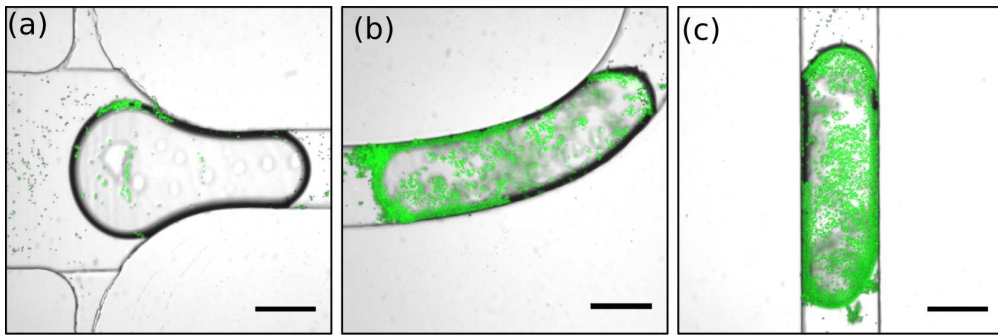


Figure 3.3: Composite micrographs of the bubble being covered with particles as it travels through the coating channel. The fluorescent particles appear in green. ((a)) Bubble in the injector, at the entrance of the channel. (b) Bubble in the first curve of the coating channel. (c) Bubble in the last straight line of the channel. Scale bars are $200 \mu m$.

Figure 3.4 gives a more quantitative view of the covering process. The geometry of this covering channel is different. It is straight, and its height slowly increases with a slope of 0.5%, which explains the apparent size reduction of the bubble as it progresses through the channel. However, the coating mechanism stays the same and this very slight slope has no effect. In these bright field images, the bubble is initially transparent and becomes progressively darker, as the particle coverage increases. We did not carry out systematic measurements but this type of setup would allow a precise monitoring of the coating rate of the bubble.

We now present a mechanism for the adsorption of particles at the air-water interface. This mechanism has been recently extensively described by Zoueshtiagh *et al.* [41] in various wetting conditions at the scale of a millimetric glass capillary tube, but is slightly

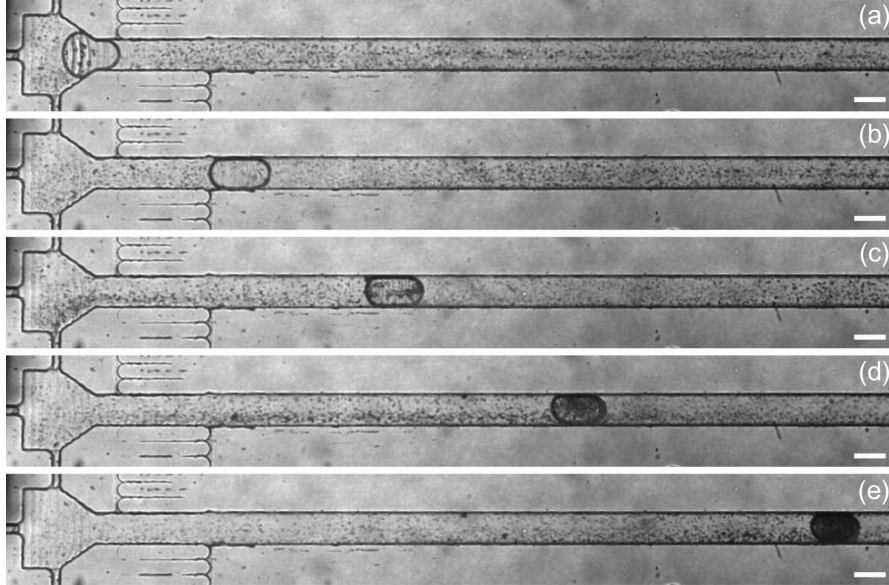


Figure 3.4: Coating of a bubble in a straight channel. The scale bars are 1 mm and the images are 2 s apart.

different in our case. Similar bubbles behaviors have also been observed at smaller scales in microfluidic channel, using nanoparticles [42]. Therefore, we assume that a similar mechanism takes place in our coating channel. Zoueshtiagh *et al.* have shown that the mechanism at play when an air-in-colloidal-dispersion bubble travels through a capillary depends strongly on two contact angles: (i) the contact angle of the liquid phase (here water) on the wall of the capillary, (ii) the contact angle of the liquid dispersing phase on the solid particles.

In our case, the outer phase (water) partially wets the walls of the channel made of glass on one side, and PDMS on the other. As stated earlier, we ensured that these walls stay hydrophilic on the time scale on the experiment. However, the exact contact angle is unknown, but it can reasonably be assumed to lie in between 40° and 70° [36].

Regarding the contact angle on the particles, we were able to image a single particle adsorbed on the interface of a bubble with very low particle coverage. Using both bright-field illumination and epifluorescence, it is possible to image a side view of the adsorbed particle and its specular reflexion in the air-water interface (see figure 3.5). This way, we directly measure on the image an estimate of the contact angle of the water on the particle, $\theta_P \approx 35^\circ - 45^\circ$.

Using the phase diagram established by Zoueshtiagh *et al.* (see figure 3.6), we find that our experimental parameters correspond to the regime of particle being captured by the rear meniscus of the bubble, as is observed in our device.

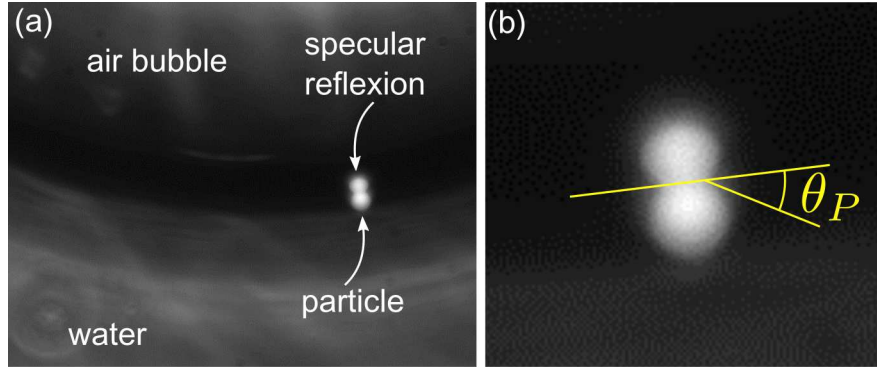


Figure 3.5: (a) Image of a single $4.5 \mu\text{m}$ particle adsorbed on an air-water interface. The particle emits fluorescent light, and its specular reflexion in the interface can be seen. (b) Close-up showing the geometrical construction used to estimate the wetting contact angle of water on the particle.

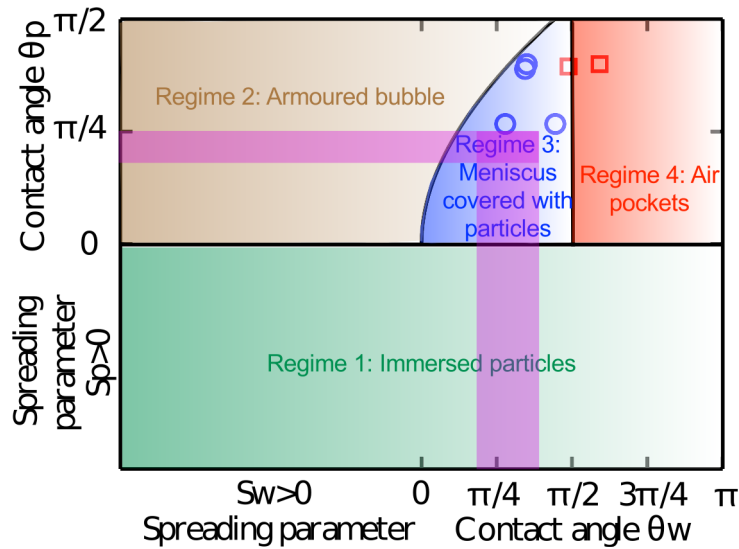


Figure 3.6: Phase diagram adapted from Zoueshtiagh *et al.* [41], showing the behavior of an air bubble pushed through a capillary filled with colloidal dispersion. The contact angle of the liquid on the particles is reported on the vertical axis, and the contact angle on the wall on the horizontal axis. The case of the present experiment is highlighted in pink, and falls in regime 3.

More precisely, as the bubble advances, particles near the floor and ceiling of the channel may be trapped in the lubrication films when they come close to the nose (ie. the front meniscus) of the bubble [43]. Since the bubble has an elongated pancake geometry, the trapped particles are squeezed between the interface and the wall (see figure 3.7). The thin film separating them from the bubble quickly drains, the particles pierce the interface, and becomes irreversibly adsorbed. Dewetting can occur on the wall,

creating some 'dewetted patches', ie. droplets of water with adsorbed particles, pinned on the wall (see figure 3.7(d)). This is not an issue because they are 'swept' by the rear meniscus that integrate the newly adsorbed particles into its interface, according to the mechanism described in [41].

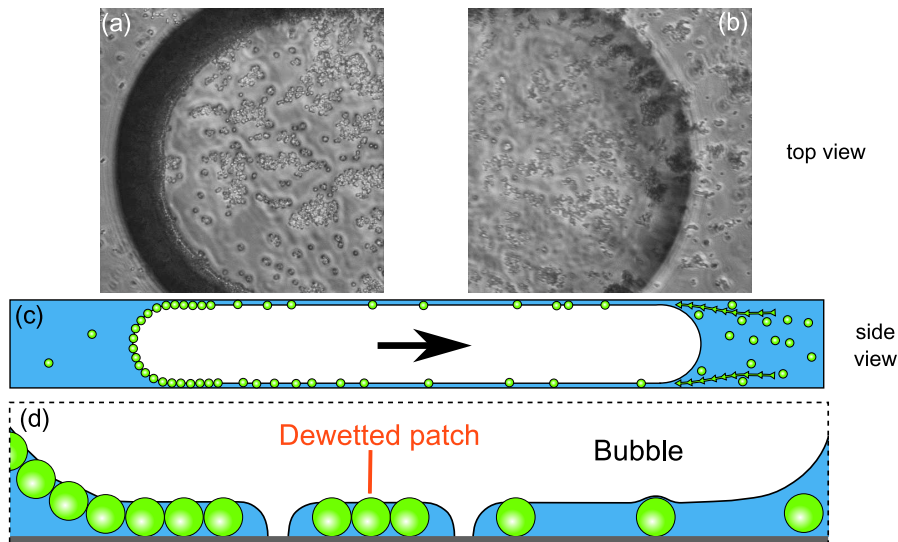


Figure 3.7: **(a-b)**Phase contrast micrographs of the front meniscus (b) and rear meniscus (a) of a bubble advancing in the coating channel. **(c)** Side view of the bubble squeezed in the coating channel, moving from left to right. The green arrowed lines at the front of the bubble indicate the trajectories of the beads trapped in the lubrication films. **(d)** Close-up (not to scale) of the bottom face of the bubble, pressed against the glass slide, represented by the thick gray line.

However, in Zoueshtiagh's experiment, the capillary has a circular section. In that case, the regime of covered meniscus can not give birth to an armored bubble because when it becomes fully covered, it reaches a limit contact angle at the wall and cannot integrate new particles. Once enough particles have covered the meniscus, it is not energetically favorable anymore to integrate new particles. But in our case, the channel has a rectangular cross section, which leaves gutters in the corners of the bubble where the adsorbed particles can freely recirculate, as depicted in figure 3.8 (see also movie 2). The particles are first trapped at the nose of the bubbles, then packed into the rear meniscus, and when the later is sufficiently covered, particles start to flow back toward the nose of the bubble. This recirculation enables a nearly complete coverage of the bubble.

However, the rate at which the particles adsorb on the interface must be carefully tuned. Indeed, if the bubble reaches full coverage before the end of the channel, the adsorbed particles suddenly jam and the recirculation stops. The incoming flow of dis-

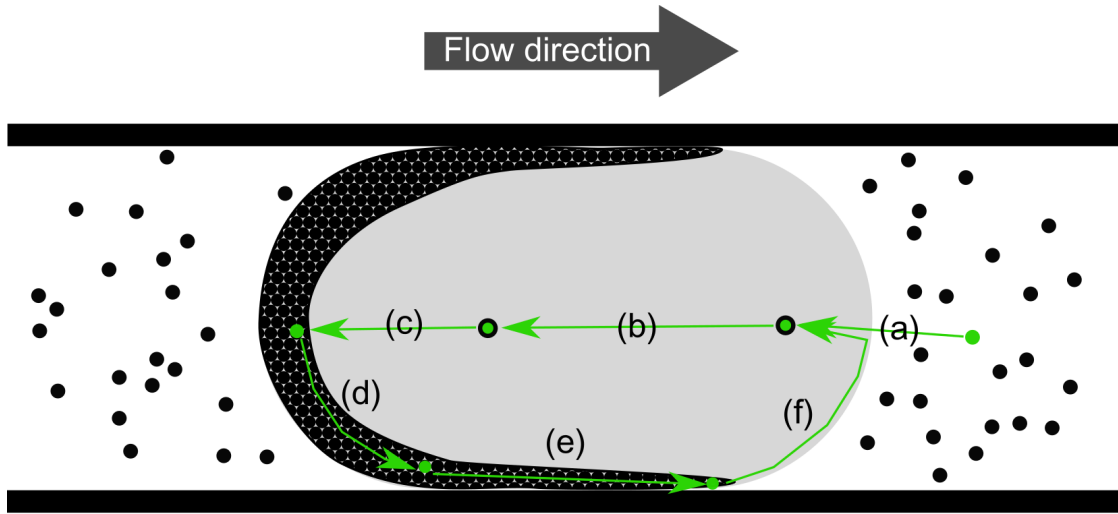


Figure 3.8: Sketch of a top view of a bubble being pushed from left to right in the coating channel (same point of view as in figure 3.7(a-b)). **(a)** The green bead is first captured from the bulk dispersion to the lubrication film. **(b)** It then is trapped and squeezed against the wall of the channel. **(c)** The particle is then absorbed in the forming armor at the rear of the bubble. **(d)** As the armor gets more and more packed, it is pushed back toward the nose by other incoming particles. **(e)** It is then pushed further in the gutters of the channel. **(f)** Finally, it comes back to the nose of the bubbles, and flows back into the lubrication film.

persion may then fragment the armored bubble, similarly to what is observed by Kotula *et al.* [42]. To avoid that, we dilute the initial particle dispersion to a concentration of 0.5% w/w so that the coverage of the bubble to not increase too quickly in the covering channel. The objective is that at the end of its travel through the coating channel, the bubble is almost fully coated with a monolayer of adsorbed particles.

3.1.2 Trapping and monitoring the bubble

After the bubble has been coated with particles in the coating channel, it is released in a conical observation chamber. The geometry of this chamber is depicted in figure 3.9(a). It consists of a wide cavity of radius 1 mm with a conical ceiling of maximum height $250 \mu\text{m}$. The slope of the top wall ensures that the bubble rises by buoyancy and stays trapped at the center of the chamber. When the partially armored bubble leaves the coating channel, it is quickly attracted toward the center of the chamber. Afterward, a flow of clean water without particles is applied through the side channels labeled *Pressure 1* and *Pressure 2* on figure 3.1. This removes the unattached particles floating around the armored bubble. As seen on the video, these particles are advected by the flow, while

the adsorbed particles circulate at the surface of the bubble. At the end of this process, a partially armored bubble is left trapped at the center of the observation chamber, as showed in figure 3.9.

One can show that the bubble remains essentially spherical by calculating the Bond number of the system:

$$Bo = \frac{\Delta\rho g R^2}{\gamma} \approx \frac{10^3 \cdot 10 \cdot 10^{-8}}{10^{-1}} = 10^{-3}, \quad (3.1)$$

where $\Delta\rho$ is the mass volume difference between air and water, g is the acceleration of gravity, R the typical radius of a bubble in the chamber, and γ the air-water surface tension. Since $Bo \ll 1$, it is reasonable to consider that the trapped bubble is spherical.

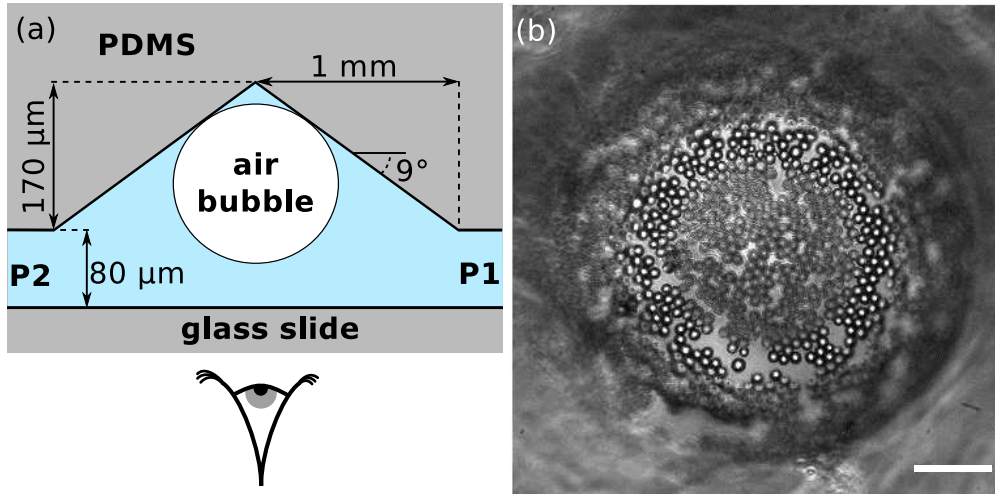


Figure 3.9: (a) Cross section schematic of the conical observation chamber (not to scale). The trapped bubble is observed from below through the glass slide closing the microfluidic system. (b) Phase contrast micrograph of the bubble partially covered with $4.5 \mu m$ diameter particles. Scale bar is $30 \mu m$.

The pressures in the two side branches P1 and P2 ('Pressure 1' and 'Pressure 2') can be independently adjusted. By setting a slight pressure difference between the two, we create the gentle flow necessary to wash the bubble. It is also possible to set the same pressure in both branches, but at a value higher than the atmospheric pressure. No flow is established because the channel is sealed, and its volume is fixed. We use this ability to fine tune the internal ambient pressure around the bubble to control its behavior. Indeed, an air-in-water bubble will swell if the pressure P is below a certain equilibrium value P_{eq} , and will dissolve and shrink if it is above. For $P = P_{eq}$, the bubble will stay stationary. The reason for this behavior is explained in details in section 4.1.1,

but we can already define a control parameter, $\Delta P = P - P_{eq}$, that sets the behavior of the armored bubbles in the observation chamber. We experimentally demonstrate this control by varying the pressure around an unarmored bubble. Figure 3.10 shows the time evolution of the relative radius of the bubble for different values of ΔP , for a typical experimental temperature of $50,0^\circ\text{C}$ and an initial bubble radius of $R = 120 \mu\text{m}$. In these conditions, the equilibrium pressure is $P_{eq} = 80 \text{ mbar}$. At that pressure value, corresponding to $\Delta P = 0$, the radius of the bubble changes by less than 1% over 20 minutes, which indicates that the unstable state of equilibrium has been reached. As soon as the value of ΔP is increased (resp. decreased), the radius of the bubble decreases (resp. increases). It can also be noticed that the rate of variation of the bubble radius is related to the absolute value of ΔP . The further the system is driven out of equilibrium, the higher the rate of variation of r .

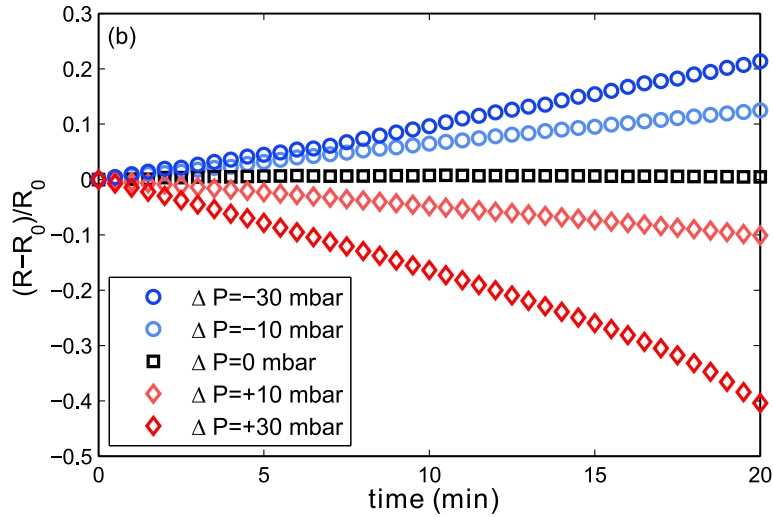


Figure 3.10: Measurement of the time evolution of the normalized radius of an air bubble in water, for different values of ΔP .

3.2 Measurement of armor resistance

In this section we use the microfluidic device and apply the pressure control over the bubble dissolution to probe the resistance of an armored bubble. First, the systematic experimental procedure is exposed, then the resulting behavior of the particle-coated bubble is described qualitatively and quantitatively.

3.2.1 Progression of a typical experiment

After a bubble has been produced, coated, and washed, it is armored with a monolayer of particles and trapped in the observation chamber. First, the system is calibrated: the pair (R, P_{eq}) must be tuned together before the armor strength can be determined. A typical experiment therefore begins by shrinking the bubble to a radius for which the particles at the interface are nearly jammed, since the bubble surface is initially only partially covered. This is done by increasing P well above a rough estimate of P_{eq} (typically up to 100 mbar). Once this radius R is reached, P is finely tuned until the bubble size remains stationary for several minutes, indicating that the equilibrium pressure P_{eq} has been found for the current bubble with a nearly jammed shell.

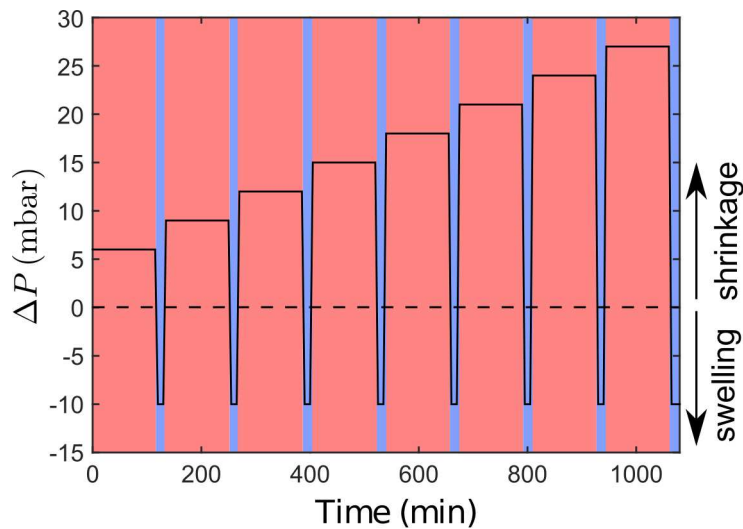


Figure 3.11: Pressure profile applied to the bubble. The dissolution pressure ΔP is progressively increased step by step. The red overlay represents the periods of dissolution and compression of the armor ($\Delta P > 0$), while the blue ones are for the swelling and stress release periods ($\Delta P < 0$).

We have seen that an air-in-water bubble will shrink if $\Delta P > 0$. Without armor, it will ultimately completely dissolve and disappear. However, when it is enclosed in a colloidal armor, the particles can resist the dissolution up to a limiting dissolution pressure ΔP^* that we wish to determine. For this, ΔP is increased stepwise, from a few millibars above P_{eq} until collapse is observed, following the profile plotted in figure 3.11. The steps of $\Delta P > 0$ corresponds to periods when the bubble shrinks and the armor is compressed isotropically (pink rectangles on the graph).

Their duration is 2 hours, to ensure that the armor truly stabilizes the bubble. Indeed, when the armor is shrinking, ie. losing gas, the flux of gas at its boundary imposes a concentration profile that relaxes to a certain value as the distance from the

bubble increases. When the bubble shrinking is blocked by the armor, the flux at the boundary vanishes, and the concentration profile must become flat, so that it is equal to the value far from the bubble everywhere. This flat state of the concentration must be realised to ensure that the steady state is reached, and that the armor would stabilize the bubble indefinitely. The time it takes for the concentration profile to relax can be estimated as $t_{relax} = D_c^2/D_{air/water} = (10^{-3})^2/2.3 \times 10^{-9} \approx 430s \ll 2h$, where D_c is the radius of the observation chamber, and $D_{air/water}$ is the coefficient of diffusion of air in water. The estimated relaxation time is thus much shorter than the 2h hour step maintained at each pressure. More over, a very weak flow of water ($<5\mu m/s$) is maintained around the bubble to accelerate the relaxation of the concentration profile by advection. This shows that the steps are long enough to reach stationary regime.

Between each of these compression steps a short period of negative ΔP (blue rectangles on the graph) allows the bubble to swell again before the next pressure increase, in order to release any stresses that build up during the dissolution step.

The evolution of the armored bubble is monitored over time and the projected area of the armor is extracted by image thresholding. The results are shown in Fig. 3.12(a). The plot shows a first range of pressures for which the area is stable over a period of two hours, indicating that the armor is capable of blocking the dissolution of the gas into the surrounding medium at these values ($\Delta P \in [6 - 18]$ mbar in this example). The peaks correspond to the $\Delta P < 0$ steps, the sudden area rise corresponding to the rapid swelling of the bubble. Figure 3.12(b) shows representative states of the bubble during the experiment (see also movie 3). It can be seen that the shell remains spherical and smooth in this regime, showing that the structure of the armor is stable and blocks the gas dissolution.

3.2.2 Buckling of the armor

The armor stabilizes the bubble only up to a certain point. At a particular value of ΔP (denoted $\Delta P_{collapse}$), the measured area sharply decreases with time, as can be seen at the sixth pressure step in figure 3.12. This indicates the sudden buckling of the colloidal shell. Above this value the armor is no longer stable and the bubble dissolves completely into the water, leaving the colloidal particles in suspension. The same behavior is observed for all of the particle sizes that we have tested. For smaller particles (500 nm), as shown in figure 3.12(b) and 3.13, the armor is at first smooth and spherical, but its symmetry is lost after buckling, as large region of the shell bend inward under the compressive dissolution stress. The magnified views (c) and (d) show that the particles form a monolayer before buckling, but this arrangement is retained after buckling. This also takes place for larger $4.5 \mu m$ particles (figure 3.14), the armor collapses like a continuous material, in spite of

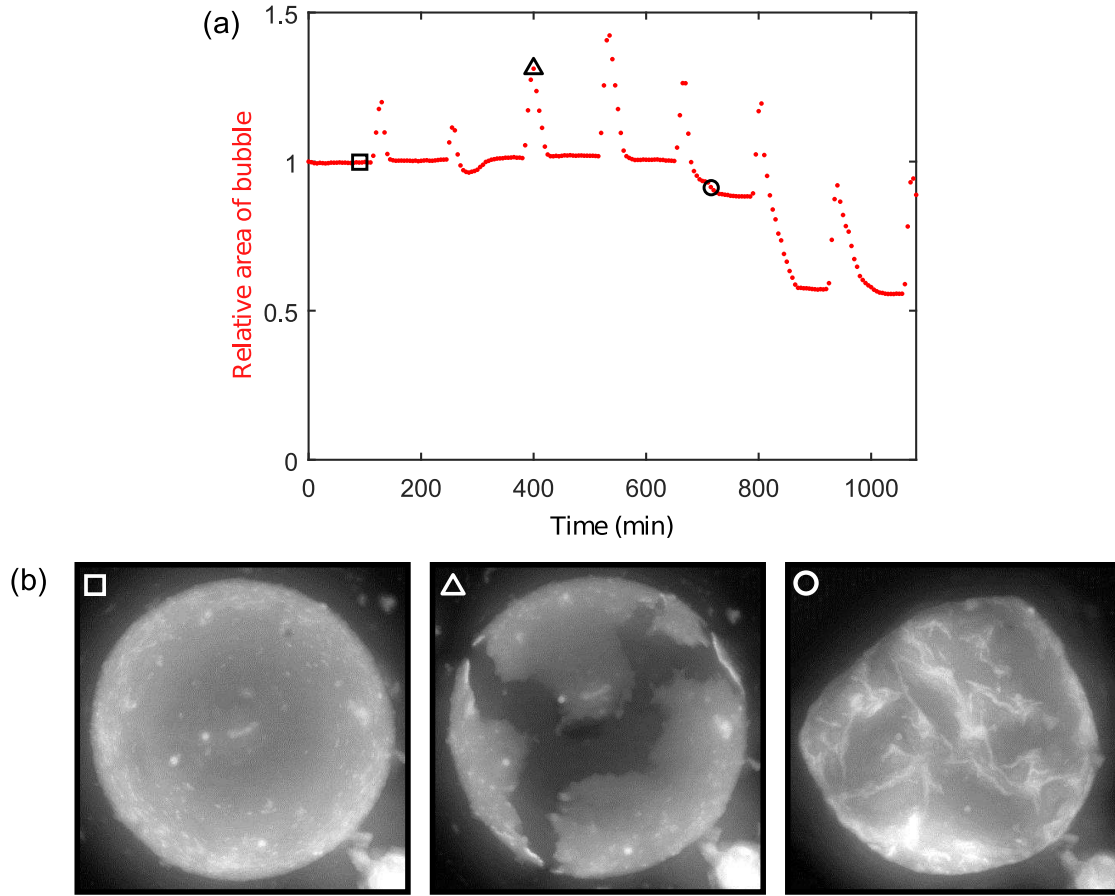


Figure 3.12: **(a)** Time evolution of the projected area of the armor submitted to the pressure profile presented in 3.11. The peaks correspond to the swelling periods. During the five first compression periods, the area stays stable. After the sixth step, the area plummets, which corresponds to the buckling event. **(b)** Epifluorescence micrographs of the armor at the different steps of testing: the blocked armor (\square , $R = 100 \mu m$), the appearance of fractures during the bubble swelling step (Δ), and finally the buckled armor (\circ). The corresponding symbols are reported on the graph above.

its apparent granular nature. These buckling events are shown in full in movie 4.

3.2.3 Mechanical strength characterization of armors

$\Delta P_{collapse}$ characterizes the resistance of each armored bubble against gas dissolution. We measure its value for a range of armor radii and three different particle sizes. The results are presented in figure 3.15. We first reproduce the same analysis as in previous papers [44, 16, 21] and plot $\Delta P_{collapse}$ as a function of the dimensionless parameter a/R , a being the radius of the particles and R the radius of the spherical armor in the jammed

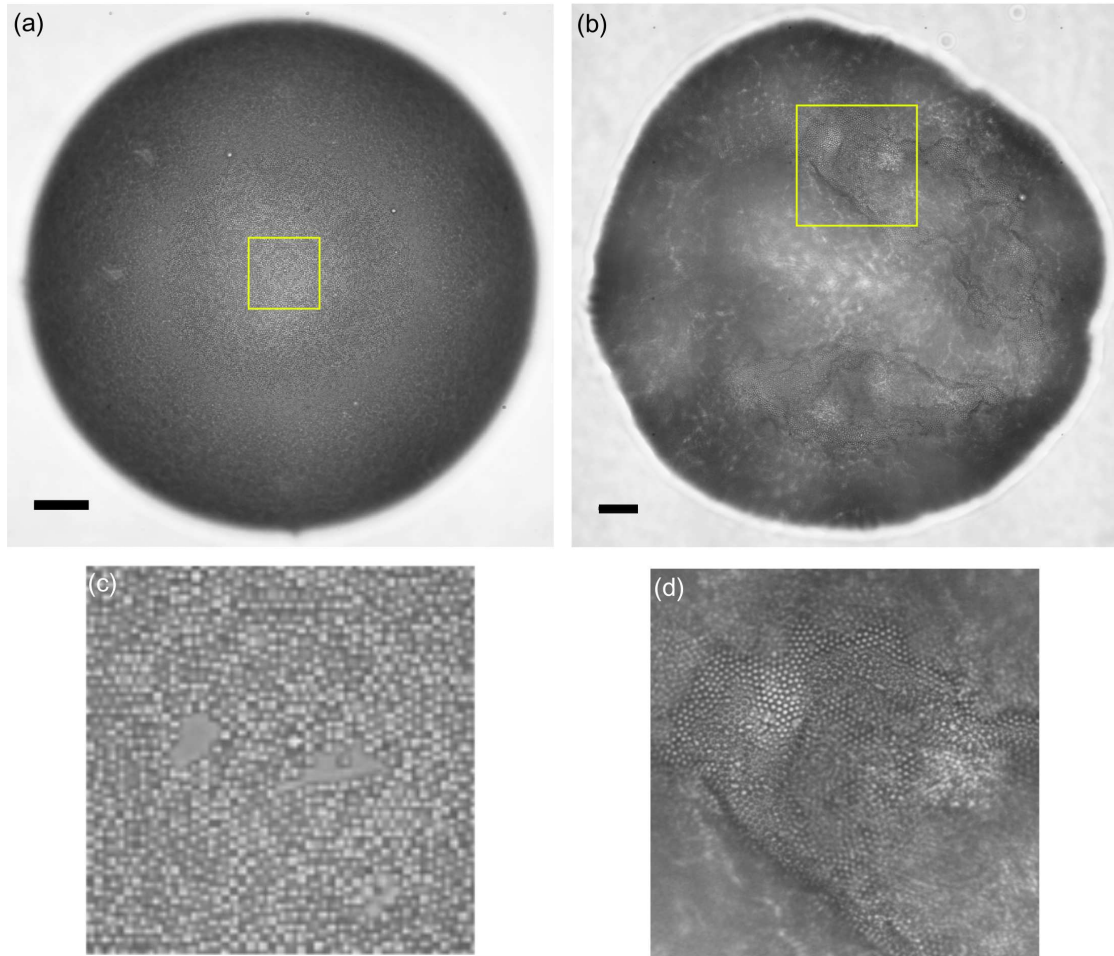


Figure 3.13: Detail of a buckling event for a bubble armored with $0.5\mu\text{m}$ particles. Scale bars are $20\mu\text{m}$. (a) Blocked armor before buckling. The yellow frame shows the enlarged area in (c). (b) Collapsed armor over the buckling threshold. The yellow frame shows the enlarged area in (d).

state before buckling occurs. The three sets of data, corresponding to particles with radii 0.5 , 1.1 and $4.5\mu\text{m}$, show different behavior and no clear conclusion can be drawn.

However, if $\Delta P_{collapse}$ is plotted against $1/R$, the points align together. We observe that $\Delta P_{collapse}$ decreases when the size of the shell increases. Indeed, a linear fit between $\Delta P_{collapse}$ and $1/R$ shows good agreement with the data up to $1/R \simeq 0.03\mu\text{m}^{-1}$, as shown by the black line. The slope of the fitted line is 104 mN/m , which corresponds to 1.5γ , where $\gamma = 70\text{ mN/m}$ is the estimated surface tension. A second striking observation is that despite a 9-fold increase in the particle diameter (from $0.5\mu\text{m}$ to $4.5\mu\text{m}$), the value of the collapse threshold barely changes. All the points lie on the same straight line,

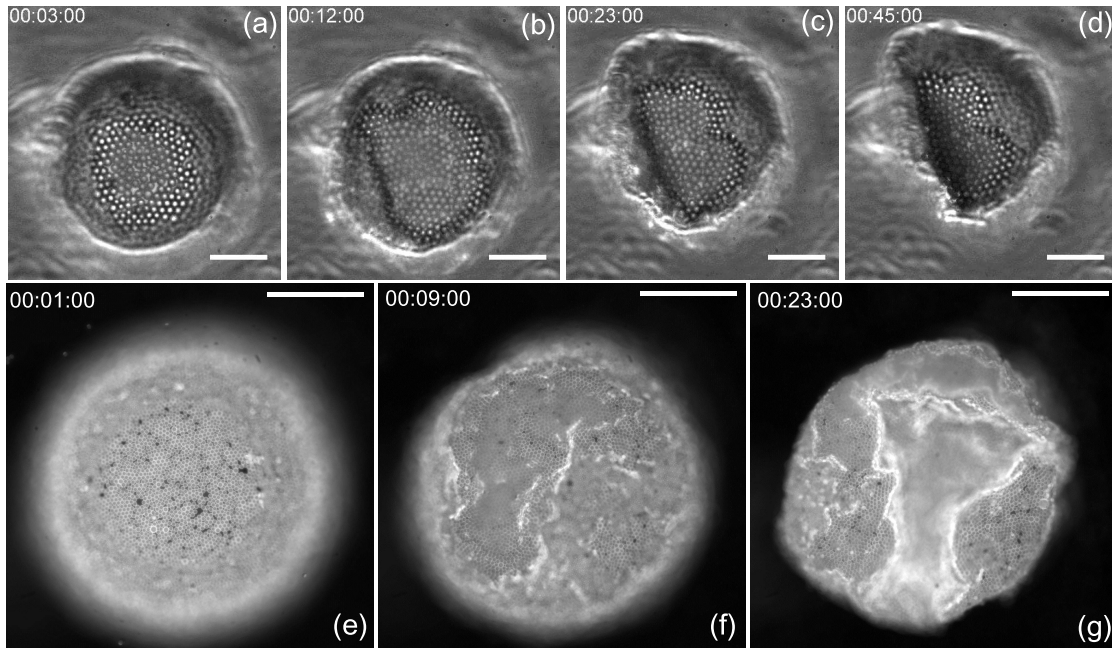


Figure 3.14: **(a-d)** Detail of a buckling event for a bubble armored with $4.5\mu\text{m}$ particles, illuminated in phase contrast. Scale bars are $30\mu\text{m}$. **(e-f)** Similar buckling event, with the same beads, in epifluorescence.

indicating that the particle size has a very weak influence on the mechanical resistance of the armor. As we will demonstrate in the next part, these two aspects are in very good agreement with the model that we develop.

The failure mechanism of the shell is catastrophic in the sense that once the threshold is reached, the buckled region grows until no gas is left inside the bubble, even for a fixed ΔP . However, if ΔP is decreased again to a negative value, the armor can re-swell and regain its mechanical rigidity in a non-buckled spherical state. This reversibility suggests that the liquid-gas contact line on the particles is pinned on the solid surface, which is confirmed by the fact that the particles never desorb from the interface: they stay attached together as a continuous granular material until the bubble has completely disappeared. These observations suggest that the air-water interface acts like a spring that pulls the armor back into place if the stress is released.

3.2.4 Onset of buckling

The buckling event seems initiated by bright lines that appear on the shell just before it starts to deform dramatically. These lines are clearly visible on figure 3.14. A closer look on these bright lines reveals that they are due to beads coming out of the plane of

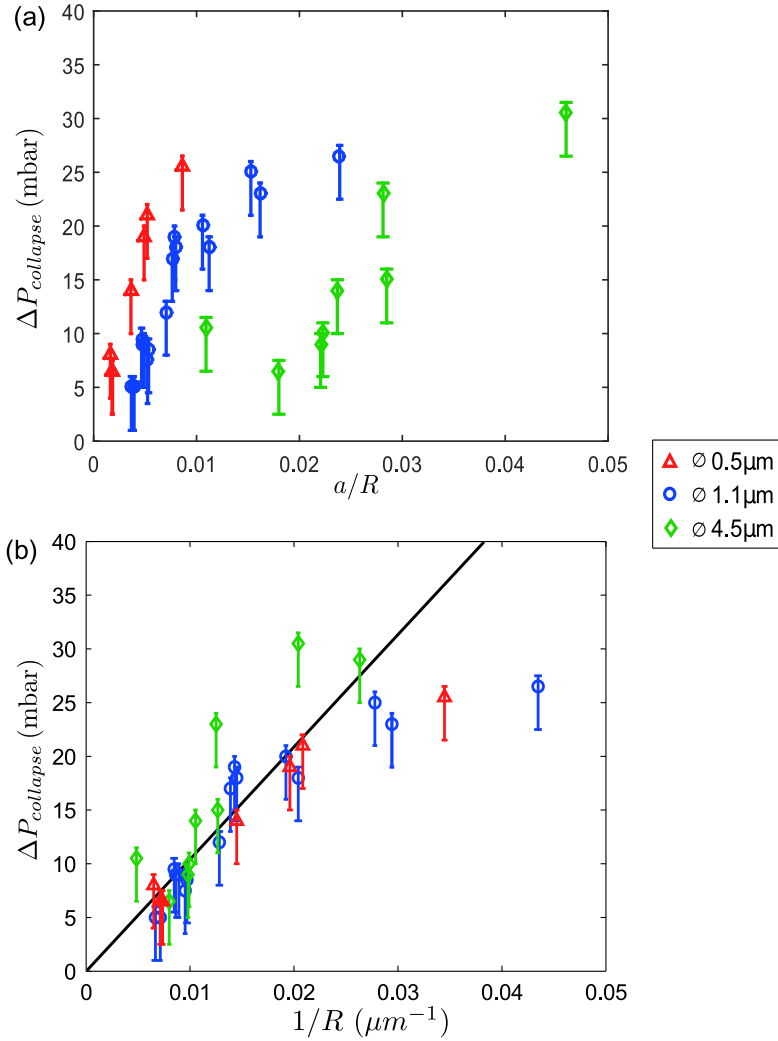


Figure 3.15: Plot of $\Delta P_{collapse}$ as a function of a/R in (a) and $1/R$ in (b), for three different particle diameters. The legend is common to the two plots. The error bars are estimated from the uncertainty in the measurement of P_{eq} and the size of the ΔP steps. The black line in (b) shows the linear fit excluding the two rightmost points.

the interface and overlapping, just at the beginning of collapse. As shown in figure 3.16 (corresponding to movie 5), beads are compressed against each other during dissolution, and when $\Delta P_{collapse}$, the stress is high enough to overcome the capillary force that maintains the beads on the interface. When this happens, beads overlap and buckling follows.

The local rise of fluorescence intensity when particles overlap is explained in figure 3.17. The observed fluorescence intensity is the result of the integral of light emission over the thickness of fluorescent material. When two beads stack up, their respective

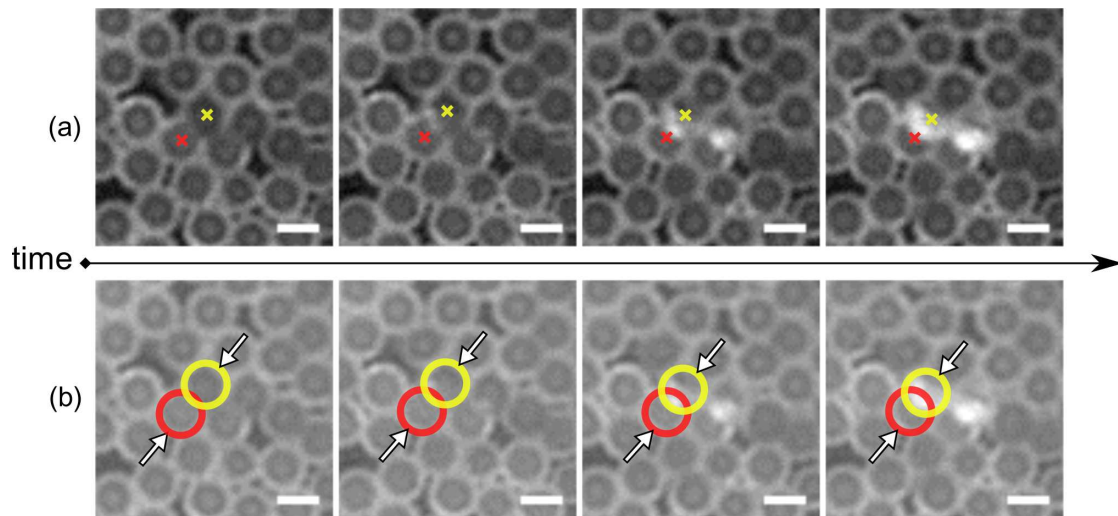


Figure 3.16: Onset of buckling of an armor composed of $4.5 \mu\text{m}$ particles. Row (a) is a close up on selected particles, within the armor of a collapsing bubble. The beads, marked by red and yellow cross are side by side at the beginning, and as the bubble dissolution progresses (from l. to r.), the centers get closer to each other and the beads overlap. Row (b) shows the same event, with the beads outlined in red and yellow. The direction of the compression is indicated by the white arrows. Scale bars are $5 \mu\text{m}$

fluorescence intensities add up, which results in a local increase in the brightness of the image.

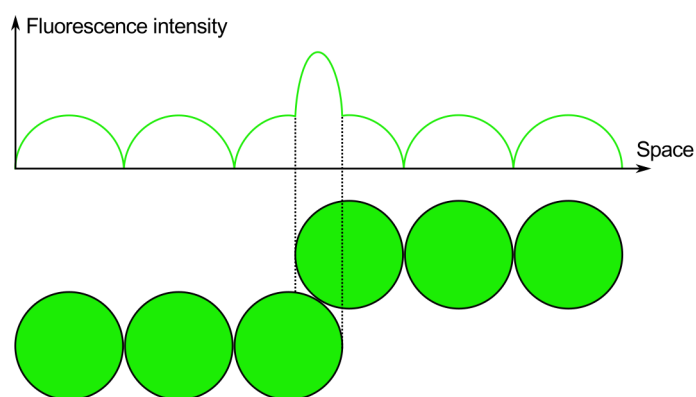


Figure 3.17: Side view of an overlap in the bead monolayer, at the onset of buckling. The graph above shows the corresponding fluorescence intensity.

3.2.5 Bubble inflation and cracks opening

When the bubble inflates during the periods of negative ΔP , a crack appears in the armor then closes again as ΔP returns to a positive value. This crack can take different orientations and differs strongly from the initial condition for the experiment where the particles were loosely packed (see figure 3.18). A possible explanation for the appearance of these cracks may be due to the fact that particles exhibit weak close range attractive interaction through the liquid. Indeed, since $\theta_P \approx 30^\circ$, most of the particle volume is immersed in water when adsorbed at the surface of the bubble, so that two adjacent particles exhibit practically the same interaction as when they are in dispersion, when they come close to each other.

During the initial compression of the armor, the particles are forced to come into close contact, up to a point where they may adhere together, due to Van der Waals forces. When the pressure is decreased, the bubble swells and the particles are pulled appart. The armor yields following a fracture path where the adhesion between particles is weakest, opening the crack patterns we observe. This could possibly be a way to measure the force necessary to separate two adherent beads, and measure the potential interaction energy.

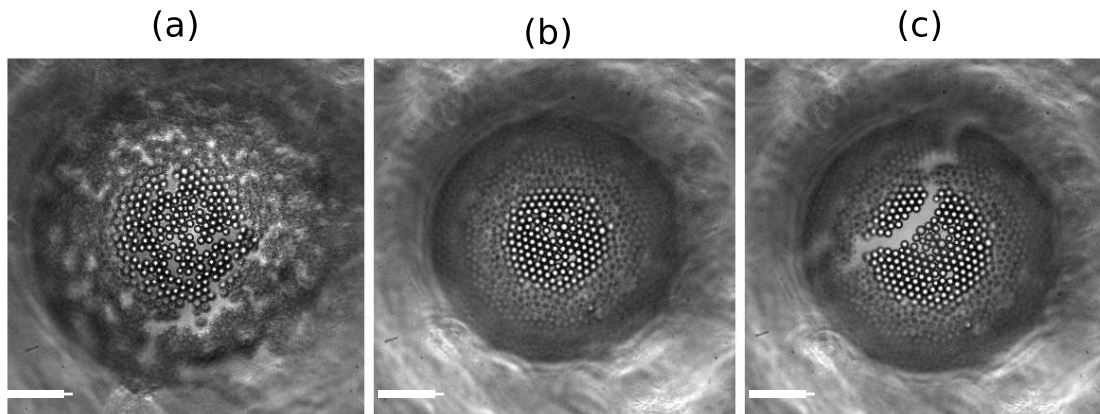


Figure 3.18: Different states of the armor during its probing. **(a)** Before the beginning of the pressure sequence, the particles are loosely packed and form small aggregates on the surface of the bubble. **(b)** During the first compression, the particles jam together and stay close packed, thus blocking the dissolution. **(c)** After the first pressure release, a crack opens in the shell in a well defined location, and the particles do not redisperse on the surface as they were in (a).

3.3 Armor with ellipsoidal colloids

We have shown in the previous sections that the robustness of the colloidal armors did not depend on the size of its constitutive particles. We propose here to investigate the effect of the shape of the particle. This drives us to test if the shape of the particles can have a measurable effect on the mechanical resistance of the armors.

The most intuitive particles shape to consider is that of a prolate ellipsoid. Adsorbed on fluid interfaces, ellipsoidal particles have already been proved to have very interesting properties [45]. Indeed, they have only one axis of symmetry instead of an infinity in the case of the sphere. This symmetry breakage induces a distortion of the interface in the vicinity of the particle: the air-water surface cannot remain flat and match the Young-Laplace contact angle on the circumference of the ellipsoid. In consequence, it adopts an undulated shape. This perturbation induces a long range capillary interaction between the adsorbed particles that is well approximated by the pair potential of two interacting elliptical quadrupoles [46], which includes attractive forces and torques. Thus, these ellipsoids can self assemble into chains with a certain level of mechanical rigidity. These results suggest that an armor made of ellipsoidal particles could have different properties, as evidenced in the case of emulsions [47].

The experimental protocol described previously is repeated with ellipsoidal particles to measure the $\Delta P_{collapse}$ of the shell. For all these experiments, the major axis of the ellipsoids is $2.5 \mu m$ long and the minor axis is $0.7 \mu m$, which corresponds to an aspect ratio of 3.5. Figure 3.19(a) shows that ellipsoidal particles adsorb the same way spherical colloids do. The magnified view shows the orientational order that arises, when particles align side by side. The results of the collapse pressure measurements are reported in figure 3.19(b).

Two observations can be made. First, the values of collapse pressure are lower than the collapse pressure with spherical beads. A linear regression on the points yields a slope of 56 mN/m , which is lower than the previous value (104 mN/m), indicating the the armors are weaker with ellipsoidal particles. Second, the data are more dispersed, which could be explained by the increased number of defects in the arrangement of ellipsoids in comparison with the packing of sphere. Indeed, since ellipsoids are anisotropic, an orientational order can arise in addition to the position order, and this could create weaknesses at the joints between regions of different orientations. Since the packing is random, the importance of these weaknesses vary from a bubble to another which explains the dispersion in the measurements.

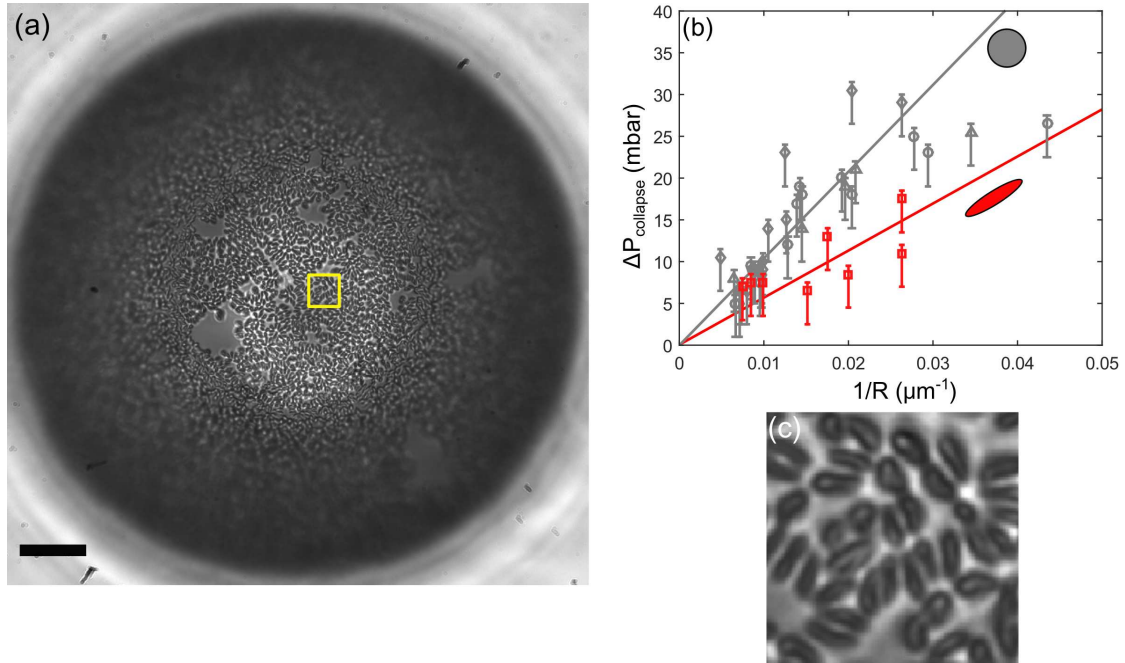


Figure 3.19: **(a)** Micrograph of a bubble partially covered with ellipsoidal particles. The yellow dotted frame shows the magnified area in **(c)**. Scale bar is $20 \mu m$. **(b)** Collapse pressure of armors constituted of anisotropic ellipsoidal particles (red squares). The values of $\Delta P_{collapse}$ for spherical particles, as well as their linear fit, are reported in gray for comparison.

3.4 Effect of surfactant on armor strength

In this section we take advantage of the design of the microfluidic channel to test the effect of an addition of surfactant in the environment of the armored bubble. The results are preliminary but it is observed that the effect of minute amount of surfactant can be drastic.

3.4.1 Effect of surfactant on the failure mode of the shell

We test the effect of the adjunction of a small concentration of sodium dodecyl sulfate (SDS) in the media surrounding the armored bubble. To do so, we produce a trapped armored bubble, according to the procedure described above. Once it is trapped in the observation chamber, a solution of SDS and sodium chloride is flown through the side channels connected to the pressure controller. The concentration of NaCl is kept at 0.5 mol/L, while the concentration of SDS can be varied. The flow rate is kept low (velocity around the bubble $< 100 \mu m$) to prevent any perturbation of the shell due to shear

stress. After a few minutes, the concentration of surfactant around the armored bubble is stabilized, it is then submitted to a low dissolution pressure $\Delta P = 3 - 5$ mbar to observe the failure mode.

A typical behavior is reported in figure 3.20 (see also movie 6), which correspond to a concentration of 100 ppm of SDS. For comparison, the critical micellar concentration (CMC) of this surfactant is 0.2%w/w=2000 ppm. The events following the jamming of the colloidal shell are radically different from the case without surfactant. The shell is unable to block the dissolution of the gas, even at such a low dissolution pressure (5 mbar). Particles desorb from the interface, so that the bubble retains its spherical shape as its volume is reduced, until it is completely dissolved. It can be seen on the video that the particles are 'ejected' one by one from the armor. This shows that even a very low concentration of surfactant is likely to compromise the stability of an armored bubble.

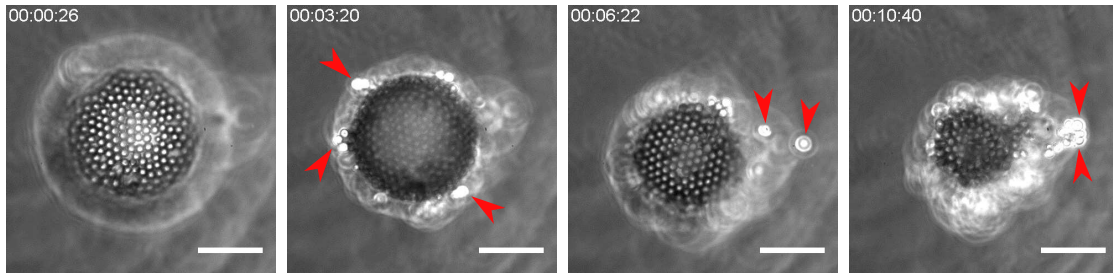


Figure 3.20: Failure of an armored bubble in a 100 ppm solution of SDS (at 0.5M NaCl). The volume of the bubble rapidly decreases when submitted to a low dissolution pressure $\Delta P = 3 - 5$ mbar. Some beads are desorbed from the shell (indicated by red arrows) and are advected by the weak flow maintained around the bubble. Scale bars are $30 \mu m$.

3.4.2 Effect of SDS concentration

We now vary the concentration of surfactant and observe the failure mode of the armor for a high value of $\Delta P = 50$ mbar $> \Delta P_{collapse}$. The results are reported in figure 3.21. For each concentration of surfactant, the shell is dissolved and the failure mode is classified either as buckling or desorption. For the bubble radii accessible to our experiment, an effect is visible only for traces of SDS (< 20 ppm). The large bubbles undergo a buckling instability, while the beads on the smaller ones are individually desorbed.

3.4.3 Possible interpretation

The weakening of the armor by surfactant can be explained by a simple mechanism. The concentration of SDS is well below the CMC (at least 100 times smaller), therefore the

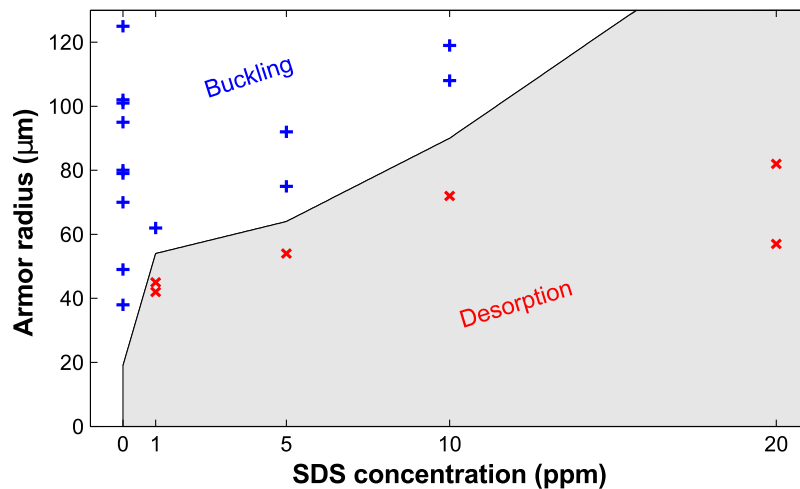


Figure 3.21: Phase diagram showing the failure mode as a function of the radius of the armor and the concentration of SDS.

surface tension of the liquid barely changes [48] However, the solid-liquid surface energy may change a lot, and thus change the contact angle of the water on the particles. Generally, surfactants have a detergent effect and increase the wettability of the solid, i.e. decrease the contact angle θ . The effect of a lowered θ on the morphology of the colloidal armor is shown on figure 3.22.

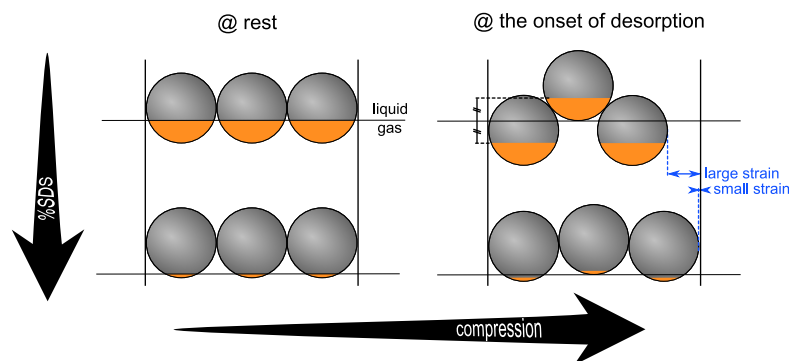


Figure 3.22: Sketch showing the effect of a diminution of θ when surfactant is added to the liquid. The particles are adsorbed at a lower penetration depth, and when the monolayer is compressed, they are likely to be ejected at a lower strain. The orange caps show the area of the sphere initially embedded in the bubble.

When the particles are jammed without compression ('at rest'), the depth of penetration of the beads is lower with a low contact angle. As the monolayer is compressed, it will eventually destabilize according to a high spatial frequency mode with alternating beads, as we will demonstrate in section 4.3. As this instability grows, the beads are

pushed against each other and away from the interface. Since the capillary restoring force is assumed to be symmetric, the beads above and below the interface undergo opposite displacements (as shown by the two equal segments in figure 3.22, top-right). If the strain is increased enough, the beads outside the bubble can eventually reach a point where they no longer intersect the plane of the interface, which is the onset of desorption. As shown on figure 3.22, the strain at which desorption happens is much lower when the θ is lower, ie. when the concentration of SDS increases. In that case, even a small distortion of the monolayer will lead to the loss of beads from the armor, which explains the failure mode observed when adding surfactant.

Finally, these results show that the sign of the electrical charge of the surfactant is paramount. Recent studies have used mixtures of colloids and surfactant to stabilize foams and emulsions [49, 31]. The idea is to use particles decorated with negative charges, and induce their hydrophobicity *in situ* with a surfactant. They either used carboxylate grafted latex (similar to the particle in our experiment) or negatively charged silica particles. A cationic surfactant (such as cetyltrimethylammonium bromide CTAB) is added, and is adsorbed on the oppositely charged surface of the particle, as depicted in the upper sketch in figure 3.23. The particle is thus rendered more hydrophobic, and its capacity to adsorb on interfaces is enhanced. However, in our case, we added SDS, an anionic surfactant. The polar heads of SDS are repulsed by the surface charge of the colloid and the effect is opposite: the particles become more hydrophilic (lower sketch of figure 3.23), and the contact angle θ decreases. This shows that the capacity of the particles to stabilize a bubble, and by extension, a foam, can change from one extreme to the other just by changing the charge of the surfactant dissolved in the dispersion. This effect is especially important since only a few ppm of surfactant are sufficient to induce dramatic effects.

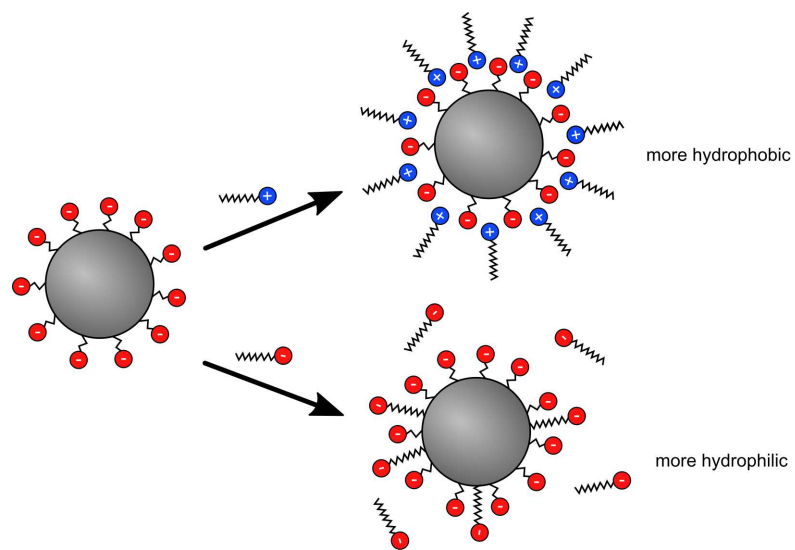


Figure 3.23: Schematic of the action of surfactant on a carboxylate grafted colloid. Cationic surfactant is attracted to the negatively charged surface of the colloid, which becomes decorated with the hydrophobic tails of the amphiphilic molecules, it becomes thus more hydrophobic. On the contrary, anionic surfactant molecules are repulsed, and their hydrophobic tail may be adsorbed on the surface of the colloid, which is natively hydrophobic (polystyrene). The particles are thus even more hydrophilic.

4

Interpretation of the behavior of colloidal armors

In this chapter, we interpret the results of the experiments on armored bubbles. First we explain in detail the meaning of the control parameter ΔP that is used to control the shrinkage or swelling of the bubble. For this, we use a classic thermodynamic model describing gas bubble nucleation in liquids. This analysis gives access to the relation between the externally imposed ΔP , and the free energy variation of the bubble when it dissolves into the water.

Then, we turn our attention to the mechanics of the shell. We show that it cannot be described as an elastic material, which is why we derive a new model based on the microscopic interactions between the beads. This description yields an expression of the cost in terms of mechanical energy to compress the armor. Comparing this cost with the thermodynamic gain of gas dissolution yields an expression of the theoretical value of the armor collapse pressure.

Finally, the mechanical resistance of an armor is compared to the stress it would undergo, should it be embedded in a real foam. To estimate the dissolution stress imposed by the surrounding foam, we use a classic model used to predict foam evolution. This enables us to show to what extent a particle stabilized foam is stable, given an

initial bubble size distribution.

4.1 Control of the bubble dissolution

In this section, we present the thermodynamic theory that explains how the behavior of the bubble is tuned by pressure adjustments. This theory is then used to derive a model that account for the collapse pressure measurements.

4.1.1 Gibbs theory of bubble nucleation

We give here the general idea that lies behind homogeneous nucleation theory. We focus on the case of an air in water bubble, for which an extensive calculation was made by Ward *et al.* [50].

Let us consider the transformation depicted in figure 4.1, where a gas bubble of radius r nucleates within a aqueous solution of the same gas.

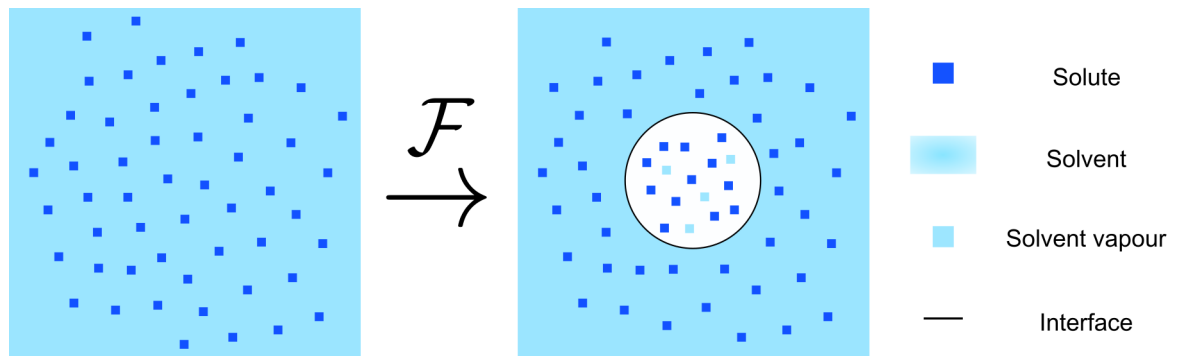


Figure 4.1: Schematic of the nucleation of a gas bubble in a weak gas-liquid solution. During the transformation, a spherical gaseous phase containing gas and solvent vapour appears within the solution.

Since this transformation occurs at constant temperature T , let us estimate the variation \mathcal{F} of Helmholtz free energy:

$$\mathcal{F} = \underbrace{\frac{4}{3}\pi r^3 \Delta h}_{\text{volume}} + \underbrace{4\pi r^2 \gamma}_{\text{surface}}. \quad (4.1)$$

The first term represents the bulk energy variation and is proportionnal to the volume of the spherical bubble. Δh is the energy per unit volume to evaporate gas and solvent molecules from the liquid phase to the gaseous phase inside the bubble. The second term

is the surface energy variation, proportionnal to the surface of the spherical bubble, γ being the surface energy or interfacial tension of the liquid-gas interface.

Let us now assume that there exists a value of the radius R_{eq} for which the bubble is in a state of thermodynamic equilibrium. It means that the free energy is extremum for this value of the radius:

$$\left. \frac{d\mathcal{F}}{dr} \right|_{R_{eq}} = 4\pi R_{eq}^2 \Delta h + 8\pi R_{eq} \gamma = 0 \quad (4.2)$$

$$(4.3)$$

and thus

$$R_{eq} = -\frac{2\gamma}{\Delta h}. \quad (4.4)$$

The expression of the free energy then reads:

$$\mathcal{F} = 4\pi\gamma \left(r^2 - \frac{2r^3}{3R_{eq}} \right) \quad (4.5)$$

The necessary condition for the existence of a physical R_{eq} is that $\Delta h < 0$. R_{eq} , and thus Δh , will be explicitly calculated in the next paragraph. Briefly, the condition $\Delta h < 0$ means that the solution of gas must be supersaturated, so that it is energetically favorable for gas molecules to go from the liquid phase to the gaseous one, regardless of the surface cost (ie: through a flat interface).

It is also worth noting that

$$\left. \frac{d^2\mathcal{F}}{dr^2} \right|_{R_{eq}} = -8\pi\gamma < 0, \quad (4.6)$$

which implies that the equilibrium is unstable, because the function $\mathcal{F}(R)$ is maximum for $R = R_{eq}$. Physically, this signifies that a bubble with $R > R_{eq}$ will swell, because it will reduce its free energy \mathcal{F} , and a bubble with $R < R_{eq}$ will shrink, because it will reduce its free energy as well.

This equilibrium radius R_{eq} is termed *Gibbs critical radius*. In the next paragraph, we explicitly calculate it in the case of weak ideal solutions of gas in water.

4.1.2 Calculation of R_{eq}

Considering a bubble of radius R_{eq} at equilibrium, we calculate the chemical potentials μ of the various components in the system. In the following, the subscripts 1 and 2 respectively denote the solvent (ie: water) and the solute (ie: air), while the superscripts ' and '' are used respectively for the components in the liquid phase and in the gaseous

phase.

In the liquid, the chemical potentials are [51]

$$\mu'_1 = \mu_{01}(P', T) - kTC' \quad (4.7)$$

$$\mu'_2 = \mu_{02}(P', T) + kT \ln \frac{C'}{C_{sat}} \quad (4.8)$$

where P' is the pressure in the liquid, T is the absolute temperature, k is the Boltzmann's constant, C' is the molecular concentration of gas dissolved in the liquid phase, C_{sat} is the equilibrium concentration in the liquid saturated with the gas through a flat interface, and μ_0 are the reference chemical potential for the considered pressure and temperature of the pure components. If the solvent is considered incompressible, μ'_1 rewrites

$$\mu'_1 = \mu_{01}(P_\infty, T) + \int_{P_\infty}^{P'} v'_1 dP - kTC' \quad (4.9)$$

$$= \mu_{01}(P_\infty, T) + v'_1(P' - P_\infty) - kTC' \quad (4.10)$$

where P_∞ is the saturation vapor pressure of the pure solvent, and v'_1 its molar volume.

For an ideal solution, the chemical potentials in the bubble are [52]

$$\mu''_1 = \mu_{01}(P_\infty, T) + kT \ln \frac{P''}{P_\infty} + kT \ln \frac{1}{1 + C''} \quad (4.11)$$

$$\mu''_2 = \mu_{02}(P', T) + kT \ln \frac{P''}{P'} + kT \ln \frac{C''}{1 + C''} \quad (4.12)$$

where C'' is the molecular concentration of gas inside the bubble.

Laplace's law gives the pressure difference between the inside and the outside of the bubble:

$$P'' - P' = \frac{2\gamma}{R_{eq}}. \quad (4.13)$$

At equilibrium, the chemical potential of the respective components are equal, thus:

$$\mu'_1 = \mu''_1 \iff \frac{P''}{1 + C''} = P_\infty \exp\left(\frac{v'_1(P' - P_\infty)}{kT} - C'\right) \equiv P_\infty \eta \quad (4.14)$$

$$\mu'_2 = \mu''_2 \iff P'' \frac{C''}{1 + C''} = P' \frac{C'}{C_{sat}}. \quad (4.15)$$

The parameter η (see equation (4.14)) is *a priori* unknown, but it can be estimated in the case of our experiment. We use DI water at $T = 50^\circ\text{C}$. The pressure controller we use covers a range of pressure from 0 to 300 mbar, ie: $101.5 \text{ kPa} < P < 131.5 \text{ kPa}$. The saturation pressure of water at this temperature is 12.3 kPa, the saturation concentration

of air in water is 1.22×10^{-5} , so $0 < C' < 1.22 \times 10^{-5}$, and finally the molecular volume of water is $v'_1 = 3.02 \times 10^{-29} \text{ m}^3$. Therefore, we calculate that $1.0006 < \eta < 1.0008$, and conclude that we can safely assume $\eta \approx 1$.

Finally, summing equations (4.14) and (4.15) gives

$$P'' = P_\infty + P' \frac{C'}{C_{sat}}. \quad (4.16)$$

Combining this with (4.13) and rearranging yields an expression of the critical radius:

$$R_{eq} = 2\gamma \left[P_\infty + P' \left(\frac{C'}{C_{sat}} - 1 \right) \right]^{-1}. \quad (4.17)$$

As stated before, this value of R_{eq} entirely determine the fate of an air bubble of radius R . R_{eq} depends only on the ambient pressure $P' \equiv P$, the dissolved gas concentration C' , and some thermodynamic constant P_∞ and C_{sat} that depend only on the temperature.

4.1.3 Expression of the free energy of the dissolving bubble

Under the assumption of a weak air in water solution, the equilibrium saturation concentration of gas dissolved in the liquid through a flat interface is proportionnal to the partial pressure of that gas. This is known as Henry's law, expressed as $C_{sat} = K_H P$, where K_H is the Henry constant. This gives a new expression of the critical radius:

$$R_{eq} = 2\gamma \left[P_\infty + \frac{C'}{K_H} - P \right]^{-1}. \quad (4.18)$$

In practice, the radius R of the studied bubble is prescribed at the beginning of the experiment. In the thermodynamic condition of the observation chamber, it will swell or shrink depending on the sign of $R - R_{eq}$. However, since the pressure is controlled, it is possible to adjust P so that this prescribed initial radius matches a condition of thermodynamic equilibrium. For this particular value of the pressure P_{eq} we have

$$R = 2\gamma \left[P_\infty + \frac{C'}{K_H} - P_{eq} \right]^{-1} \quad (4.19)$$

Note on the influence of temperature: At this point, we notice that if the temperature of the system T is increased, P_∞ increases and K_H decreases, which means that for a given R , P_{eq} increases. For this reason, we choose to regulate the temperature of our experiments to 50.0°C . This way, our working pressure is raised around 70 mbar, in the middle of the range of the pressure controller (0-300 mbar). This gives a better precision and a finer control over the bubble dissolution.

Combining equation (4.19) with equation (4.18), and noting $\Delta P = P - P_{eq}$ yields

$$R_{eq} = 2\gamma \left[\frac{2\gamma}{R} - \Delta P \right]^{-1}. \quad (4.20)$$

This expression can be plugged into (4.5) to obtain the expression of the Helmholtz free energy of the studied bubble.

$$\mathcal{F} = 4\pi\gamma r^2 \left(1 - \frac{2r}{3R} + \frac{r\Delta P}{3\gamma} \right), \quad (4.21)$$

where R is the initial radius of the bubble for which P_{eq} was measured, and r is a variable radius used to estimate the free energy variation of the bubble, and thus predict the behavior of the bubble in the vicinity of $r = R$.

This equation is plotted in figure 4.2 for different values of ΔP . For $\Delta P = 0$, the bubble of radius R is in an unstable equilibrium state, for which \mathcal{F} is maximum (black curve). If ΔP is increased to a positive value, the \mathcal{F} curve shifts to the right, and the bubble is no longer at equilibrium (red curve). The system will decrease its free energy by dissolving the gas into the water thus reducing the bubble radius. Conversely, if ΔP is decreased to a negative value, the opposite transfer will take place and the bubble will swell (blue curve).

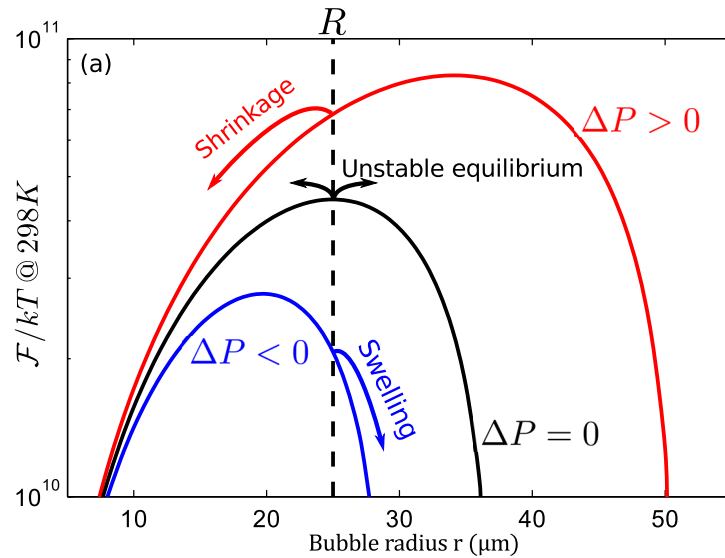


Figure 4.2: Free energy of a single gas bubble of radius R in a weak gas-liquid solution. If $\Delta P = 0$, the bubble radius is stationary. The bubble shrinks if $\Delta P > 0$ and it swells if $\Delta P < 0$, due to gas exchange between the liquid and the bubble.

This control of the bubble size through pressure control closely mimics the exchange

that takes place because of the over- or under-pressure experienced by each bubble in a foam [53, 54]. This analogy will be explored in greater details in section 4.5

4.2 Comparison to models of elastic shell

Our experiments provided a quantitative measurement of the maximum pressure that an armor can withstand before buckling. A direct approach to describe the behavior of these armors would be to model them as spherical hollow capsule made of some elastic material. The buckling of these spherical vessels is an old problem that has been studied extensively a long time ago [55, 56]. The buckling threshold of a sphere depends on its geometry, and on the properties of the shell material. Letting aside the influence of the Poisson modulus, the only material parameter that comes into play is the elastic Young modulus E . The expression of the buckling threshold pressure ΔP_E in this elastic approximation is

$$\Delta P_E \propto E \left(\frac{t}{R} \right)^2 \quad (4.22)$$

where R is the radius of the hollow shell, and t its thickness.

An elastic description of a particle covered interface has already been built in several studies [20, 15, 57, 25]. The resulting scaling laws are:

$$E = \frac{\gamma}{a} \quad \text{for the Young modulus} \quad (4.23)$$

$$B = \gamma a^2 \quad \text{for the bending modulus} \quad (4.24)$$

A scaling for the bending modulus of a sheet of thickness t is $B \propto Et^3$. If we consider that the equivalent thickness of the covered interface is equal to the diameter a of the particles, ie. $a \propto t$, we have

$$E \propto \frac{B}{a^3} \propto \frac{\gamma}{a}. \quad (4.25)$$

This suggests that the surface tension provides the restoring force that explains the elasticity of coated interfaces.

Combining these two scaling laws, and assuming again $t \equiv a$, should lead to a description of the buckling of the armored bubble, that is

$$\Delta P_E \propto \frac{\gamma a}{R^2}. \quad (4.26)$$

We shall now compare this prediction to our experimental results.

First, we estimate the order of magnitude of the expected buckling threshold (as will be shown later, the dissolution pressure ΔP is equivalent to a mechanical external

compression of the shell of the same magnitude, ΔP). We have $0.5\mu m < a < 4.5\mu m$, $23\mu m < R < 206\mu m$, and $\gamma = 0.07 N/m$. Therefore, computing the expected extremum values from those experimental data, ΔP_E should lie within the range 0.03-2.2 mbar. Experimentally, we rather measure collapse pressure between 5 mbar and 30 mbar.

Second, the expected scaling with respect to shell radius R is not what is observed experimentally. Rather than a -2 exponent, a simple inverse law seems more adapted, as shown in figure 3.15.

Third, $\Delta P_{collapse}$ is nearly independent of the diameter of the particles that make up the armor: a variation of a factor 9 in particle diameter leads to only a minor variation in the measured collapse pressures. This is in complete discrepancy with the elastic model, which predicts that the buckling pressure should be proportionnal to the diameter of the particles.

For these reasons, we conclude that a description of an armored bubble in term of an elastic hollow capsule is not adapted, which justifies the development of the model that is now presented.

4.3 Modeling the armor behavior

We now seek a model to predict the threshold value of ΔP at the onset of collapse of the colloidal shell, as well as the buckling mode. To do so, we consider a spherical shell of radius R that undergoes an infinitesimal isotropic compression (radius variation δR). This allows us to calculate the energy variation (W_{diss}) due to the gas dissolution in the liquid and compare it to the energetic cost of buckling the shell (W_{shell}), as detailed below.

4.3.1 Dissolution energy

We suppose that the shell of initial radius R is slightly compressed, which leads to a small radius variation δR . This volume variation δV of the shell corresponds to the dissolution of the same volume of gas into the surrounding water. The energy variation associated with the dissolution can be readily computed using equation (4.21). We define W_{diss} as the dissolution energy divided by the surface area of the shell. At first order we have:

$$W_{diss} = \frac{1}{4\pi R^2} \delta R \left. \frac{\partial \mathcal{F}}{\partial R} \right|_{r=R} = \Delta P \delta R. \quad (4.27)$$

This result is equivalent to saying that the shell is submitted to an external overpressure ΔP , the work of which (W_{diss}) is estimated over the compression δR . Note that ΔP here is the departure from the equilibrium pressure ($P - P_{eq}$) and that this result does

not require any knowledge of the pressure within the bubble. This result is in agreement with the expected behavior of the bubble: the spontaneous evolution of the system is given by the situation where $W_{\text{diss}} < 0$. If $\Delta P < 0$, then $\delta R > 0$ (swelling), and if $\Delta P > 0$ then $\delta R < 0$ (shrinking)

4.3.2 Shell deformation energy

Reduction of the problem

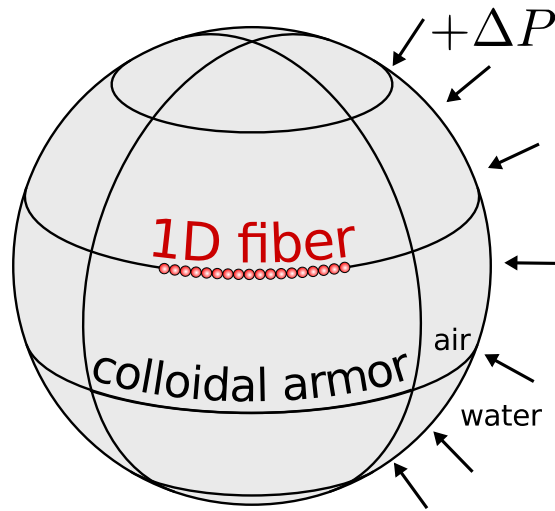


Figure 4.3: Sketch of the colloidal armor with an arbitrary 1D fiber highlighted in red. The air in water bubble is submitted to positive dissolution pressure $\Delta P > 0$.

In order to estimate the energetic cost of deformation of the shell W_{shell} per unit surface, we reduce the problem to the more tractable study of a 1D fiber, as depicted on figure 4.3. This fiber is an arbitrary line of N rigid beads of diameter a taken on the shell surface, having a total length L and width a . These beads are adsorbed on the liquid-gas interface, resulting in a radial restoring force that tends to hold the beads at an equilibrium position, defined here at $z = 0$ (figures 1.1 and 4.4). z is the depth of penetration of the particle into the fluid interface, and quantifies the out-of-plane displacement of the bead.

Capillary restoring force on one bead

The expression of the energy associated with this capillary restoring force has been derived previously [12]. Indeed, the energy of a single bead trapped on a fluid-fluid

interface minus the energy of the same bead completely immersed in the liquid is [12]

$$\Delta E = \pi a z (\gamma_{sv} - \gamma_{sl} - \gamma_{lv}) + \pi z^2 \gamma_{lv}, \quad (4.28)$$

where z is the depth of penetration of the bead into the fluid interface. This energy profile is plotted in figure 1.1. The equilibrium position for which ΔE is minimum is attained for $z_0 = (1 - \cos \theta)a/2$ (using the Young-Dupré relation), and the value of the minimum is $\Delta E_{min} = -\pi \gamma z_0^2$. The energy variation $\Delta E - \Delta E_{min} = w_\gamma^i$, that is the capillary potential energy for each bead i , for a vertical displacement $z - z_0 = \delta z_i$, can then be written as:

$$w_\gamma^i = \pi \gamma \delta z_i^2. \quad (4.29)$$

Buckling of the fiber

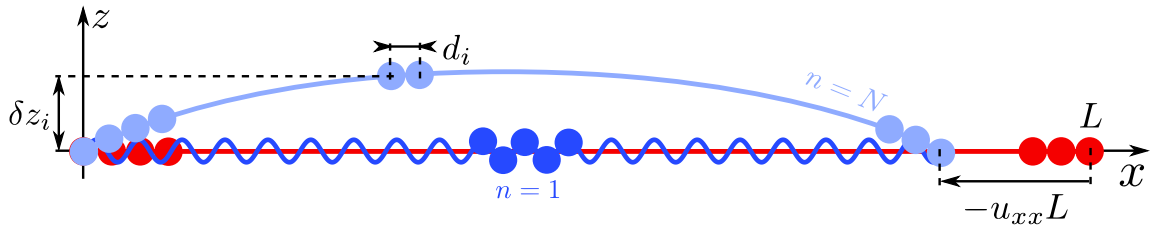


Figure 4.4: Sketch of the buckling of the fiber. The red line shows the undeformed initial state of the fiber of length L , the blue lines are the deflected sinusoidal states. Light blue is the lowest frequency mode, dark blue the highest frequency mode with alternating beads.

The compression of the armor reduces its radius and leads to a longitudinal compression of the fiber, which results in an uniaxial strain u_{xx} . Since the beads are rigid, they must move out of the plane of the shell to comply with the x-axis displacement. A sinusoidal profile of amplitude A is assumed to describe the out-of-plane displacements of the beads along the fiber, as shown on figure 4.4. The expression of the deflection δz_i of each bead i as the following form:

$$\delta z_i = A \cos \left(\frac{\pi i}{n} \right) \quad \text{with } n \in \mathbb{N}, n \in [1, N]. \quad (4.30)$$

The lowest possible spatial frequency is attained for $n = N$, where N is the total number of beads in the fiber. It corresponds to a low curvature of the fiber, and is what would be expected in the case of the Euler buckling of an elastic beam. The highest spatial frequency with $n = 1$ translates the case for which the particles alternate between only

two positions, at a fixed distance above and below the interface plane.

We now seek to calculate the strain. For this we first compute the longitudinal (x-axis) distance d_i between two adjacent beads i and $i + 1$ at different deflections (z-axis), for a very small deflection $A \ll a$. A close-up of the two considered bead is sketched in figure 4.5. Using the Pythagorean theorem:

$$\begin{aligned} d_i &= \sqrt{a^2 - A^2 \left[\cos\left(\frac{\pi i}{n}\right) - \cos\left(\frac{\pi(i+1)}{n}\right) \right]^2} \\ &\simeq a \left(1 - \frac{A^2}{2a^2} \left[\cos\left(\frac{\pi i}{n}\right) - \cos\left(\frac{\pi(i+1)}{n}\right) \right]^2 \right). \end{aligned}$$

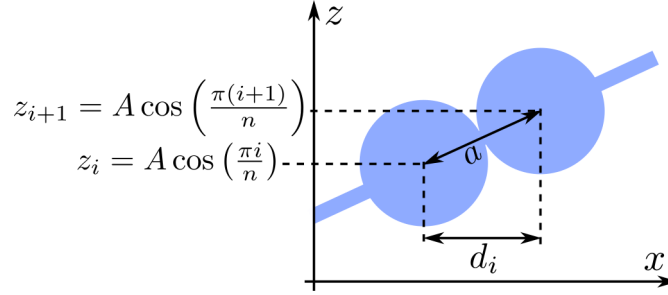


Figure 4.5: Close-up of the geometrical construction used to calculate d_i .

Summing this expression, we obtain the length of one period of the deformed fiber projected along the x-axis:

$$\begin{aligned} \sum_{i=1}^n d_i &= an - \frac{A^2}{2a} \sum_{i=1}^n \left[\cos\left(\frac{\pi i}{n}\right) - \cos\left(\frac{\pi(i+1)}{n}\right) \right]^2 \\ &= an - \frac{nA^2}{2a} \left(1 - \cos\left(\frac{\pi}{n}\right) \right). \end{aligned}$$

The initial length (ie: before compression) of this period of fiber was an . Therefore, the strain is:

$$u_{xx} = \frac{\sum_{i=1}^n d_i - an}{an} = -\frac{A^2}{2a^2} \left(1 - \cos\left(\frac{\pi}{n}\right) \right). \quad (4.31)$$

The strain of any fiber of an isotropically deformed sphere can be calculated easily. For instance on figure 4.6, we have $u_{xx} = (L' - L)/L$. Since $L = \Omega R$ and $L' = \Omega(R + \delta R)$, we simply end up with $u_{xx} = \delta R/R$ for any arbitrary fiber in the sphere. The total energy cost per unit surface area W_{shell} of the deformed shell can now be estimated by summing the energies necessary to displace each bead, over one period of the sinusoidal deflection. The initial apparent surface of the fiber is $n \times a^2$. Using equations (4.29) and (4.30) we

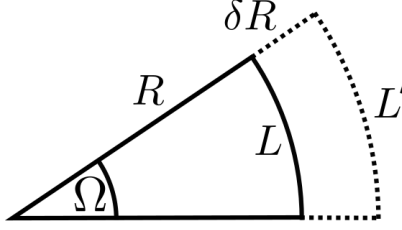


Figure 4.6: Strain of a radially extended fiber.

have:

$$W_{\text{shell}} = \sum_{i=1}^n \frac{w_{\gamma}^i}{n \times a^2} \quad (4.32)$$

$$= \frac{\pi\gamma}{na^2} \sum_{i=1}^n A^2 \cos^2\left(\frac{\pi i}{n}\right) \quad (4.33)$$

$$= \frac{A^2\pi\gamma}{2na^2} \quad (4.34)$$

Combing this last equation with equation (4.31) to express A in terms of u_{xx} , and noting that $u_{xx} = \delta R/R$, yields:

$$W_{\text{shell}} = -\frac{\pi\gamma\delta R}{R(1 - \cos(\frac{\pi}{n}))}. \quad (4.35)$$

4.4 Synthesis and model final prediction

The energy cost and the energy gain upon an infinitesimal compression of the shell are now calculated. These expressions, (4.27) and (4.35), can be used to calculate the buckling threshold of the shell. The total energy variation of the system upon compression is $W_{\text{diss}} + W_{\text{shell}}$. If this sum is negative, then the deformation of the shell described above is favorable and the mechanical stability of the shell will be lost. The equation $W_{\text{diss}} = -W_{\text{shell}}$ then gives an expression of the pressure buckling threshold, that is:

$$\Delta P_n^* = \frac{\pi\gamma}{R(1 - \cos(\frac{\pi}{n}))}. \quad (4.36)$$

This equation predicts different threshold pressures depending on the buckling mode n . The lowest threshold ΔP^* is attained for $n = 1$, which corresponds to the smallest possible wavelength, where beads alternate below and above the plane of the air-water

interface. In this situation, the value of the threshold is

$$\Delta P_1^* = \frac{\pi\gamma}{2R} \simeq 1.57 \frac{\gamma}{R}. \quad (4.37)$$

This prediction is in very good agreement with our experimental observations. As shown on figure 4.7, the data align on the model curve, with no fitting parameter.

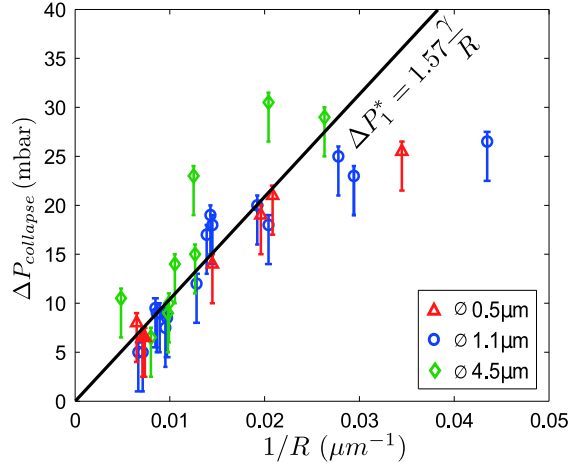


Figure 4.7: Experimental values of $\Delta P_{collapse}$, reported with the values predicted by the model ΔP_1^* (solid black line).

First, the scaling of ΔP^* with the bubble radius as $1/R$ is the scaling law that is observed experimentally. The model also predicts a slope of 1.57γ , while the slope measured experimentally is 1.63γ , which is very close. Second, the value of the particle radius a does not appear in the expression of ΔP_1^* , an independence which is also evidenced by the experimental data. Third, the most unstable mode is predicted to be $n = 1$, which corresponds to the highest available spatial frequency with alternating beads. Thus, the deformation of the shell at the onset of buckling should be very localized and should occur at the scale of individual beads, rather than at the scale of the whole shell, as it would be expected in elastic buckling. This behavior is observed experimentally, as localised dislocations between adjacent beads emerge just before buckling (see figure 3.16 and movie 5). These dislocations consist in neighbouring beads coming out of the plane of the interface and overlapping with each other. Once such a dislocation appears, the shell loses its mechanical stability, in the same fashion as a bridge's arch (see figure 4.8).

This model thus completely captures the mechanics of the armor. The consideration of very simple microscopic elements, namely hard spheres compressed against each other and trapped by capillary springs, are sufficient to precisely describe the behavior of the whole mesoscopic armored bubble. The model accounts for the unusual aspect of the



Figure 4.8: The stability of the bridge is compromised by the dislocation of one stone.

buckling of the colloidal shells, in terms of scaling, order of magnitude, and independence with respect to the particle size.

Indeed, as explained earlier in section 4.2 the behavior of armored bubbles is fundamentally different from what would be obtained with an elastic hollow shell [56]. In the continuous elastic case, the deformation energy cost would be proportionnal to the squared mean curvature of the deflection, rather than the squared amplitude, as for the rigid particles. This would lead to $W_{\text{shell}}^{\text{elast}} \propto u_{xx}/n^2$, which leads to a least energetic cost when n is maximum, that is to say for large wavelength deformation, as in the classical Euler buckling. Moreover, the critical pressure would scale with $1/R^2$ [56] also contrasting with our measurements.

4.5 Prediction of the behavior of the armor within a foam

In this section we take advantage of the fine predictions on individual armored bubble to predict the behavior of a particle-stabilized foam. We combine a classic foam evolution model [53] with our armor resistance measure to predict the fate of each bubble within the foam.

4.5.1 Lemlich model

To probe the mechanical properties of the shell in the previous section, the ambient pressure in the microfluidic chip is imposed externally through a pressure controller. In a foam, each bubble is subjected to a dissolution pressure ΔP_{foam} imposed by the surrounding bubbles. Indeed, when two bubbles of different radii come in close proximity, the difference in internal Laplace pressure drives a flux of gas from the small bubble to the large bubble. In a foam, each bubble has several neighbours, and interact with each

of them, creating very complex coupling. This phenomenon is called Ostwald ripening and is one of the main foam coarsening process.

Lemlich [53] used a mean-field approximation to simplify the problem and estimate the flux of gas in or out of a bubble. He assumed that the bubble interacts with the surrounding liquid, and not directly with the neighbouring bubble. The surrounding liquid is in turn assumed to be in equilibrium with a fictitious bubble of radius $R_{Lemlich}$, so that the pressure difference between a bubble of any size R and the liquid is

$$\Delta P_{foam} = 2\gamma \left(\frac{1}{R} - \frac{1}{R_{Lemlich}} \right). \quad (4.38)$$

This pressure difference can also be viewed as the dissolution pressure experienced by each bubble in the foam. From Fick's law, one can compute the flux of gas J from each bubble:

$$J = KA\Delta P_{foam}, \quad (4.39)$$

where K is the effective bubble gas permeability. Assuming that the surface over which the exchange is taking place can be approximated with $S = 4\pi R^2$, one gets the rate of variation of the mass of the bubble:

$$\dot{m} = 8\pi\gamma K \left(R - \frac{R^2}{R_{Lemlich}} \right). \quad (4.40)$$

By assuming the conservation of the number of gas moles in the whole foam, the summation of equation (4.40) taken over every bubble in the foam must be null. Therefore,

$$\sum n(R) \left(R - \frac{R^2}{R_{Lemlich}} \right) = 0, \quad (4.41)$$

where $n(R)$ is the total number of bubbles of radius R in the foam. The number of bubbles in a typical sample is high. For instance 1 mL of foam with an air fraction of 0.64 (which is the limit between a dry and a wet foam) and bubbles of radius $R = 100 \mu m$ contains approximately 160'000 bubble. As a consequence, it is reasonable to consider a continuous distribution of bubble sizes, whose density probability function is $F_l(R)$. With this in mind, an expression of $R_{Lemlich}$ is

$$R_{Lemlich} = \frac{\int_{r=0}^{+\infty} r^2 F_l(r) dr}{\int_{r=0}^{+\infty} r F_l(r) dr}. \quad (4.42)$$

In this model, the behavior of a single bubble of radius R in a foam depends on the radii distribution of the whole population. If $R < R_{Lemlich}$, then it experiences a dissolution pressure $\Delta P_{foam} < 0$, consequently the bubble will dissolve and shrink.

Conversely, if $R > R_{Lemlich}$, it will swell.

In the same way, for a single bubble of radius R immersed in water in our microfluidic device, $R_{eq}(P)$ is the radius of the bubble that would be in equilibrium with the liquid for a given pressure P , temperature, and dissolved gas concentration C . Equation (4.20) gives the expression of the dissolution pressure in the chamber:

$$\Delta P = 2\gamma \left(\frac{1}{R} - \frac{1}{R_{eq}(P)} \right), \quad (4.43)$$

which is equivalent to the pressure felt by a bubble in a foam where we would have $R_{eq} \equiv R_{Lemlich}$. This shows that our device simulates the environment of a 'Lemlich foam', with $\Delta P \equiv \Delta P_{foam}$.

4.5.2 Comparison with armor strength

In Lemlich's model, the behavior of any armored bubble within a foam is only a function of its own radius, and of $R_{Lemlich}$, which is itself a function the probability density function of the radii distribution. A common way of characterizing the bubble size distribution in a foam is, beside the average radius value, to use the polydispersity P . It is defined as the standard deviation normalized by the mean of the distribution:

$$P = \frac{\sqrt{\langle (R - \langle R \rangle)^2 \rangle}}{\langle R \rangle} \quad (4.44)$$

where $\langle \rangle$ denotes the mean over every bubble in the foam. Moreover, the expression of the polydispersity gives :

$$\mathcal{P}_d^2 = \frac{\int_{r=0}^{+\infty} (r - \langle R \rangle)^2 F_l(r) dr}{\langle R \rangle^2} \quad (4.45)$$

$$= \frac{\int_{r=0}^{+\infty} r^2 F_l(r) dr - 2 \langle R \rangle \int_{r=0}^{+\infty} r F_l(r) dr + \langle R \rangle^2}{\langle R \rangle^2} \quad (4.46)$$

$$= \frac{\int_{r=0}^{+\infty} r^2 F_l(r) dr}{\langle R \rangle^2} - 1 \quad (4.47)$$

The polydispersity is therefore linked to the Lemlich radius through

$$R_{Lemlich} = \langle R \rangle (1 + P^2). \quad (4.48)$$

For a given average radius, the higher the polydispersity, the higher the Lemlich radius. To set these ideas, let us estimate the behavior of bubbles in foams of increasing poly-

dispersity. We use log-normal distributions of constant mean, but we vary the standard deviation. Log-normal distributions are commonly use to describe bubble size distribution in a foam [7]. One of their advantages over gaussian distributions is that they do not take negative values. Figure 4.9 shows plots of the distributions used, with a mean set at $\langle R \rangle = 100 \mu m$, and an increasing standard deviation.

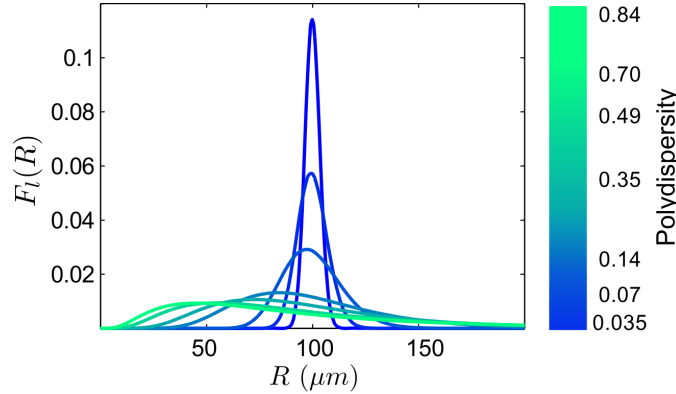


Figure 4.9: $F_l(R)$ functions used in the analysis. The mean of the distributions are kept constant at $100 \mu m$, while the standard deviation are varied from $3.5 \mu m$ to $84 \mu m$. The blue-green color scale represents the corresponding polydispersity, from the most peaked distribution ($P = 3.5\%$) to the most spreaded ($P = 84\%$).

For each foam, the over- or under-pressure felt by its bubbles can be computed as a function of the radius of the considered bubble, according to equations (4.43) and (4.42). These dissolution pressures ΔP_{foam} are plotted in figure 4.11, as colored hyperbolas following the same color scale as in figure 4.9. The armor collapse threshold value ΔP^* (Eq. 4.36) is then superimposed to the pressures imposed by the surrounding foam. The intersection of these curves defines a cutting radius R_{cut} (see figure 4.10), for each initial bubble distribution. Bubble whose radius is smaller that R_{cut} experience a dissolution pressure higher than their armor resistance, therefore they buckle and disappear, whereas if $R > R_{cut}$, the armored bubble is stabilized. It is observed that bubbles in a foam of high polydispersity globally experience a higher dissolution pressure. The cut-off radius is thus higher, and more armored bubbles are likely to buckle.

To gain a better view of the stability of the foam, we calculate the number fraction of collapsed bubbles in the foam (dissolved fraction) by summing the number of bubbles below R_{cut} . The model for foams with no particles at the interfaces predicts that over 50% of the bubbles will start to dissolve at the begining of the foam aging, even for very monodisperse initial distributions, as shown in figure 4.11. This is what is expected, since $R_{Lemlich}$ is close to the median radius in that case. Half of the bubbles are below the radius and dissolve.

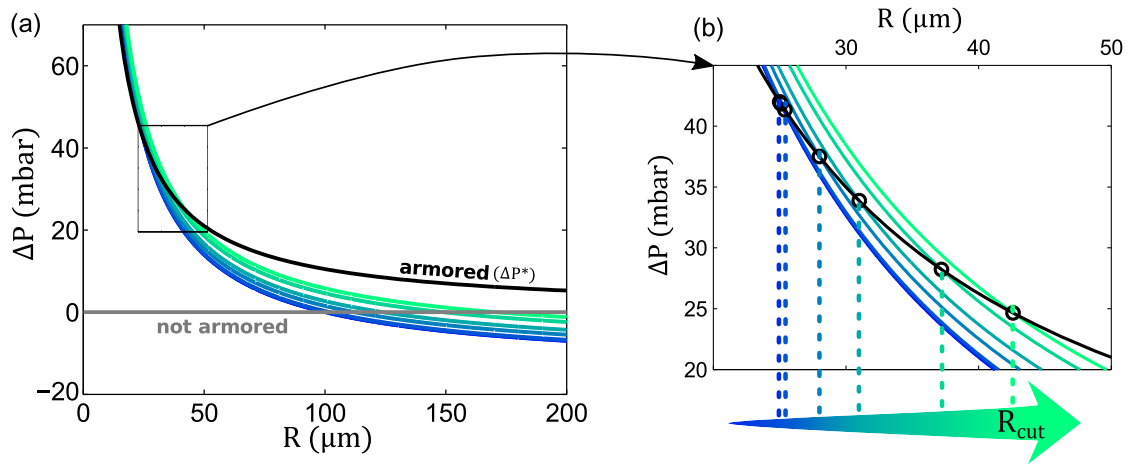


Figure 4.10: **(a)** The blue-green curves display the overpressure felt by a bubble as a function of its radius R in a foam with a log-normal bubble size distribution. The black line represents the resistance ΔP^* of a colloidal shell as defined from our model and our experiments. Bubbles subjected to a pressure below this critical value will collapse and disappear, while the others will remain stable. The case of unarmored bubbles ($\Delta P = 0$) is displayed in gray for comparison. **(b)** is a close-up of the region where $\Delta P = \Delta P^*$ (o), which defines the cut-off radii R_{cut} .

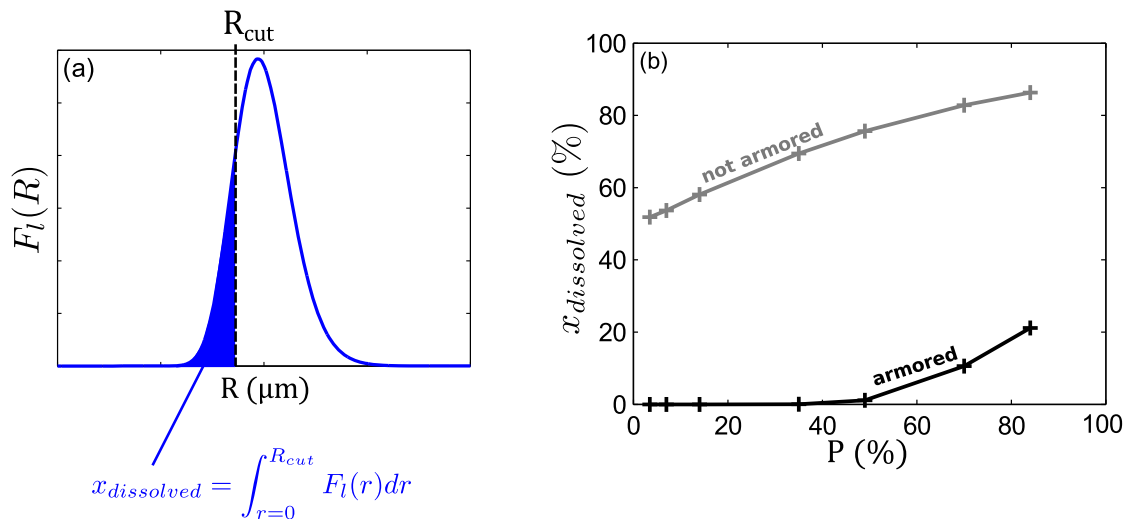


Figure 4.11: **(a)** The buckled percentage is calculated by integrating the probability density function on $[0, R_{cut}]$. **(b)** Proportion of bubbles that collapse/dissolve under the influence of the whole foam, in the armored case (black) and the unarmored case (gray), as a function of the initial polydispersity P of the initial distribution.

This is only true at the beginning of the evolution, since the distribution evolves as some bubbles swell or shrink. We are only interested in the initial stability of the foam: if the shrinking of the bubble below $R_{Lemlich}$ is prevented, so is the swelling of those above, since no gas is available for diffusion. This is what is expected to happen when the bubbles are armored: less than 0.1% of them are predicted to collapse for polydispersity up to 40%, indicating that these foams would be stable against Ostwald ripening from the very beginning of their evolution.

This study shows that our experiment and our model account for the stability of particle stabilized foams against Ostwald ripening. It also provides an easy way to extrapolate local properties at a single armored bubble scale, to the global stability of the foam against Ostwald ripening.

5

Outlooks

In this chapter, we put our theoretical and experimental results in perspective. First, the values of collapse pressures that we find experimentally and predict theoretically are compared with values found by other research groups. Although those studies were made using different configurations, we show that it is possible to compare their results with ours. Then, we discuss the possibilities opened both by the experimental microfluidic setup and by the theoretical framework. Finally, we conclude on the main advances provided by our work.

5.1 Connection to other studies

Despite numerous articles dealing with particle-laden interfaces, few papers address the question of the mechanical resistance of armored bubbles and droplets with quantitative measurements. We explore here the relations between the work presented in this thesis and the two most relevant studies.

Monteux et al. [16]

Monteux et al. investigate the deflation of a particle-coated millimetric droplet of decane in water. They observe jamming of the particles at the interface, and then a collapse of

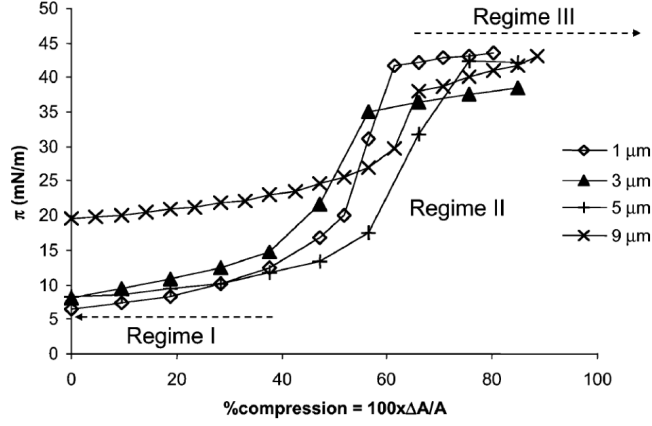


Figure 5.1: Surface pressure Π as a function of the compression ratio of the particle-laden interface in the Langmuir trough. Adapted from [16]

the subsequent colloidal shell as the volume of the droplet is further decreased. They identify three regimes I, II and III. I is the state in which the particles are not close-packed, before jamming. Regime II describes the rigid state of the shell, with jammed particles, where the volume of the droplet remains nearly constant. Regime III occurs when the armor buckles, which induces a sudden reduction of the volume of the droplet. Since those experiments are volume-controlled rather than pressure-controlled, they do not quantify the mechanical resistance of the armor.

However, they also perform surface pressure measurements on a flat interface in a Langmuir trough. They observe the same regimes I, II and III in this configuration. The surface pressure is low at first in regime I, then it increases with a constant slope in regime II, and it finally plateaus to an asymptotic value when regime III is reached (see figure 5.1). The value of the surface pressure at the transition II-III, i.e. the value of the plateau, can be related to the value of the buckling pressure that we measure for a spherical shell. The surface pressure Π can be seen as the compression force per unit length of shell. In the case of a spherical shell of radius R under compression, it is linked to the external overpressure ΔP by the geometric relationship:

$$\Pi = \frac{R\Delta P}{2}. \quad (5.1)$$

This expression is determined by considering an arbitrary equatorial rim on the sphere, which defines a cutting plane of the sphere. By projecting on the unit vector normal to this plane the pressure force F applied on the rim we have $F = 2\pi R\Pi = \pi R^2\Delta P$. The first thing to notice is that despite a 9-fold variation in the particle radius, the value of the plateau varies weakly, and stays between 37 and 43 mN/m. This shows that the

mechanical resistance of the particle covered interface is weakly influenced by the size of the beads, similarly to what we demonstrated in our experiment.

It is also possible to recover the numerical value of buckling surface pressure using our model (4.37) and the geometrical relation (5.1). Our expression $\Delta P \approx 1.57\gamma/R$ can be translated in term of surface pressure: $\Pi \approx 0.78\gamma = 0.78 \times 50.3 \text{ mN/m} = 39.5 \text{ mN/m}$, which is in agreement with Monteux et al.'s data.

Pitois et al. [44]

The experiments carried out by Pitois *et al.* consist in depressing a hemispherical droplet covered with solid particles. This time, the pressure is controlled, it is thus directly possible to relate their results to ours. They measured the collapse pressure of half air-in-water bubbles with radii from $240\mu\text{m}$ to 1 mm . The particle sizes tested are $16 \mu\text{m}$ and $40 \mu\text{m}$, and the surface tension is that of water, 70 mN/m . Their results are reported on figure 5.2, along with our measurements. The sizes of the bubbles tested are approximately one order of magnitude larger than the one from our work, but the values of $\Delta P_{collapse}$ they measure fall on the same line, which shows a very good agreement with our observations and theoretical model. Remarkably, the influence of the particle size is also very weak, even for particles as big as $40\mu\text{m}$, almost 9 times larger than the largest particles we used.

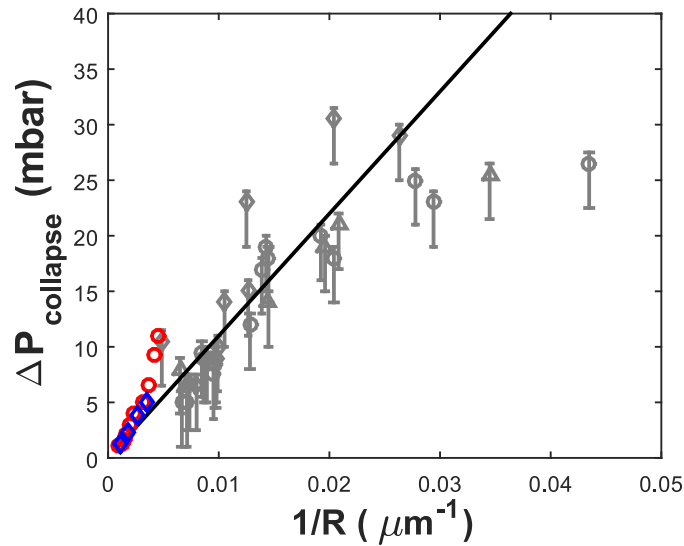


Figure 5.2: Collapse pressure of armored bubbles as a function of their inverse radius. Gray points are measurement form the present work, colored points are adapted from [44]. (red: $40 \mu\text{m}$ beads, blue: $16 \mu\text{m}$ beads.)

Our experimental measurements and model prediction are in very good agreement

with results from other authors with very different configuration. This shows the robustness of our experimental approach and the fiability of our theoretical description for a wide range of parameters, including particle size, bubble radius and surface tension.

Relevance to applications

This work investigates in details the behavior of particle coated bubbles, which are the elementary constituents of particle stabilized foams. The new insight gained into the comprehension of the mechanisms underlying the stability of these single objects can be extrapolated to draw conclusion on the stability of particle-laden foams against Ostwald ripening. Indeed, we combine our conclusions with the classic foam coarsening Lemlich model, and show that it explains the outstanding stability of particle stabilized foams, up to a large polydispersity of the initial foam.

This is of importance when it comes to engineer new particle-stabilized foams, because the acceptable level of initial polydispersity determines the choice of the process to generate the foam. The less stringent the condition on the monodispersity of the foam is, the cheaper it is to generate the foam using a simple and cost-effective process, such as whipping. Our model gives a quantitative upper bound on the polydispersity of the foam, given collapse pressures measured on single bubbles.

Another striking conclusion of our study is that the size of the particles has no influence on the mechanical resistance of the bubble, and therefore on the stability of the subsequent foam. One can thus use smaller particles and achieve the same stabilisation effect as with bigger ones, which presents two advantages. First, decreasing the size of stabilizing particles reduces the amount of material use, and consequently the cost. Second, it has been shown that smaller particles are easier to adsorb on interfaces than bigger ones [8]. The shear force required during foam generation and particle adsorbtion is thus also reduced, which requires a lower energy input and is less likely to deteriorate the properties of the raw materials during processing.

Both these informations are highly valuable in industrial area such as food industry and construction material (ie: concrete). Indeed, the margin on these product is in most cases very low, which is in part explained by the huge volumes of production. Therefore, while formulating these products, one can afford very little equipement or raw material cost increase. That is why stabilizing foam with small particles and using a low-cost foaming device is very advantageous. Lastly, and specifically to food product, another positive point of using smaller particle is their lower perceptibility in the mouth. Indeed, the generally admitted limit for a granular feeling when eating a preparation is a grain size of $30 \mu m$.

5.2 Perspectives

5.2.1 Explore more complex shells

The microfluidics system and the procedure developed here to probe an armored bubble is general and can be easily extended to more complex systems. Indeed, we have shown that the destabilisation of the armor is akin to that of an arch, with a short wavelength dislocation triggering the buckling. An interesting lead would be to use particles customized to inhibit these small scale deformation, in order to delay the onset of buckling. A first strategy would be to alter the geometry of the particle. We have seen that elongated particles do not induce any reinforcement of the shell, but recent studies [58, 59] show that angular shapes such as cylinder can induce an hinging effect that blocks the rotation of particles, which could possibly rigidify a shell made up of such particles. Other groups have manufactured cubical colloids [60], which could be even more effective. Rough particles or fractal aggregates such as fumed silica should also reinforce the shell by geometrically interlocking, and thus hinder the rolling and sliding of particles on each others.

A second strategy would be to chemically graft reactive groups or polymer brushes at the surface of the beads. A chemical reaction or the entanglement of the polymer between two adjacent particles could act as glue and sinter the shell, making it much more resistant. Using a sintering process reversible under a particular stimuli could even allow controlled collapse of the bubble under certain conditions. This would be useful for instance in situation where a foam is used for the decontamination of area polluted with hazardous chemical, biological or radioactive materials. Under its stable form, the foam is used for the actual decontamination thanks to its large contact area and volume, and is collapsed and liquified on demand to easily recover the hazardous substance.

Finally, it could also be interesting to investigate bubbles coated with living particles, ie: bacteria. We performed preliminary experiments, in collaboration with Gabriel Juarez (Environmental Microfluidics Group (MIT) Cambridge, MS). The objective was to adsorb bacteria from a strain of *Bacillus Subtilis* to the air-water interface of a bubble. Indeed, these bacteria are known to degrade hydrocarbon droplets by attaching at the water-oil interface [61]. This can be used for example to clean a sea oil-spill. The bacteria are thus 'hydrophobic', and we have shown that they can attach to an air-in-water bubble, as shown in figure 5.3. However, we did not observe buckling of these structures, probably because the bacteria were not enough strongly attached to the interface. Indeed, we observed rather desorption events, similarly to the case of particles with surfactant (see section 3.4). It would be useful to test other bacteria strains, that might be attached more strongly to interfaces, such as *Marinobacter aquaeolei*, another

oil degrading bacteria.

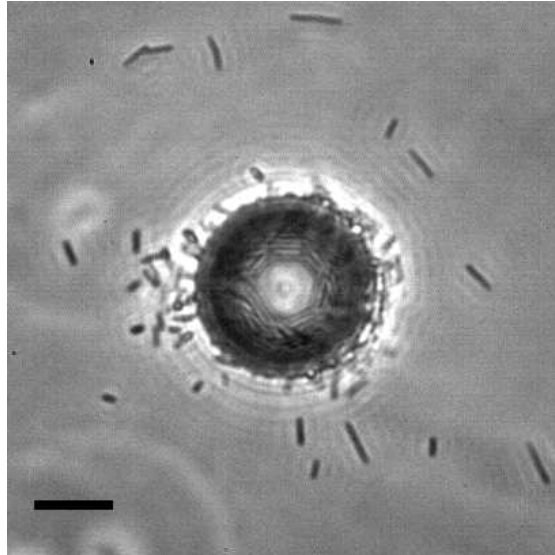


Figure 5.3: A bubble partially enclosed in a shell of adsorbed *Bacillus Subtilis*. Scale bar is $50 \mu m$.

5.2.2 Deepen the understanding of the coverage

The coating channel of the microfluidic device provides a reliable way of forcing the adsorption of particles on a bubble. This is interesting since the classical methods to adsorb particles in bulk involve a high shear rate in turbulent flow, that yields a low covering efficiency: most of the particles end up unused and stay in the bulk, rather than being adsorbed on the interface. While we understood the general mechanism of covering, in light of Zoueshitagh *et al.* study [41], it would be interesting to investigate in more detail the mechanism at play in the microchannel. In particular, what are the effects of dispersion flowrate and bubble speed, and which channel geometry is optimum to achieve the most efficient coverage. Also, it appeared that the aggregation state of the colloid had an influence on the coverage efficiency, a question that should also be investigated.

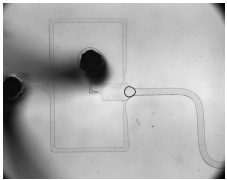
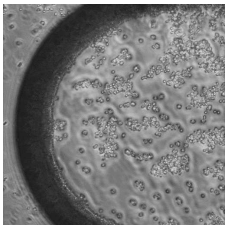
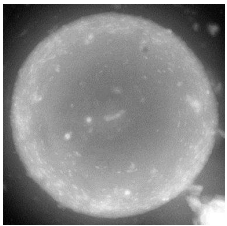
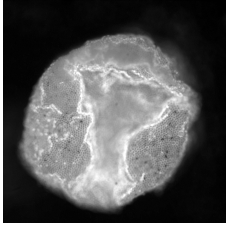
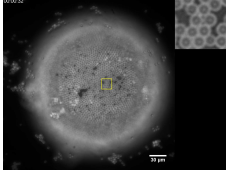
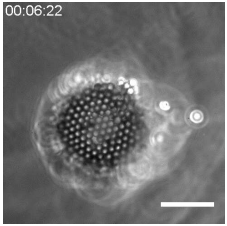
5.3 Conclusion

As microfluidic tools continue to develop and to gain in robustness, they provide novel methods to address questions in different areas of science. The study shown here, which relies on the ability to generate a single microscopic armored bubble and observe it over long periods, provides a unique approach for measuring the mechanical stability of these objects. Such measurements can naturally be generalized to a wide range of materials, including elastic shells or particles having different chemical, electrostatic, or mechanical interactions. When associated with the energy-based model presented above, new insight can be gained into the underlying physical interactions in these composite materials.

Our results on armored bubbles provide a multi-scale framework for understanding foam stabilisation: by submitting an individual armor to a controlled dissolution pressure, we observe a mechanical failure and quantitatively measure the resistance of the colloidal shell. We find a singular behavior that cannot be described by the usual elasticity argument invoked in many studies [15, 57, 25]. In particular, we show that small colloids have the same stabilisation capabilities as particles ten times bigger. These experimental observations are accounted for by a model that takes into account the microscopic structure of the shell, at the colloidal scale. We then combine those results to a classical foam evolution model and show that the stability criterion we found at the bubble scale can explain the outstanding stability of a particle stabilised foam.

This chapter focused on the behavior of the smallest elementary unit of a foam, ie. a bubble. In the next chapter, we take a step back and turn our attention to the destabilisation of an initially monodisperse wet foam.

Movies index

<p>Movie 1</p>		<p>Operation of the microfluidic device, first in bright-field to show the formation of the air bubble, then in epifluorescence, to show the covering of the bubble in the channel, its trapping and washing in the observation chamber.</p>
<p>Movie 2</p>		<p>Close-up of the bubble being covered in the coating channel. The particles stack at the rear of the bubble, forming the armor.</p>
<p>Movie 3</p>		<p>Evolution of the armored bubble as it is submitted to the pressure profile. The images of this timelapse are reconstructed from focus stacks, in epifluorescence illumination.</p>
<p>Movie 4</p>		<p>Buckling of different armored bubbles. (i) 4.5 μm particles in epifluorescence illumination. (ii) 4.5 μm particles in phase contrast. (iii) 0,5 μm particles in phase contrast.</p>
<p>Movie 5</p>		<p>Overlap of beads at the onset of buckling. The left image is an armored bubble compressed up to the onset of buckling, and the frame on the right is a simultaneous close-up on overlapping beads.</p>
<p>Movie 6</p>		<p>Armored bubble dissolving in a 100 ppm solution of SDS. Rather than buckling, the shell loses its particles one by one. They can be seen on the movie, advected by the outer flow.</p>

Part II

Emergence of disorder in a monodisperse foam

6

Monodisperse foam coarsening

In the last decade, there has been a regain of interest in foams with a very monodisperse bubbles size distribution [62]. Indeed, microfluidic and millifluidic techniques have recently rendered their production much easier and more reliable [33, 63]. The control over these monodisperse liquid foams is very valuable when they are used as precursor for solid foams. The material thus obtained exhibits a very ordered structure, which can confer it interesting mechanical or thermal properties. An example of application is that of the production of scaffolds for 3D cellular culture and tissue engineering [64], as shown in figure 6.1. An initially liquid monodisperse foam is gelified into the desired scaffold.

However, liquid foams age and their bubble size distribution evolve with time, mainly through three processes. The first one is coalescence when the liquid film between the bubbles ruptures. It can be avoided by the addition of a proper surfactant in the liquid phase. The second phenomenon is the drainage of the liquid between the bubbles under the influence of gravity. It can be slowed down by increasing the viscosity of the liquid phase, or even by using a yield stress fluid. The third foam coarsening process is Ostwald ripening, which is the diffusion of gas from small bubbles to larger ones. As we have shown in Part I, a very efficient way to block this process is to coat the bubbles with an armor of solid particles. A foam stabilized with particles can be stable and keep the

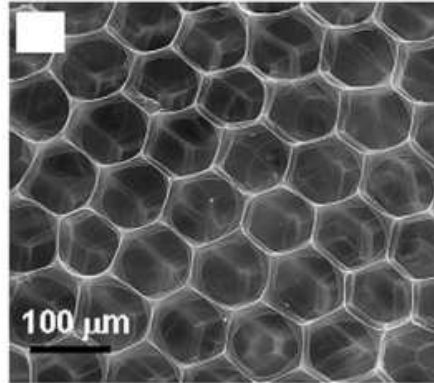


Figure 6.1: Scaffold produced by the gelification of a monodisperse foam of alginate solution. From [64]

same bubbles size distributions for months. Nevertheless, it is not always possible to protect the bubbles with colloidal shells, because the presence of solid particles may not be compatible with the final application of the product. This is why it is important to understand to what extent a monodisperse foam is stable in time and how it ages, when Ostwald ripening is not prevented.

Indeed, monodispersity is a very particular situation for a foam, in which all the bubbles have the same size. In such a situation, Ostwald ripening should theoretically not occur since there is no Laplace pressure difference between the bubbles. However, the situation cannot physically be this ideal, and the small, but inevitable, polydispersity of the foam triggers gas exchanges between the bubbles, which initiates the coarsening process. This leads the foam to a polydisperse self similar state [11, 65], in which the normalized bubble size distribution does not change, while the mean bubble radius increases. The ordered structure conferred by the monodispersity is thus lost once the final polydisperse state is reached. This final self-similar state is well known, both for the case of dry and wet foams. In the dry foam limit, it has been demonstrated that the self similar growth regime imposes a power law of exponent $3/2$ for the time variation of the mean bubble radius [66]. In the wet foam limit, which is equivalent to a bubbly liquid or an 'emulsion' of a gas in a liquid, the LSW (Lifshitz-Slyozov-Wagner) theory predicts an exponent $1/3$ for the evolution of the radius [10].

However, the transient regime between the monodisperse bubble size distribution and the self similar regime is not that well studied. It has been addressed by a few studies in two-dimensionnal cases [67, 68, 69]. It was found that the transient behavior depends on the initial degree of order of the foam, but the asymptotic steady state reached is always the same. In particular, Glazier *et al.* showed that, when the initial foam is highly monodisperse, the polydispersity overshoots before relaxing to the asymptotic

value. This is due to the presence of monodisperse domains that remain in the foam, even when the coarsening process has started, as shown in figure 6.2.

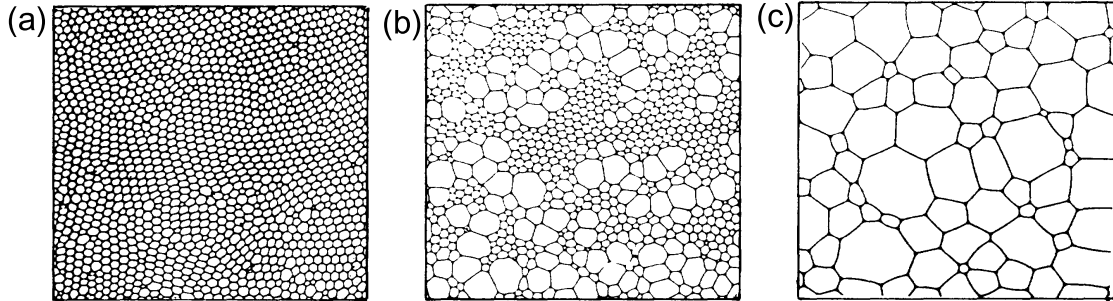


Figure 6.2: **(a)** Initial ordered state of the foam. **(b)** Transient state with polydisperse regions and regions retaining the initial monodispersity. **(c)** Final polydisperse, self-similar, state. From [67]

Although Glazier *et al.* described this transient regime, they did not investigate the spatial aspect of the transition: where and how the disorder appears and propagates in the foam? Indeed, their experiments suggest that the transition is all but homogeneous in space. This is important to know, for instance in applications where a liquid monodisperse foam is produced in order to solidify it and create a structured material. A badly scaled solidification time could give the final material a very heterogeneous structure, similar to that of figure 6.2. The properties, should it be mechanical, optical, or acoustical, of such a material would in consequence be deteriorated.

In this part, I will tackle this issue by considering the case of a quasi-2D wet foam, ie. a monolayer of spherical bubbles. The experimental setup we developed allow the individual monitoring of 30'000 bubbles constituting an initially monodisperse foam. First, we show that disordered zone randomly nucleate in the foam and spread. Then, we characterize the invasion speed of the disorder and account for the measurement by a model that takes into account the polydispersity of the disordered zones. Finally, we open on the possibilities of analysis offered by the setup and the data collection procedure.

7

Setup and experimental procedure

7.1 Microfluidic device

The microfluidic chip used for the experiments is shown in figure 7.1. It is composed of a large hexagonal observation chamber, of side 4 cm and thickness 0.8 mm, with two series of four sloped air injectors on two opposite sides of the hexagon. These injectors are similar to the ones used in the armored bubbles experiments, and serve to produce a large number of air bubbles. The only difference is the adjunction of small shunting channels at the end of the injector that ease the pinching of the air thread. These small channels allow fluid from the chamber to flow back to the low pressure region where the pinching occurs (see inset of figure 7.1), accelerating the detachment of the bubble. This injection method ensures a very narrow size distribution of the 30'000 bubbles studied [33]. Indeed, for a mean bubble radius of $120\mu m$, the measured standard deviation is typically less than $4\mu m$. The chamber is also connected to thicker channels to ease the filling and emptying of the foam between experiments. The filling process is shown in figure 7.2 and movie 7. The foam chamber is very slightly conical, with a slope toward the center of 0.1 %. This shape prevents the drift of the bubbles on one side or the other of the field of view, if the device is not perfectly horizontal.

A slab of transparent polycarbonate (PC) is embedded in the PDMS, above the

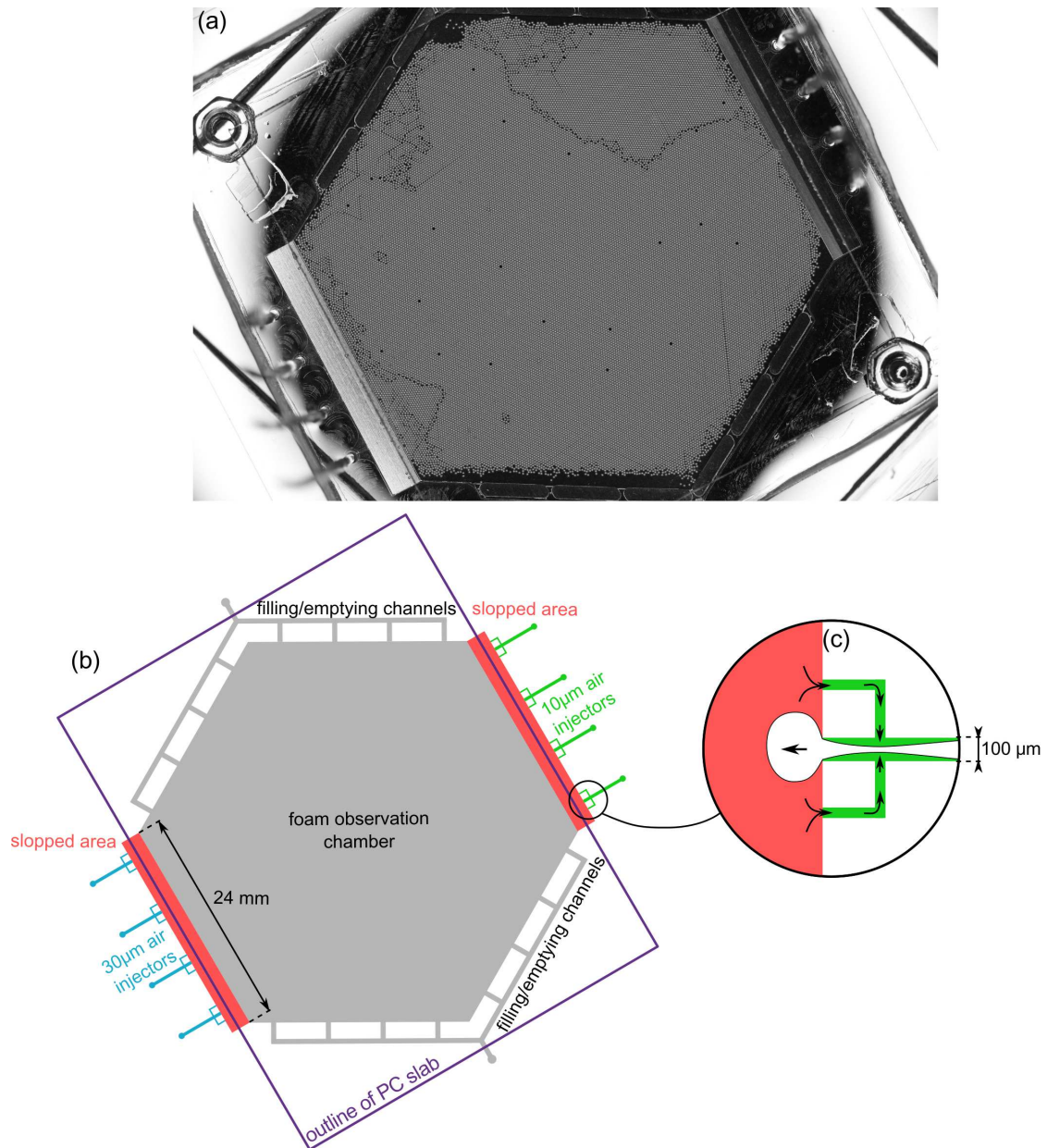


Figure 7.1: (a) Photography of the micro channel filled with foam. (b) Scheme of the geometry of the micro channel. The inset (c) shows the geometry of the shunting channels near the injectors. The arrows indicate the direction of the water flow that enhance the pinching of the air thread.

chamber, (see figure 7.3). Its dimensions are 48x44x3mm. Once PDMS has been cast on the brass mold, the PC slab is immersed in the liquid PDMS. The mold is then placed on a hot plate (150°C), and the PC slab is pressed against spacers that keep it 1 mm

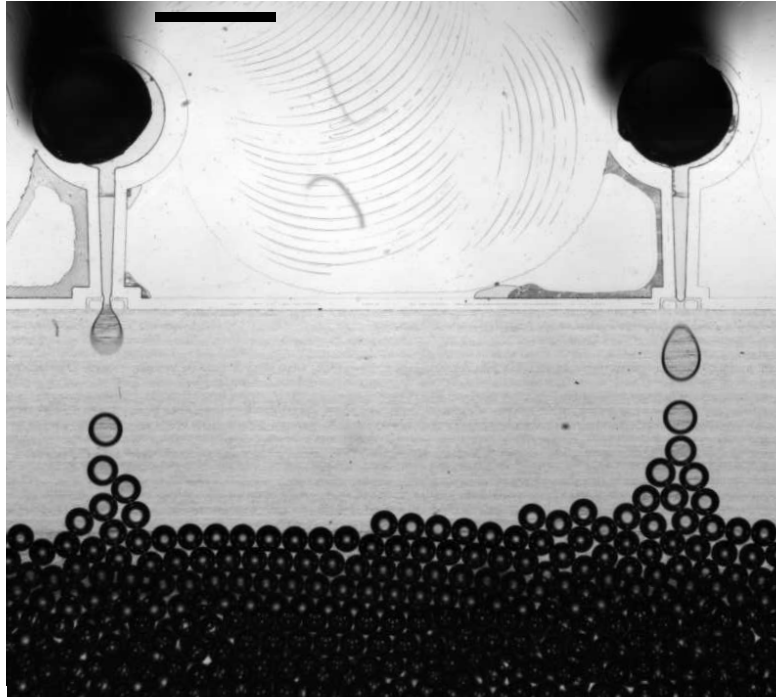


Figure 7.2: Generation of the bubbles in the sloped injector. After detachment, they travel toward the large chamber where they pack to form the foam. Scale bar is 1 mm.

above the top of the central chamber. It is necessary to press it until the PDMS has started to cure, to prevent it from rising by buoyancy.

This PC plate has two functions. Firstly, it reduces the elasticity of the large PDMS chamber, and thus reduces its hydrodynamic capacitance. Indeed, when the chamber is filled with bubbles, the pressure increase necessary to impose the flow of air and water swells the deformable chamber. When the flow is turned off, the chamber relaxes back to its original volume, creating a back flow that disrupts the bubble monolayer and forces bubbles outside of the chip. With a rigidified chamber, this phenomenon is greatly reduced. Secondly, the PDMS is permeable to gases, and at the very long time scales of the experiments we perform here (20h), this could have an influence on the gas-liquid equilibrium inside the chamber. Thus, the other utility of the PC slab is to create a gas-tight barrier that seals the chamber from the outer atmosphere.

7.2 Experimental procedure

In order to produce the foam, the device is first completely filled with a 2% w/w aqueous solution of SDS (Sodium Dodecyl Sulfate). This concentration is well above the CMC (10 times), which ensures a very good stabilisation of the bubbles. The only subsequent

coarsening mechanism is then inter-bubbles gas diffusion (Ostwald ripening), and coalescence events do not take place. Four independent outlets of a pressure controller (MFCS, Fluigent) are connected to the inlets of the wedged air injectors. The pressure is slowly increased until a regular production of bubbles starts at one injector. It is necessary to have more than one injector, since they are very thin (10 or 30 μm in height) and very likely to be clogged by small dusts or PDMS debris. However, the probability of four injectors being clogged during an experimental run is much lower. Depending on the pressure, the bubble production frequency is between 50 Hz and 100 Hz, so that the required time to produce the 30'000 bubbles necessary to fill the chamber is about 10 min. We consider that the bubbles do not evolve during the filling time, since the effective observation time of the experiment is more than 100 times longer.

The bubbles are then manually rearranged into a monolayer that floats atop the chamber. This rearrangement is necessary since bubbles may have stacked in multiple layers during their generation, as can be seen in the lower part of figure 7.2. To reorganize them into a monolayer, we gently press the top of the chamber to squeeze the bubbles against the floor of the channel. This results in the flattening of the bubble multilayer into a monolayer. The bubbles diameter is around 240 μm , so that, once they are arranged in the same plane, they are spherical and only in contact with the ceiling of the chamber.

The device is backlit with a ring-shaped light source placed 15 cm below the microfluidic chip, as shown in figure 7.3. An image of the chamber is captured every 90 s, through a 60 mm macro lens mounted on a Nikon D7000 digital single lens reflex camera (DSLR). The front lens of the objective is placed 5 cm above the microchip, so that the chamber fills the entire field of view. The resolution of the images captured is 4928x3264 pixels, which gives a definition, with our setup, of 27 μm /pixel. A time-lapse sequence is then acquired for a total duration of 20h.

7.3 Image analysis

The ring shape of the light enables an easy segmentation of the images to extract information about individual bubbles in the foam, as shown in figure 7.4. Firstly, the raw image is binarised using a threshold determined globally for the whole image sequence by hand. The image is similar to dark-field (ie. phase-contrast) micrograph: there is no direct light from the source hitting the sensor of the camera, only rays from the ring refracted by the interfaces of the bubbles. This yields a high contrast image (figure 7.4(a)) that can be easily thresholded: pixels above the threshold are set to a logical 1 value, pixels below are set to a logical 0 value. This yields a binary image, in which 1 pixels are

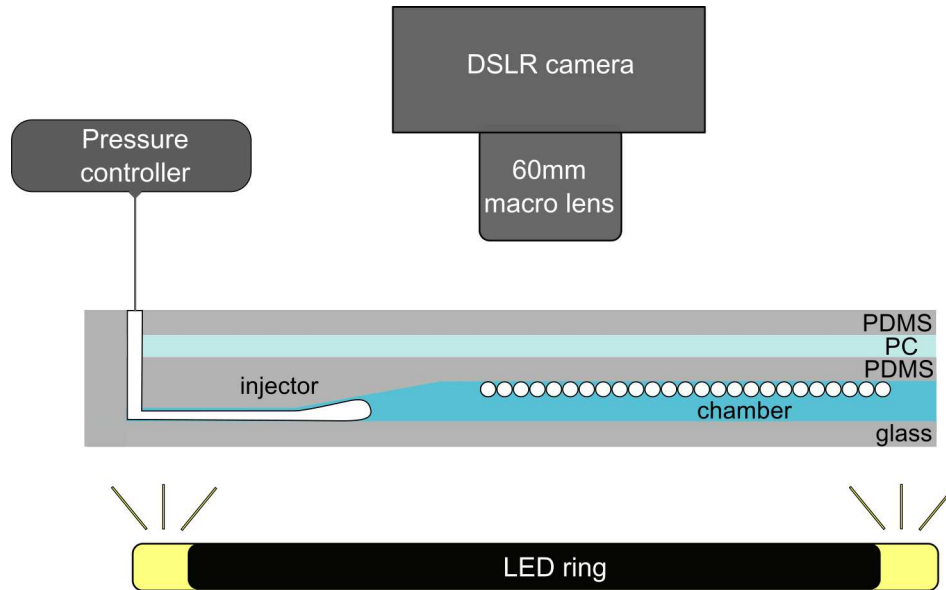


Figure 7.3: **(a)** Cross section of the air injector and bubble chamber. The air injected through the slope thanks to a pressure controller breaks into bubbles that pack at the top of the observation chamber, thus forming the foam. The device is backlit using a LED ring, and images are acquired from the top using a camera.

white and 0 pixels are black (figure 7.4(b)). This binary image is then cleaned by removing white regions smaller than 5 pixels or in contact with the border of the image. The white areas are then dilated by 1 pixel to close the rings that might present an opening, the holes (ie. black regions surrounded by white) are filled, and the resulting regions are eroded by one pixel to restore their original area. This enhanced binary image is shown in figure 7.4(c). Each white regions thus correspond to one bubble. By measuring the centroid position of the individual regions, and their area (ie. their number of pixels), it is possible to know the radius and position of each bubble. The measured centroids of the example image are shown in figure 7.4(d). This procedure is repeated for each image of the time-lapsed evolution of the foam.

The radius of the bubble is related to the area of the white region measured on the image. To find the relationship, we perform a calibration by hand on a few bubble of different sizes. For each bubble, its radius R is measured directly on the image. The apparent area of the bubble, ie. $A = \pi R^2$, is plotted against the area measured by the image analysis algorithm, A_I , as shown in figure 7.5.

A calibration by hand is performed on ≈ 10 bubbles to determine the coefficient of the linear relationship between the actual radius of the bubble and the radius of the light ring segmented by the procedure. In this way, the size of each bubble can be known with precision. The plot shows a linear relationship between the areas, with a

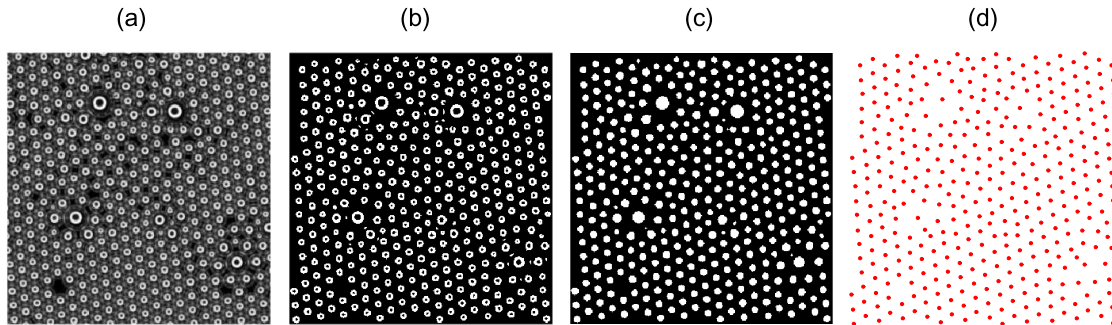


Figure 7.4: Process of image segmentation under Matlab. (a) Raw image. (b) Image after thresholding. (c) Binary image after cleaning and hole filling. (d) Resulting bubble centroid positions.

proportionality factor of 4.58. Since the definition of the image (in $\mu\text{m} / \text{pix}$) is known, we can calculate the actual radius of the bubble as a function of the area of the bright ring measured by the image analysis algorithm:

$$R \text{ (in } \mu\text{m)} = \sqrt{\frac{A_I}{\pi}} \times 4.58 \times 27 \mu\text{m} / \text{pix} = 16.25 \times \sqrt{A_I} \quad (7.1)$$

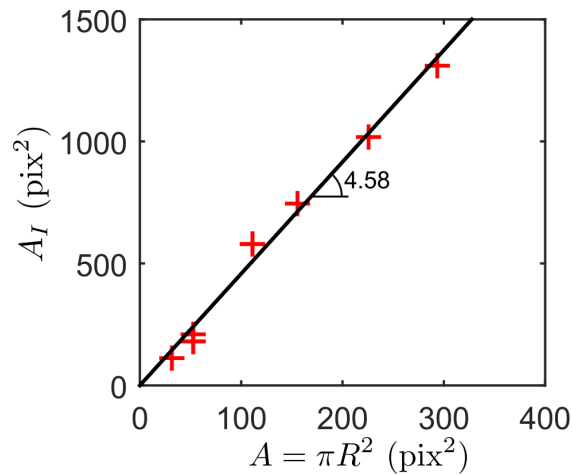


Figure 7.5: Area A_I measured by image analysis as a function of the actual apparent area measured for several bubble on he image (red crosses). The black line shows a linear regression, of slope 4.58.

8

Nucleation and growth of disorder

In this chapter, we study the evolution of a monolayer of spherical air bubbles in water. This system is a model system that is a surrogate for the evolution of a wet foam or an emulsion. The advantage of the monolayer configuration is that each bubble can be imaged individually, thus enabling precise measurements. This is an advantage over conventional methods that probe the evolution of the foam structure during ripening. For instance optical techniques (Diffuse Transmission Spectroscopy, Diffusing Wave Spectroscopy), are indirect measurements that only give access to averaged values of the bubble characteristics. More advanced methods such as X-ray tomography and Nuclear Magnetic Resonance Imaging can give access to the complete 3D structure of a foam, but they are much more heavy to implement.

The evolution of the foam is studied at different levels. First we show that the global evolution of the foam follows the classic expected scaling laws for emulsions [10]. Then we classify the bubbles into two population, and describe precisely the nucleation and growth of the spatial disorder in the foam.

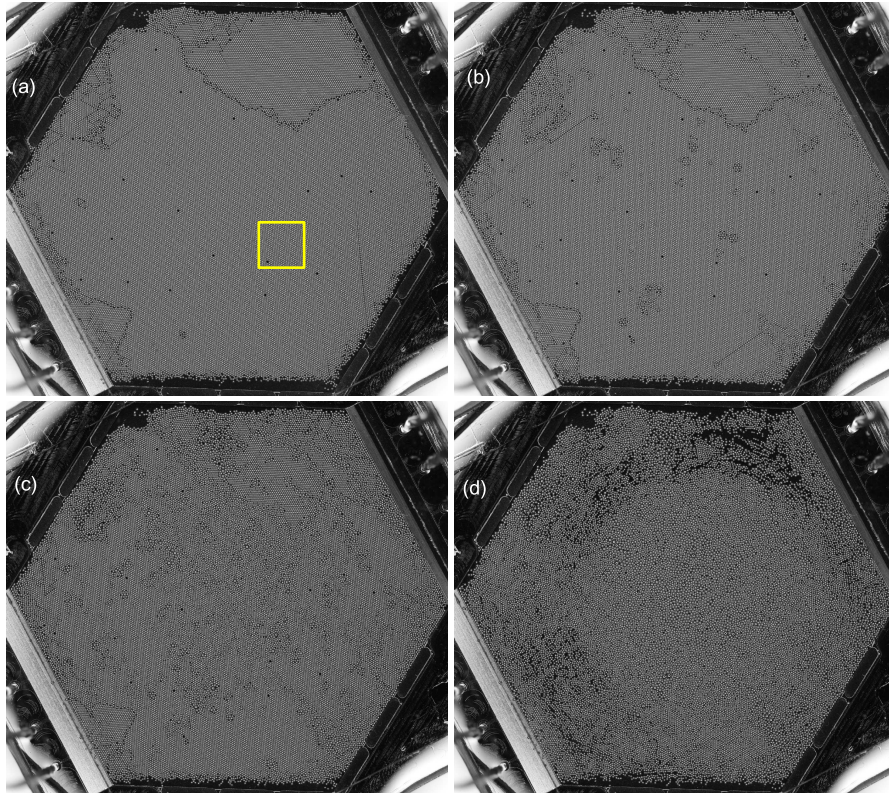


Figure 8.1: The foam at different steps of its evolution, in the microchip. The images were acquired using the lighting and camera setup described in section 7.2. (a) after 6 min. (b) after 126 min. (c) after 216 min. (d) after 296 min. The yellow in frame (a) represent the region magnified in figure 8.4.

8.1 Aging of a monodisperse foam

Figure 8.1(a) shows the whole system at the beginning of the evolution, a few minutes after the complete filling of the chamber. The foam exhibits a high crystalline order, the bubbles being packed according to an hexagonal lattice. Grain boundaries can be seen between regions where the principal directions of the bubble crystal are different. Some sites are also left inoccupied, creating vacancy defects in the crystal. The further evolution of the foam is shown in panels 8.1(b-d), and movie 8. The crystalline order observed at the beginning destabilizes between 60 min and 400 min and is completely lost afterward. When the foam has reached this fully disordered state it keeps evolving until the end of the experiment, but its general structure and organization does not change anymore.

This structure change can be quantified by monitoring the evolution of the polydispersity of the bubbles in time (see figure 8.2). The polydispersity of a set of bubbles is

defined as the ratio of the standard deviation to the mean of the bubbles radii:

$$\mathcal{P} = \frac{\sqrt{\langle (r - \langle r \rangle)^2 \rangle}}{\langle r \rangle} \quad (8.1)$$

where $\langle \rangle$ represents the mean over all bubbles in the foam.

The evolution of \mathcal{P} as a function of time is represented in figure 8.2. It shows a transition from a very monodisperse state ($\mathcal{P}=3\%$) to a state of steady polydispersity around 30%. This transition occurs between 100 min and 400 min, similarly to what was observed visually in the experimental images.

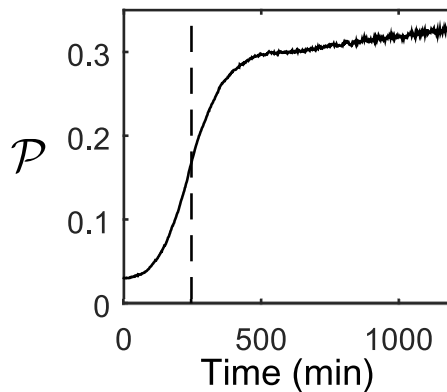


Figure 8.2: Evolution of the polydispersity of the foam. The vertical dashed line at 246 min represent the inflexion point of this curve. This line is reported in figure 8.3.

8.2 Long-time regime

The final state reached by the foam is a self-similar state [11] in which the structure of the foam remains steady, and the radii distribution scaled by the mean radius does not change. In particular, the radii standard deviation scaled by the mean radius, ie. the polydispersity \mathcal{P} does not change. Since our system consists of spherical bubbles, the classical LSW (Lifshitz-Slyozov-Wagner) theory [70] is well adapted to describe it. The LSW theory predicts the evolution of the droplet size distribution of an emulsion, undergoing Ostwald ripening. As in the case of a foam, the emulsion droplets exchange matter by diffusion across the continuous phase, due to the Laplace pressure difference between droplets of different sizes. The LSW theory predicts [10] that when self-similar state is reached, the mean bubble size $\langle R \rangle$ should evolve over time as $t^{1/3}$, while the total number of bubbles N should decrease as t^{-1} .

Figure 8.3 shows in log-log scale the evolution of N and $\langle R \rangle$ as a function of time. After ≈ 246 min, which corresponds to the inflexion point of the polydispersity curve,

these quantities follow power laws, of respective exponent -1 and $1/3$. This behaviour is consistent with the prediction of the LSW theory in the self similar regime. This shows that, after a transient regime, the monodisperse foam studied here tends toward a universal state, common to other types of foams or emulsion.

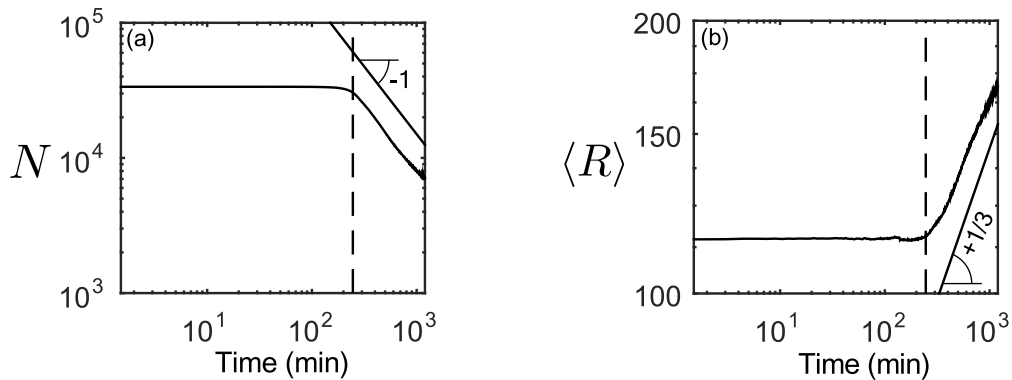


Figure 8.3: (a) Log-log scale plot of the total number of bubble in the foam. (b) Log-log scale plot of the mean bubble radius. The dashed lines mark the inflexion point of the polydispersity curve (see figure 8.2)

8.3 Order-disorder transition

We now focus on the transition from the initial monodisperse state toward the final polydisperse state.

Figure 8.4 shows close-ups of a particular region of the foam, highlighted in figure 8.1 by a yellow square. These snapshots are respectively taken at 6 min, 126 min, 216 min and 291 min.

At 6 min (8.4(a)), the foam is completely crystalline, arranged in a compact hexagonal packing where each bubble has 6 first neighbours. However, one vacancy defect can be seen in the lower left part of the frame. At 126 min (8.4(b)), three bubbles have started swelling by drawing gas from their 6 neighbours. The two upper bubbles show an earlier stage of destabilisation. Indeed, only the volume of their 6 first neighbours has been reduced, and the perturbation has not been propagated further in space than this first layer of bubble. On the contrary, the lower left bubble is at a more advanced stage, where the first layer is almost completely transferred in the central bubble. The bubbles in the second layer start to swell at their turn, since they are in contact with the very small bubbles of the first layer. In this way, the perturbation is propagated further in space, as shown in 8.4(c): at 216 min, other bubbles started to swell, creating new destabilisation points. Around the three first points, the first layer has completely disappeared and the

hexagonal symmetry has been broken. Finally, at 296 min (8.4(d)), the foam is completely destabilized and the crystalline order has been lost everywhere. The bubbles that started to swell at the beginning are still the largest bubbles in the foam.

It is interesting to note that the vacancy defect in the lower left corner does not seem to be the source of destabilisation of the foam. Indeed, the first step of ripening seen in 8.4(b) consists in random bubbles starting to swell and draw the gas from their closest neighbour bubbles. This sudden contrast in bubble size quickly propagates to further bubbles and the crystallinity is rapidly lost across the whole foam, as seen in figure 8.4(c-d).

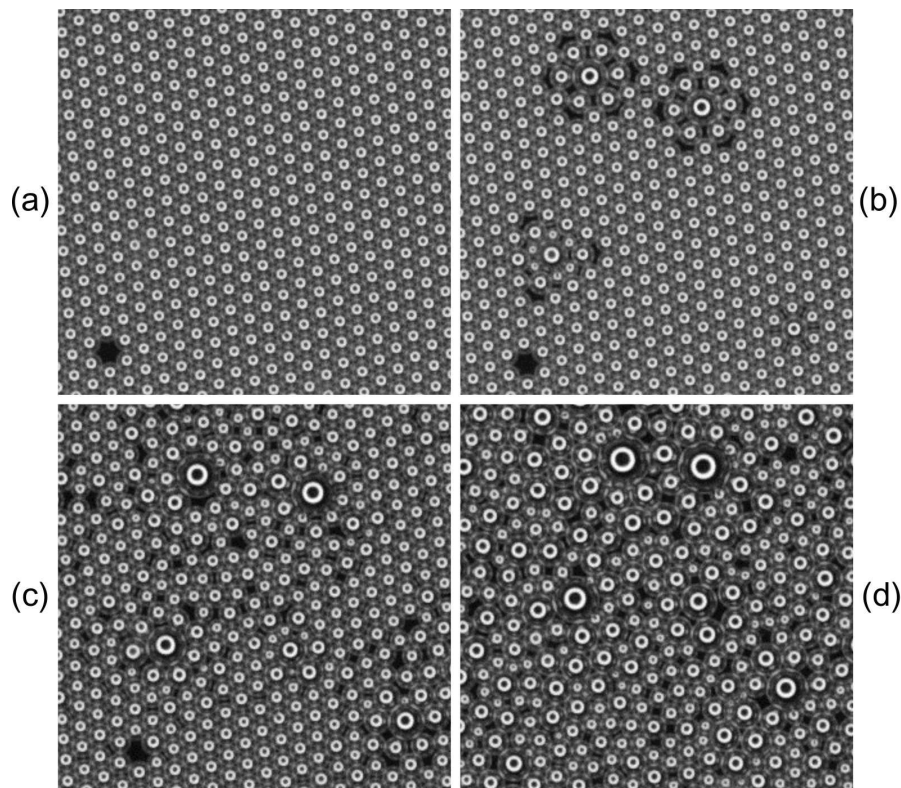


Figure 8.4: Close-ups of a region in the foam at different times. This region is shown by the yellow box in figure 8.1. (a) After 6 min. (b) After 126 min. (c) After 216 min. (d) After 296 min.

8.4 Classification in 2 sub-populations

As can be seen in figure 8.4 and movie 8, the foam is initially monodisperse and the bubbles are arranged in a crystalline fashion on an hexagonal lattice. During the first steps of its ripening, the foam seemingly segregates into two distinct populations. Some

bubbles remain ordered and the crystalline order is retained over large areas, while in other regions, they evolve more quickly as the order is lost and their radii change. These disordered regions grow around certain bubbles that are probably very slightly larger than their immediate neighbours at the beginning of the foam evolution, which triggers the destabilisation as described earlier (see figure 8.4). Here, we seek to define a criterion that classifies the bubbles as 'ordered' or 'disordered', in order to localize and quantify regions of disordered foam.

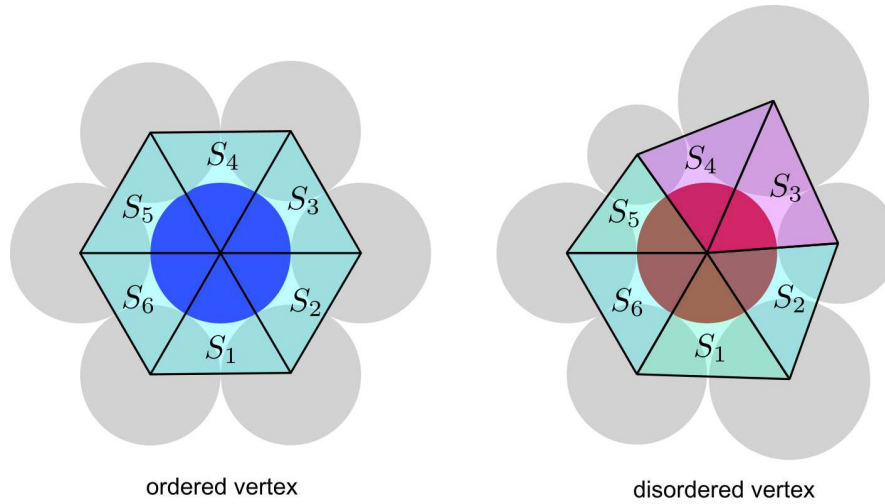


Figure 8.5: Sketch representing the principle of the calculation of the order parameter AD . The left side shows the case of an ordered vertex/bubble, with the six relative triangles having the same area, keeping the value of AD low. The right side corresponds to the case of 6-neighboured disordered vertex/bubble. Two of the associated triangles have areas that depart from the mean value, which raises the value of AD .

To do so, we start by computing the Delaunay triangulation of the positions of the centroids of the bubbles. Each vertex of the triangulation is thus connected to n triangles, n being the number of neighbours of the bubble. For each bubble/vertex, the areas S_i of its n associated Delaunay triangles are computed. The dispersion of the values of S_i is a good indicator of the regularity of the vertex arrangement [71]. The 'area-disorder' parameter AD_{bubble} quantifying this is calculated as:

$$AD_{bubble} = 1 - \left(1 + \frac{\sum_{i=1}^n (S_i - \langle S \rangle_{foam})^2}{n \langle S \rangle_{foam}} \right)^{-1}, \quad (8.2)$$

where $\langle S \rangle_{foam}$ is the mean triangle area over the whole foam. For a perfectly ordered bubble (fig.8.5(a)), the dispersion of S_i is low since all the triangles are similar. In that case, AD_{bubble} is close to 0. As the geometrical disorder increases (figure 8.5(b)), the triangles differentiate with each others, and AD_{bubble} increases, its maximum value

being 1.

A threshold value must be determined to separate sufficiently ordered bubbles from disordered ones. Furthermore, we add the additional criterion that an ordered bubble must have exactly 6 neighbours ($n = 6$). The threshold value is determined using Otsu's method [72] on the distribution of AD for each image. This method is widely used in image analysis, to find the best threshold for the segmentation of a gray levels image. Briefly, it considers the gray level value of all the pixels in an image, and find a separation threshold that minimizes the variance of gray value within each separated class. We apply this principle to the set of AD values computed in each image of the foam. Bubbles whose AD value is below the threshold and with $n = 6$ are classified as ordered, the rest is classified as disordered.

Figure 8.6 shows the Delaunay triangulation and the associated classification for the same image sequence as the one in figure 8.4. We can see that the intuitive notion of disorder in certain regions of the foam is well recovered by our classification method.

8.5 Characterisation of the bubbles subsets

Bubbles labeled as disordered, represented by a red star, form clusters inside a larger region of ordered bubbles (blue disks). As can be seen in figure 8.6 and movie 9, these disorder regions first randomly nucleate within the initial monodisperse foam and rapidly grow, until the foam is completely disordered. Figure 8.7(a) is a plot of the number of bubbles in each class (N_o ordered bubbles and N_d disordered ones) as a function of time. Since the total number of bubbles N decreases, it is more representative to plot the number fraction of each class, defined as:

$$x_{dis} \equiv x = \frac{N_d}{N_o + N_d} \quad (\text{disordered fraction}), \quad (8.3)$$

$$x_{ord} = \frac{N_o}{N_d + N_o} \quad (\text{ordered fraction}). \quad (8.4)$$

x_{dis} and x_{ord} are plotted in figure 8.7(b). The fraction of disordered bubbles is initially low and progressively increases while the number of bubbles in ordered regions decreases. At a well defined crossover time of 240 min, the x_{dis} exceeds 50%, and reaches a plateau to 96-97%. This residual value of $x_{ord} = 3-4\%$ is due to a flaw in the classification method. At the end of the transition, when the foam is entirely disordered, the distribution of AD is compressed toward its maximum value 1. But a tail of lower values still exists, and the Otsu's criterion then gives a threshold that let a small but finite number of bubbles be classified as ordered.

Figure 8.8 shows bubbles radii histograms of the two sub-populations. The top row

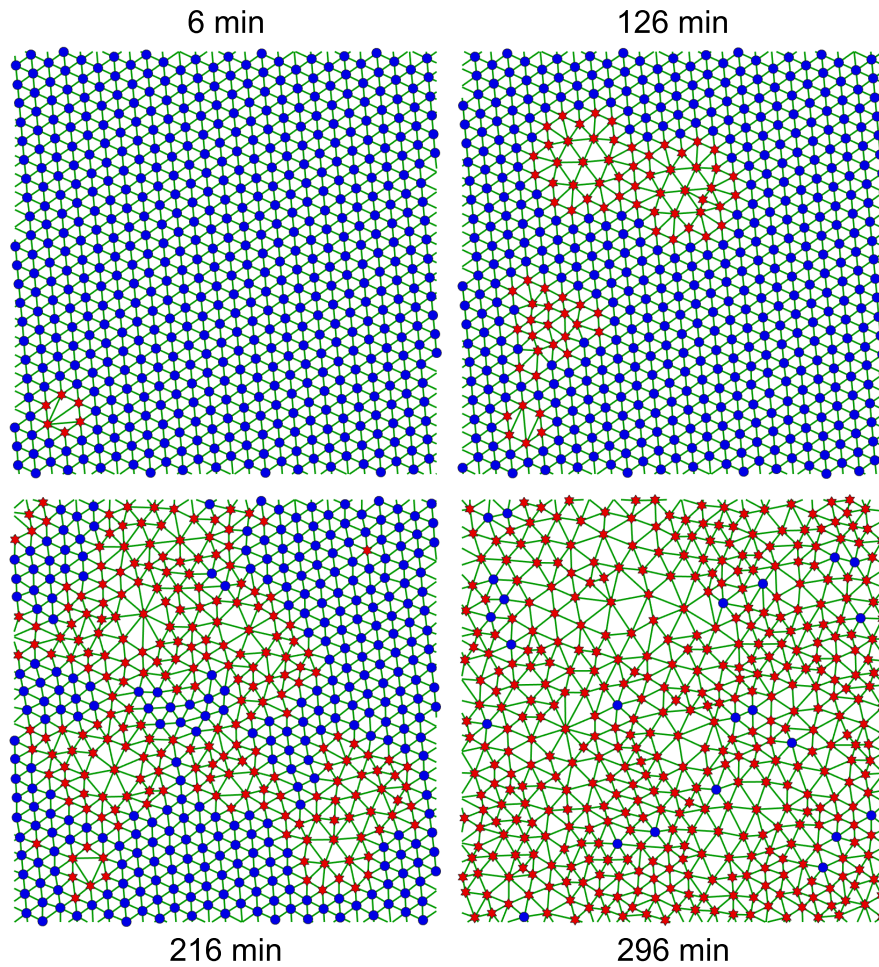


Figure 8.6: Delaunay triangulation of the foam region from figure 8.4, at different times. Ordered bubbles are represented by blue disks, disordered ones by red stars.

represents the raw number of bubbles in each size class, for the ordered (blue) and disordered (red) populations. Over time, the height of the blue histogram drops significantly, but with a width that remains constant. This shows that despite a rapid decrease of the number of ordered bubbles, their size distribution remains very monodisperse until their number falls to almost 0, around 400 min (see figure 8.7(a)). At the same time, the number of disordered bubbles rises, but the distribution is always wider than the ordered distribution.

The bottom row of figure 8.8 shows the same histograms normalized by the total number of bubbles in each population, which is thus a good representation of the probability density functions of the ordered and disordered bubbles radii. The blue histogram, stays relatively narrow and peaked until 150 min, but it starts to widen at 240 min, which corresponds to the inflexion point in figure 8.2. At this time, a large fraction of the foam

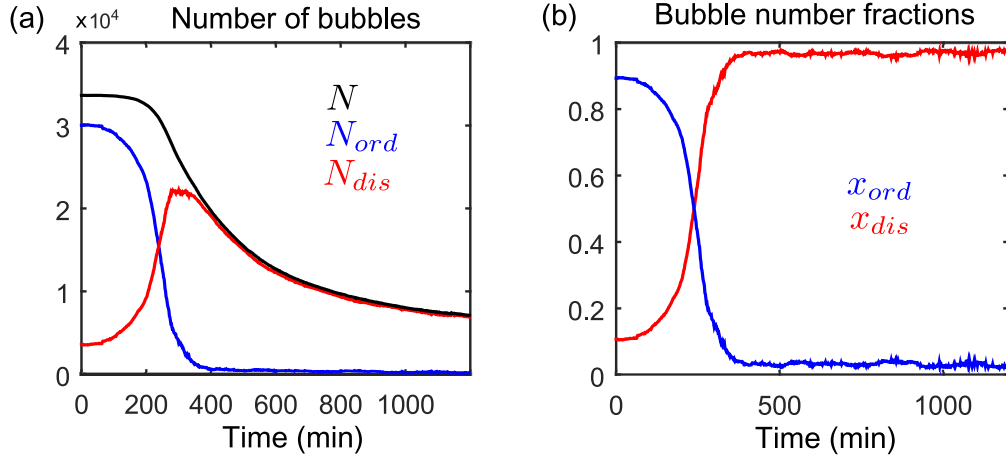


Figure 8.7: **(a)** Evolution of the number of bubble in ordered population (blue), disordered population (red) and total number of bubbles in the foam (black). **(b)** Normalized fractions of bubbles in each class.

is disordered, so that it becomes increasingly difficult to separate order from disorder. Some disordered bubbles may be classified as ordered, which widens the blue histogram. This tendency is confirmed by the last plot at 600 min: both histograms have the same shape because all the bubbles are disordered. The remaining ordered bubbles are classifications errors. The normalized distribution of disordered bubbles has a different evolution. It is peaked at the beginning, because even geometrically disordered bubbles have not had the time to evolve yet. However, their behavior rapidly departs from the ordered bubbles, as their distribution rapidly spreads from 150 min and becomes wider than the ordered bubbles distribution.

Finally, both histograms slightly drift toward the right, at higher radii values, in accordance with the regular increase of $\langle R \rangle$ observed (see figure 8.3). They also show no significant skewness, so that they can be approximated by gaussian distributions. This justifies the use of the mean and standard deviation as representative parameters to describes the bubbles size ditributions.

Indeed, these parameters are used to quantify the evolution of the distributions, as shown in figure 8.9. The mean radii of the two populations are equal and steady up to 200 min. After this time, the mean radius of the disordered bubbles starts to rise slowly, whereas that of the ordered bubbles remains steady up to 300 min before starting to rise more rapidly. This delay shows again the increased stability of the ordered bubbles in comparison with the disordered ones. The slope difference might be explained by the fact that at 300 min, most of the foam is disordered. The remaining ordered islands are small and surrounded by polydisperse foam which strongly destabilizes them. As for the standard deviations, their evolution are different. The deviation of the disordered

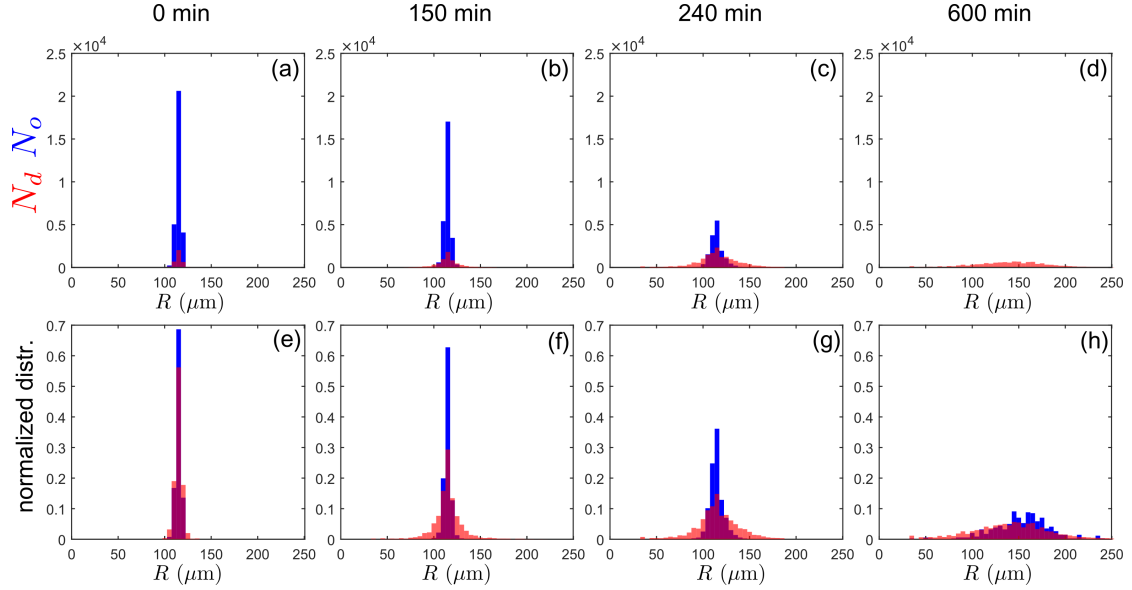


Figure 8.8: **(a-d)** Number of bubbles of different size classes in the ordered (blue) and disordered (red) populations, at different times of the foam evolution. **(e-h)** Normalized bubbles radii distribution in the two populations. The height of each bin from the first row (a-d) has been divided by the total number of bubbles in each population. The bin width of all the histograms is $5 \mu m$.

bubbles starts to increase from the beginning of the foam evolution, while that of the ordered bubbles keeps a constant low value for approximately 200 min, before starting to increase slowly. The values of the means and standard deviations are used to calculate the polydispersities \mathcal{P}_d and \mathcal{P}_o (resp. for the disordered and ordered populations) according to equation (8.1), as shown in figure 8.9(c). The polydispersity of the entire foam is also reported for comparison. This shows the very different behavior of the two populations: \mathcal{P}_d starts to grow earlier than the global polydispersity of the foam \mathcal{P} , whereas \mathcal{P}_o stays low for 150 min before starting to rise slowly at 200 min.

In all three plots of figure figure 8.9, the blue curves should not be considered after 400 min. Indeed, those points are measurements on residual ordered bubbles, which are not relevant because they are false-positives of Otsu's criterion.

The global evolution of the foam is thus explained by the combination of the evolutions of the sub-populations, the disordered bubbles being destabilized quickly and the ordered ones remaining relatively stable for a longer duration. \mathcal{P} is related to \mathcal{P}_o and \mathcal{P}_d through the formula

$$\mathcal{P}^2 = x\mathcal{P}_d^2 + (1-x)\mathcal{P}_o^2, \quad (8.5)$$

where $x \equiv x_{dis}$. Therefore, the variation of \mathcal{P} is due to two factors: (i) the rapid increase

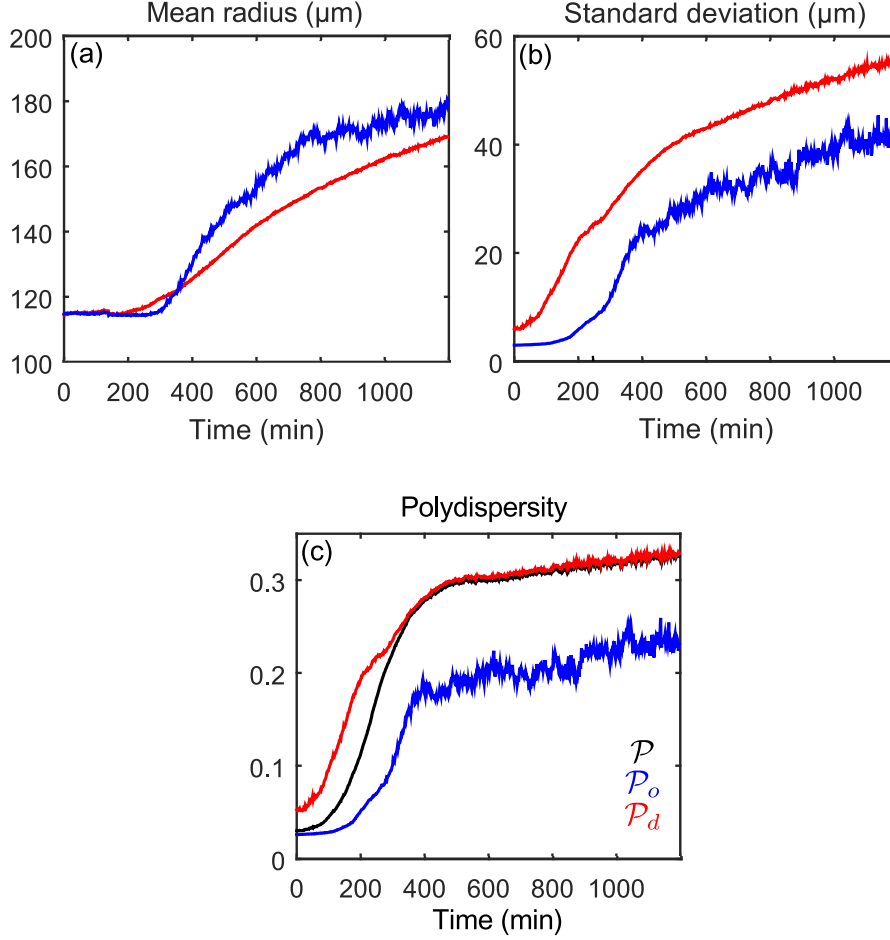


Figure 8.9: **(a)** Evolution of the mean bubble size for the ordered (blue) and disordered (red) populations. **(b)** Evolution of the standard deviation of the bubbles size distribution for the ordered (blue) and disordered (red) populations. **(c)** Evolution of the polydispersity of each population (red: disordered, blue: ordered, black: total) as a function of time.

of the polydispersity of the disordered bubbles, (ii) the increasing fraction of disordered bubbles within the global population. We quantify the contributions to the variation of \mathcal{P} by differentiating with respect to time the above expression (8.5):

$$\partial_t (\mathcal{P}^2) = \dot{\mathcal{P}}^2 = \underbrace{\dot{x}(\mathcal{P}_d^2 - \mathcal{P}_o^2)}_A + \underbrace{x\dot{\mathcal{P}}_d^2 + (1-x)\dot{\mathcal{P}}_o^2}_B. \quad (8.6)$$

Therefore, the variation of \mathcal{P}^2 includes two contributions A and B. A is a term that explains the variation of \mathcal{P}^2 due to the variation of the number of disordered bubbles \dot{x} , \mathcal{P}_d and \mathcal{P}_o being kept constant. Term B translates the contribution of the variations of the polydispersities of the two populations, for a given disorder fraction x . Figure

8.10 is a plot of experimental measurements of $\dot{\mathcal{P}}^2$ (solid line), and its two constituting terms A (dashed line) and B (dotted line) as a function of time. The principal peak in $\dot{\mathcal{P}}^2$ is composed of two subpeaks. The earlier one corresponds to the rapid expansion of the disordered zones (term A), while the second one is associated with the increase of polydispersity in the disordered zone (term B), that spreads on most of the foam at this time.

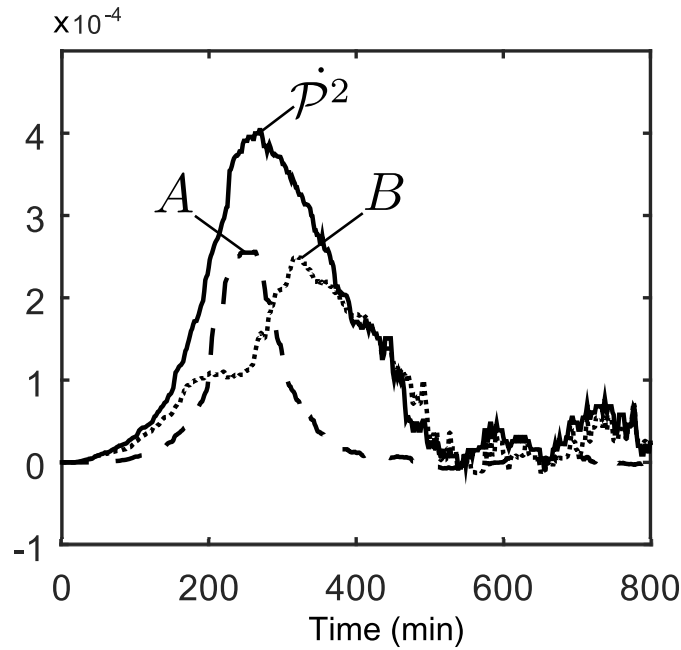


Figure 8.10: Plot of $\dot{\mathcal{P}}^2$ (solid line). The dashed line is the term A, corresponding to the contribution of \dot{x} . The dotted line is the term B, corresponding to the contributions of $\dot{\mathcal{P}}_o$ and $\dot{\mathcal{P}}_d$.

This shows that the destabilisation of the foam is composed of two successive mechanisms, (i) the nucleation and growth of disordered zones and (ii) the destabilisation of the now completely disordered foam until self similar regime is established. The first instants of the monodisperse foam destabilisation are thus not homogeneous in space, and if the foam was to be solidified or gelified at those times, it would have heterogeneous structural properties. This allows to choose the moment at which to 'freeze' the foam, before the transition to retain the crystalline structure, or after the transition to guarantee a homogeneous spatial structure that is disordered everywhere, and not only in certain regions.

The first part of the transition is thus the one that has the biggest impact on the structure of the foam. It is responsible for the loss of crystallinity in the bubbles' spatial arrangement, which can profoundly alter the properties of the foam. In the next section,

we analyse in details the growth rate of the disordered zones, and relate it to global properties of the foam.

8.6 Model of the disorder invasion

8.6.1 Constant invasion rate

Glazier et al. [67] described the ripening of a monodisperse foam as the growth of disorder region inside a monodisperse 'fossile' foam. However, they did not have access to an actual experimental measurement of the disorder fraction x that they use in their modeling. Therefore, we attempt to use Glazier's model to describe the evolution of x observed in our experiments.

The authors assume that the growth rate of the number of disordered bubbles N_d is proportionnal to the contact length between ordered and disordered zones. This contact perimeter is estimated, under the assumption that the disordred zones are randomly scattered in the foam, which yields an approximate expression of the contact perimeter L :

$$L \propto \frac{N_o N_d}{N_o + N_d}. \quad (8.7)$$

Since Glazier *et al.* do not justify this expression, we give here a simplified model to explain the origin of the scaling for the perimeter. For this, the foam is modeled as a square lattice comprising $N = N_o + N_d$ sites, as shown in figure 8.11. A site can either be occupied by an ordered bubble (blue), with a probability $p(o) = N_o/N = 1 - x$, or a disordered one (red), with a probability $p(d) = N_d/N = x$. To calculate the contact perimeter, let us consider an arbitrary couple of sites, as depicted in figure 8.11(b). The probabilities of the 4 different configurations are:

$$p(dd) = x^2 \quad (8.8)$$

$$p(oo) = (1 - x)^2 \quad (8.9)$$

$$p(do) = x(1 - x) \quad (8.10)$$

$$p(od) = (1 - x)x. \quad (8.11)$$

The length of the perimeter is given by the total number of site doublets, multiplied by the probability of having an order-disorder interface on the doublet:

$$L = \frac{N}{2} \times 2x(1 - x) = \frac{N_o N_d}{N_o + N_d} \quad (8.12)$$

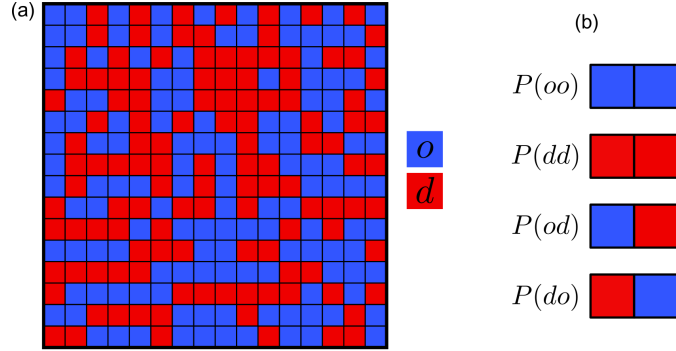


Figure 8.11: **(a)** Sketch of the square lattice used to calculate L . Ordered bubbles are represented by blue squares, disordered bubbles by red ones. **(b)** Four possible configurations of the couple of sites.

This justifies the form of Glazier's differential equation:

$$\dot{N}_d = \tau_G^{-1} \frac{N_o N_d}{N_o + N_d}, \quad (8.13)$$

where τ_G is a characteristic time, used as a fitting parameter. By dividing the two members by $N = N_o + N_d$, it simplifies into

$$\dot{x} = \frac{x(1-x)}{\tau_G}. \quad (8.14)$$

This differential equation can be solved and we get

$$x(t) = \frac{1}{1 - (1 - \frac{1}{x_0}) \exp -\frac{t}{\tau_G}}, \quad (8.15)$$

where $x_o = x(t = 0)$. The measurements and the best fit of this expression are represented in 8.12. The best fit parameter is $\tau_G = 98$ min, which corresponds to an inflexion point at 215 min. It can be seen that the transition predicted by the model is not sharp enough to accurately describe the measurements.

8.6.2 Variable invasion rate

We propose a new model to describe the invasion of the crystalline foam region by the disordered zones. More specifically, we refine the expression of the constant transfer rate $1/\tau_G$ used by Glazier *et al.* [67]. The idea is to account for the fact that as the polydispersity \mathcal{P}_d in the disordered zone rises, the rate at which it invades the ordered regions increases as well. Indeed, this idea is supported by the Lemlich model on foam evolution [53], that we already used in Part I: more polydisperse foams impose higher

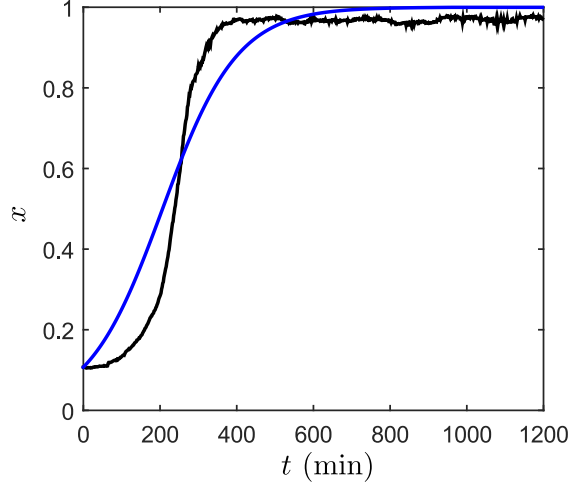


Figure 8.12: Evolution of the disordered bubble number fraction x as a function of time. The black line is the experimental data, blue line is the best fit using Glazier's model [67], with $\tau_G = 98$ min.

dissolution pressures to the bubbles within. The idea of our model is to estimate the speed of progression of the order-disorder boundary. More precisely, we discretize the problem, since we calculate the time necessary for the boundary to jump of one bubble length, or in other words for one layer of ordered bubbles to become disordered

The motion of the boundary between the zones is modeled as depicted in figure 8.13. Once a bubble B_0 is in contact with the boundary, it takes a time t_J until it switches from ordered to disordered. t_J is the typical time the boundary takes to 'jump' one layer of ordered bubbles. If we fix an arbitrary disruption α that the bubble B_0 must undergo to switch from ordered to disordered, we can write

$$R_0(t + t_J) = R_0(t) + t_J \dot{R}_0(t) \quad (8.16)$$

$$= R_0(t) + \alpha R_0(t) \quad (8.17)$$

$$\Rightarrow t_J(t) = \alpha \frac{R_0(t)}{\dot{R}_0(t)} \quad (8.18)$$

The invasion rate \mathfrak{K} is defined as the inverse of the time necessary to change the classification of one layer of bubbles. This yields the following scaling of the invasion rate \mathfrak{K} :

$$\mathfrak{K} \propto t_J^{-1} \propto \frac{\dot{R}_0}{R_0} \quad (8.19)$$

Indeed, the faster the bubbles radius changes, the faster their geometrical arrangement is disturbed, and the faster they will switch from an ordered to a disordered classification.

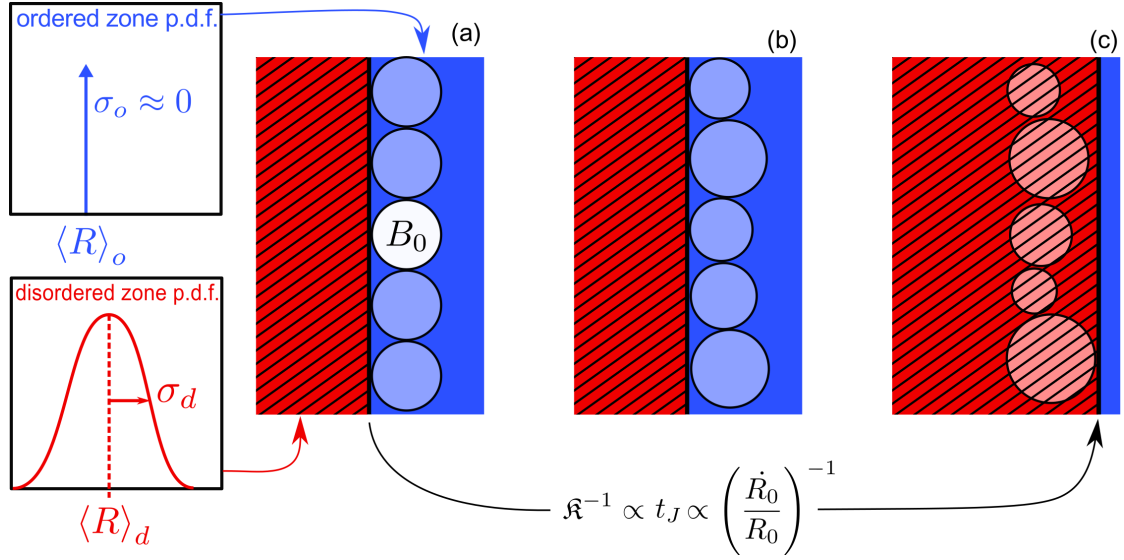


Figure 8.13: Sketch of the model system describing disorder invasion. **(a)** The ordered (blue) region is perfectly monodisperse, while the disordered region (red) is a random bubble population with a known probability density function (p.d.f.). **(b)** As the system evolve, the first layer of blue bubbles destabilizes under the influence of the red region, up to a point **(c)** where the first layer is sufficiently disorganized to be classified as disordered. At this time, the boundary jumps and the process restarts.

For the sake of simplicity, we consider that the ordered region of the foam is strictly monodisperse, so that the probability density function (p.d.f.) of the ordered bubbles size distribution is a δ function, centered in $\langle R \rangle_o$. On the other side of the boundary, the foam is modeled as a random medium, composed of disordered bubbles whose size are distributed according to a p.d.f. centered in $\langle R \rangle_d$, with a standard deviation of σ_d (see figure 8.13(a))

The Lemlich model relies on a mean-field approximation to estimate the radius time derivative of a particular bubble, surrounded by a population of bubbles of random sizes. Using the same approach, we focus on the particular bubble B_0 in the ordered first layer. This bubble, of radius $R_0 = \langle R \rangle_o$ is submitted to the disordered environment on the other side of the boundary, which is responsible for its radius variation. Indeed, the other bubbles on the ordered side have no effect on B_0 since they all have exactly the same radius $\langle R \rangle_o$. Thus, there is no pressure difference and no gas transfer with these bubbles. Therefore, the random foam on the disordered side is the only responsible for the evolution of B_0 . According to Lemlich formula, its rate of radius variation is:

$$\dot{R}_0 = \kappa \left(\frac{1}{R_d^{21}} - \frac{1}{R_0} \right). \quad (8.20)$$

κ is a parameter incorporating the physico-chemical properties of the foam. Its expression is $\kappa = 2JR_g\gamma T/P$, with J the gas-permeability of the interfaces, R_g the perfect gas constant, P the ambient pressure. R_d^{21} is the so-called 'Lemlich radius', already discussed in Part I. It is the ratio of the second raw moment to the first raw moment of the bubble size distribution. Since here we consider only the distribution of disordered bubbles, its expression becomes:

$$R_d^{21} = \frac{\langle R \rangle_d^2 + \sigma_d^2}{\langle R \rangle_d} \quad (8.21)$$

$$= \langle R \rangle_d (1 + \mathcal{P}_d^2). \quad (8.22)$$

Indeed, by definition of the polydispersity, $\mathcal{P}_d = \sigma_d / \langle R \rangle_d$. We can now estimate the rate of invasion \mathfrak{K} from equations (8.20) and (8.22). The sign of the radius variation is not important since the disorder can arise either from shrinkage or swelling of the bubble. Hence, we take the absolute value of \dot{R}_0 :

$$\mathfrak{K} \propto \left| \frac{\dot{R}_0}{R_0} \right| = \frac{\kappa}{R_0} \left| \frac{1}{\langle R \rangle_d (1 + \mathcal{P}_d^2)} - \frac{1}{R_0} \right| \quad (8.23)$$

Finally, we assume that the average bubble radius is the same in the ordered and disordered populations, ie. $R_0 = \langle R \rangle_o = \langle R \rangle_d$. The expression of \mathfrak{K} then becomes:

$$\mathfrak{K} \propto \frac{\kappa}{R_0^2} \left(\frac{\mathcal{P}_d^2}{1 + \mathcal{P}_d^2} \right) \approx \frac{\mathcal{P}_d^2}{\tau} \quad (\mathcal{P}_d \ll 1), \quad (8.24)$$

where $\tau = R_0^2/\kappa$ will be taken as a fitting parameter. It incorporates the mean ordered bubbles radius R_0 , and the physico-chemical properties of the foam κ .

The differential equation for the evolution of the disorder fraction x becomes, with this new expression of the invasion rate,

$$\dot{x} = \frac{\mathcal{P}_d^2}{\tau} x(1-x). \quad (8.25)$$

This equation can be integrated by separation of variables:

$$x(t) = \left[1 - \left(1 - \frac{1}{x_0} \right) \exp \left(-\frac{1}{\tau} \int_0^t \mathcal{P}_d(y)^2 dy \right) \right]^{-1}, \quad (8.26)$$

where y is a dummy integration variable.

This expression is fitted to the experimental measurement of $x(t)$, with τ the adjust-

ment parameter. The experimental values of \mathcal{P}_d are used as measured in the experiments, without further processing. As shown in figure 8.14, the agreement with the data is very good. The optimal value of the fitting parameter is $\tau = 1.95$ min.

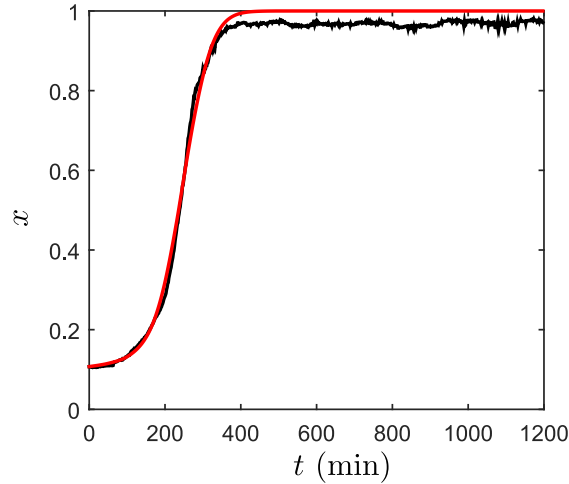


Figure 8.14: Evolution of the disordered bubble number fraction as a function of time. Solid line is the experimental data, dotted line is the model used by Glazier in [67], and dashed line is our modified model.

With this modeling, the sharpness of the transition is recovered, which shows that \mathcal{P}_d^2 is a good descriptor of the invasion rate of the disordered foam.

The validity of the hypothesis on which this model relies can be tested experimentally. First, it can be seen on figure 8.9 that the hypothesis $\langle R \rangle_o = \langle R \rangle_d$ is very well verified up to 200 min. After this time, the two curves separate until 400 min, which is the time when the invasion is completed and the foam is completely disordered. However, the difference never exceeds $10 \mu m$, a relative variation of 9 %, which is reasonable.

Second, the characteristic time τ should be proportionnal to R_0^2 . Intuitively, this signifies that a foam composed of larger bubbles should evolve and destabilize more slowly, which is reasonable, since the pressure in larger bubbles is lower, inducing slower gas transfers. This could be confirmed experimentally by monitoring a foam with larger bubbles, but unfortunately the present setup did not give us access to values of R_0 significantly different enough to draw clear conclusions.

Finally, the contact perimeter L between the ordered and disorder zones is assumed to scale like $x(1-x)$. It is possible to experimentally measure this perimeter. To do so, we count the number of ordered bubbles that count at least one disordered bubble in their neighbours (according to the Delaunay triangulation). This number N_p is measured at each time of the bubble evolution. The temporal evolution of N_p , as well as that of $x(1-x)$ are plotted in figure 8.15. The curves are very similar, and the correlation is

shown in the last panel of the same figure, where N_p is plotted versus $x(1-x)$. The points align on a straight line, which experimentally confirms the validity of the scaling law for the perimeter.

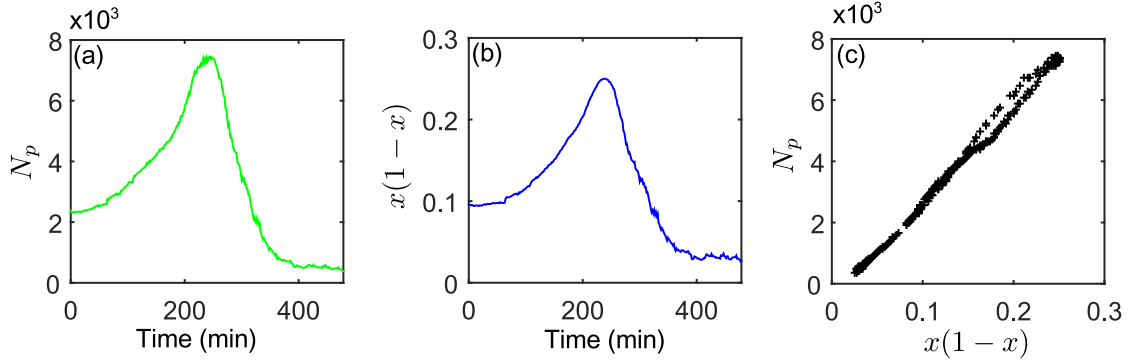


Figure 8.15: **(a)** Time evolution of the experimentally measured perimeter, ie. the number of bubble in the perimeter, N_p **(b)** Time evolution of the computed value of $x(1-x)$. **(c)** N_p plotted against $x(1-x)$.

8.7 Conclusion

In part II, we have presented a microfluidic setup with which the ripening of a monodisperse foam could be monitored precisely, at the level of individual bubbles. We have shown that the destabilization from the initial ordered state to the final self-similar state is a two steps process. Firstly, disordered zones randomly nucleate in the foam and invade the other regions that stay more ordered. The polydispersity of the disordered zones is higher and increases more rapidly than that of the the ordered regions. Secondly, after the spreading of the disorder over the whole foam, the polydispersity homogeneously rises until it reaches the plateau value, characteristic of the final self-similar state. The first step of the transient regime is thus spatially inhomogeneous, since polydisperse zones, lacking any structural order, coexist with very monodisperse areas, exhibiting a crystalline order.

This invasion step has then been analyzed in details, to understand the mechanisms explaining the propagation of the disorder in the foam. We have shown that the rate of growth of a disordered zone is proportionnal to its perimeter, and that the rate of invasion per unit length of perimeter depends on the polydispersity of the disordered zone. Precisely, this rate \mathfrak{K} scales like \mathcal{P}_d^2 .

This shows that the transient regime between a monodisperse state and the well known self-similar regime is complex, and has a great impact on the structure of the

foam. Not only the foam loses its crystalline order, but it also does so in a heterogeneous manner: disorder zones randomly nucleate and grow, while large region can remain crystalline for a long time. This mechanism, that we precisely reproduced with a model, was observed on quasi-2D systems. However, since the bubbles are spherical, the exchanges between the bubbles would be same in a wet 3D foam, or even an emulsion. The destabilisation process would very certainly be similar to what we observed, and could be described with our model, although the geometry of the disorder invasion would be more complex.

The accurate knowledge of the destabilization process is very relevant when one wants to produce a porous material by solidifying a liquid foam, for instance, concrete, ceramic, metal or ice-cream. The bubble size distribution of the foam sets the final structure of the material, that is why it is paramount to know how it evolves over time after the generation of the bubbles in the initial liquid.

Finally, the general idea of the destabilization process described here could be generalized to other systems involving individual identical elements interacting with each others, such as living cells in a tissue, droplets in an emulsion, or microcrystals in a metallic alloy.

In any case, the general philosophy of the phenomenon is very well summed up by the famous belgian comic character 'Le chat', in figure 8.16.



Figure 8.16: Translation of the text in the bubbles: 'If one puts a little bit of disorder in a perfect order, it is immediately a mess. However, if one puts a little bit of order in the middle of a mess, it is still a mess. It means that the mess is stronger.' From [73]

9

Future work

The experiments described in the previous chapter are very rich and yield a substantial amount of data. We present here a few interesting leads for future research based on preliminary work that we carried out.

9.1 Single bubble tracking

Using a tracking algorithm that we developed, it is possible to trace the history of each individual bubble during the ripening of the foam. Figure 9.1(a) is a representative example of the type of trajectories (in the (t, r) plane) that bubbles can follow. In order to smooth out the noise of the signal, and recover the general trend of $R(t)$ for each bubble, each trajectory is fitted with a 5th order polynomial. Extra constraints are added to enhance the quality of the fit: the initial value at $t = 0$ is set to the mean of the five first values of the measured $R(t)$, and the first derivative at $t = 0$ is set to 0 (ie. the degree-1 term is set to 0).

A large variability is observed in the type of history that each bubble can follow. Bubbles can immediately shrink and disappear, or keep the same radius for a certain time, before quickly shrinking and disappearing. On the contrary, other bubbles can immediately start to swell and reach a large radius at the end of the experiment, or

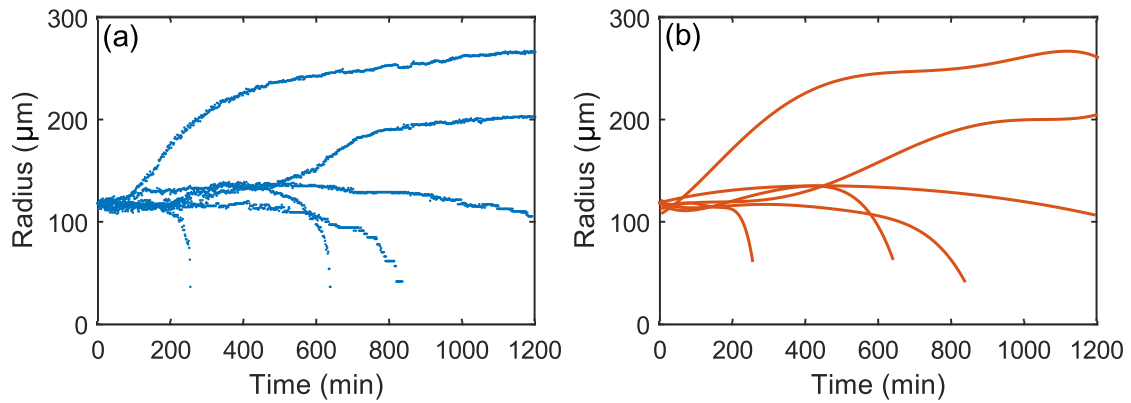


Figure 9.1: Evolution of the radius of six different bubbles as a function of time. (a) Raw data. (b) Polynomial fits.

others can start to swell after a certain lag time. Finally, some bubbles can even follow non monotonous pathes and swell at first, and then shrink back to their original size.

This large variety of behavior is very interesting and is most probably due to the fact that each bubble has its own micro-environment determined by its close neighbouring bubbles. It would therefore be interesting to study the correlation between the type of behavior observed, and the local environment of the considered bubble.

A first step toward this can be done by calculating the instantaneous rate of variation of each bubble's volume. Indeed, since a polynomial fit of all the bubbles trajectories is known, it is possible to compute the time derivative of the radius, \dot{R} , for each bubble, as a function of time. Once again, the resulting rates of variation, calculated for each bubble at each time, present a large variability, as shown on figure 9.2. The instantaneous volume variation of all the bubbles is plotted against their radius, at different times of the foam evolution. This volume variation was calculated as $\dot{V} = 4\pi R^2 \dot{R}$.

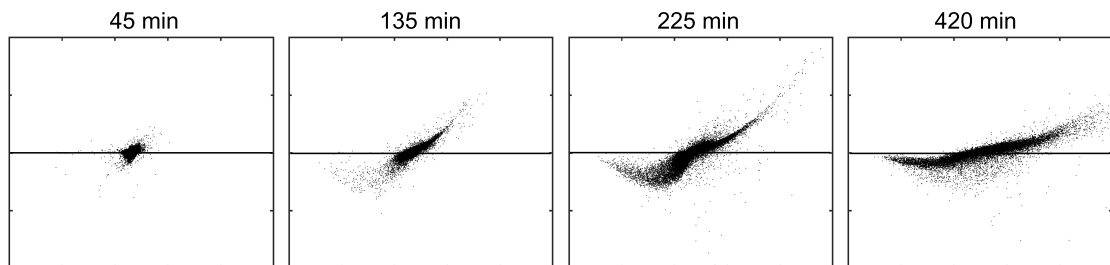


Figure 9.2: Instantaneous volume variation \dot{V} of the bubbles as a function of their radius, for different times. The axis for all panels are: x-axis, \dot{V} (-500 500 pL/min) y-axis, R (0-250 μm)

At the beginning, the volume variations are weak and all the points are gathered near the x-axis. But over time, an elongated shape develops, and crosses the x-axis (ie. $\dot{V} = 0$) at a value of R close to the mean bubble radius ($115\mu m$). This shape is in accordance with the general idea of Ostwald ripening: larger bubbles swell ($\dot{V} > 0$) while smaller bubbles shrink ($\dot{V} < 0$). However, the large scattering of the points suggest that the local environment should be taken into account, since bubbles with the same given radius can have very dispersed \dot{V} values.

9.2 Induced defect

We have seen that the nucleation-growth of random defects is at the origin of the foam destabilization. An idea would be to induce a size defect in a bubble at a given position, to study its subsequent growth. Numerical simulation have been performed on this problem [74].

A very localized heating of one bubble within the foam enables us to induce a very controlled defect in the foam. This heating is done by focusing an infrared laser within the channel [75], near the position of the desired defect, to slightly swell the bubble. The swelling volume is controlled by the heating time of the laser. Once this defect initiation is realised, the slightly larger bubble starts to draw gas from its first neighbours. The following propagation of disorder from this point can then be followed, as shown in figure 9.3. This could give a even more precise view of the disorder propagation, notably by investigating the effect of topological rearrangements as the sizes of the bubbles change.

9.3 Grain boundary

Using the two sets of injectors of the chamber at the same time, it is possible to produce bidisperse foams with two spatial domains of different mean radii, as shown in figure 9.4, thus creating a grain boundary in the foam. The evolution of the bubbles sizes can be measured as a function of their distance from the grain boundary, as shown in figure 9.4. It can be seen that the bubbles on the boundary between the two domains swell faster than the others. This is caused by the higher radius contrast between the bubbles of different sizes in direct contact at the grain boundary. It would be interesting to study how the disorder, that nucleated at the grain boundary, propagates into the two monodisperse domains.

Furthermore, on the last image in figure 9.4 at 83 min, the left region with smaller bubbles shows signs of destabilisation, according to the nucleation-growth mechanism studied in the previous chapter. Therefore, it exists a competition between this ho-

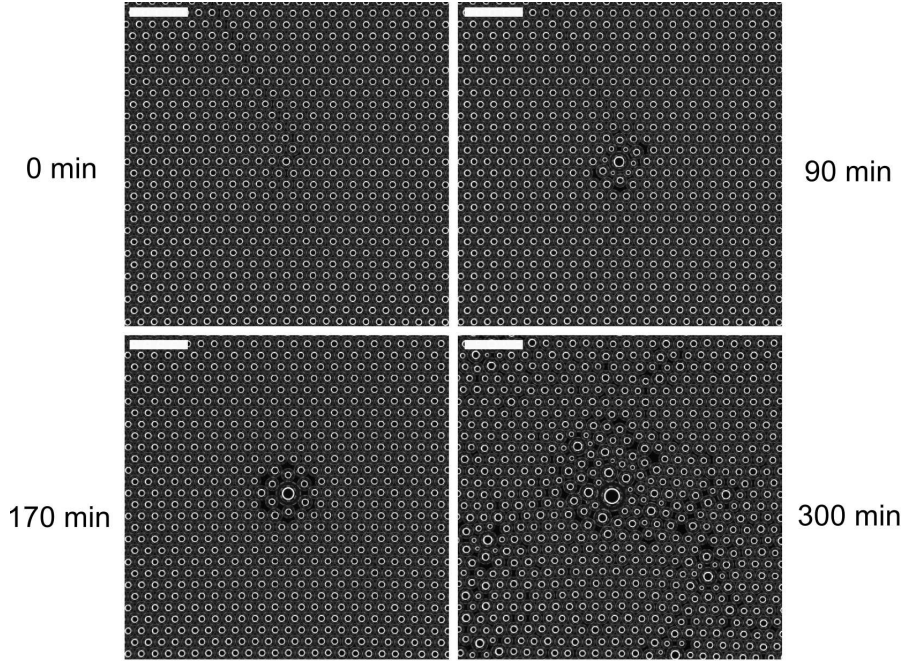


Figure 9.3: Evolution of a laser-induced foam defect. Scale bars are 1 mm.

mogeneous disorder nucleation, within a domain of given size, and the heterogeneous nucleation of disorder at the grain boundary. The ratio between the bubbles sizes of the two domains is probably the key factor that determines if homogeneous or heterogeneous disordering occurs first.

9.4 Further experiments

The microfluidic setup we developed gave us new insight into the physical mechanisms governing the destabilisation of a monodisperse foam. There are still valuable information to harvest from the experiments we have presented, but the very simple air-water-SDS composition used remains a model system. The next step would be to work with more complex physico-chemical formulations, akin to those used in real industrial applications.

Our system gives very precise informations on the destabilisation of a foam *via* Ostwald ripening. The first natural experiment to investigate would consequently be to observe the chemical formulations classically used to block Ostwald Ripening.

A common method to stop Ostwald ripening is to add a small amount of water-insoluble gas (typically a perfluorocarbon [76]) in the bubbles. The insoluble molecules stay in the bubbles and create an osmotic counter-pressure that can block Ostwald ripening. The idea would be to generate this type of foam in our system, to measure the

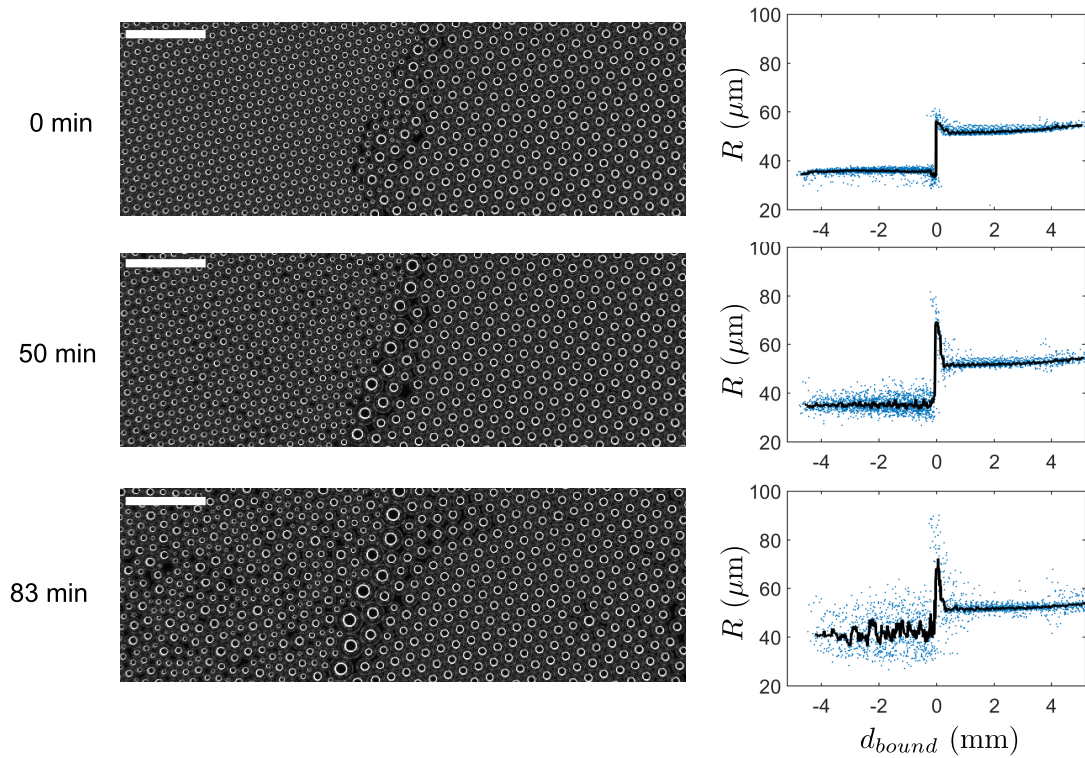


Figure 9.4: Successive steps of the evolution of a foam grain boundary. Scale bars on the micrographs are 1 mm. The plots on the right show the radii of the bubbles as a function of their distance from the grain boundary d_{bound} . The black line corresponds to the median-filtered points, with a window size of 10 samples.

minimal concentration of insoluble gas necessary to preserve the foam's ordered structure. Presumably, a very low concentration of insoluble gas may stop the evolution of the foam, but it could happen after the disorder invasion. Our system would thus allow to tune the concentration of blocking gas, as a function of the desired structural order of the final foam.

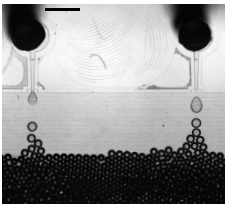
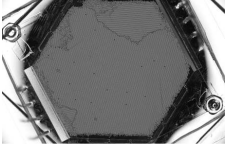
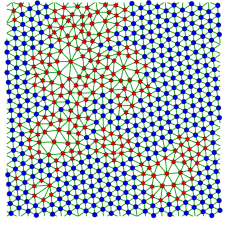
Another widely used stabilisation method against Ostwald ripening is to use surfactants presenting an interfacial elasticity [54]. The interfacial pressure from the adsorbed surfactant can be sufficient to generate a stress that blocks Ostwald ripening. Our system could provide a systematic method to measure the stabilisation efficiency of a surfactant formulation, simply by measuring to what extent the growth of disorder is prevented in the foam.

These experiments could easily be adapted to the study of liquid-liquid dispersion. A mere geometric adaptation and an increase of the optical magnification would be the only necessary modifications, since the droplets in an emulsion are generally smaller, of

the order of tens of microns.

Finally, we stated in section 6 that one of the interest of the study was to understand disorder growth, in order to prevent the structure alteration of a monodisperse liquid foam used as a precursor for a solid porous material. This could be directly tested *in situ*, in our system, by monitoring the simultaneous solidification/coarsening of a solidifying foam. We would be able to see how and when the solidification of the continuous phase stops the ripening and freezes the structure of the foam. The continuous matrix could be for example a gelifying aqueous solution, a polymerizing monomer mix, or a setting cement slurry.

Movies index

Movie7	 A grayscale micrograph of a microfluidic device. Two circular injectors at the top are shown. Bubbles are being generated at the junctions and are moving downwards into a larger chamber. The bottom of the chamber is filled with a dense layer of small, dark bubbles.	Generation of the bubbles at the injector and filling of the foam chamber.
Movie 8	 A grayscale micrograph showing a top-down view of a microfluidic chamber. The chamber is filled with a complex, interconnected network of dark lines representing the foam structure. The chamber has a hexagonal shape with rounded corners.	Evolution of the foam in the microfluidic chamber.
Movie 9	 A 2D visualization of a foam structure. The bubbles are represented as a collection of points. A Delaunay triangulation is overlaid on these points, with red lines connecting the vertices. The vertices are colored: red stars represent disordered bubbles, and blue disks represent ordered ones. The overall pattern is a complex, interconnected network of triangles.	Animation of the evolution of the Delaunay triangulation of the area zoomed in figure 8.4. The red stars are disordered bubbles, the blue disks are ordered ones.

General conclusion

The aim of this thesis was to gain new insights into the physics underlying the long-term stability, and instability, of liquid foams. Using the microfluidic tools at our disposal, we tackled this question using two very different, yet complementary, approaches.

In the first part, we went down to the smallest scale of a foam, by observing a single bubble. This brought a novel understanding to the very well known observation that a coating of solid particles can protect a bubble from dissolution [17]. We have precisely measured the mechanical properties of a particle armored bubble, and showed that its resistance to dissolution was only affected by the bubble radius, and not by the particles' size. These findings are of importance when designing particle-stabilized foams, because they guide the choice of the particles to use for a particular application.

In the second part, we studied the foam at a larger scale, by analyzing the evolution of a large population of identical bubbles. This monodisperse foam destabilizes through Ostwald ripening toward a well-known self-similar state. However, we have shown that the transient regime leading to that state is not homogeneous in space. It can be described as a disorder nucleation-growth process, which has a profound impact on the spatial structure of the foam. The model that we develop predicts how the disorder grows in the foam, which is a valuable asset in applications where an ordered organization of the bubbles is required.

This multiscale approach provides a global understanding of foam stabilization. Indeed, part II gives a comprehension of the driving mechanism of Ostwald ripening, while part II shed light on the physical mechanisms that counteract it. This double understanding provides keys to design innovative foams resisting coarsening.

Over the course of this PhD work, we designed a very versatile microfluidic device, which breaks down into two main structures. Firstly, the injector and the coating channel are dedicated to the production of complex objects (armored bubbles or droplets) the properties of which can be finely tuned by changing the geometry of the channel and the type of particles used. Secondly, the observation chamber enables the immobilization of the produced object, in a controlled environment, for long-term monitoring, using

various types of imaging systems. The size of this chamber can be adapted to observe a single bubble or droplet (as in part I), or a large number of objects (as in part II).

A microfluidic architecture combining the injector and coating channel from part I and the large observation chamber from part II would open possibilities to observe large populations of complex objects, coupled by strong interactions, down to the precision of a single object.

Such a setup could be used to monitor the ripening of a population of colloid-armored bubbles, in order to observe the arresting of Oswald ripening by the colloidal shells, and verify the conclusions that we drew on the stability of particles-stabilized foams in section 4.5. Namely, that the smallest bubbles buckle and disappear, and that the initial polydispersity of the foam is the key parameter which determines the fraction of bubbles that dissolve.

Finally, this system could be capable of producing and providing precise informations on what I would call 'living foams'. Indeed, in section 5.2.1, we mentioned the possibility of adsorbing bacteria on the interface of an air-in-water bubble. The potential system schemed in figure 9.5 produces bubbles using a wedged injector, which are then forced by a flow of bacterial suspension into coating channels. The bacteria-coated bubbles are then released in a culture chamber, where the foam can be observed.

A very interesting type of bacteria, that could be used in this system, was recently reported by Zhu *et al.* [77]. They genetically engineered a strain of *Synechocystis*, a type of cyanobacteria, so that it reduces carbon dioxide into ethylene, through a photosynthetic reaction. This reaction uses input energy from light and can be written as : $2\text{CO}_2 + 2\text{H}_2\text{O} \rightarrow \text{C}_2\text{H}_2 + 3\text{O}_2$. This type of reaction is extremely interesting because by it is a way of sequestering CO_2 and, by the same token, of producing ethylene, a highly energetic fuel, as well as dioxygen. Culturing these bacteria on a population of CO_2 bubbles, using the microchip described in figure 9.5, could provide an efficient way of producing ethylene from carbon dioxide, since the foam would greatly enhance the interface to volume ratio of the culture. Furthermore, such a biphasic bacterial culture would certainly exhibit very complex coupling between the bacterial growth, the gas consumption and production by the bacteria metabolism, and the gas exchanges by diffusion between the bubbles. The very precise monitoring enabled by our system, at a level of single bubbles, would certainly be very useful to unravel such complex interactions.

In conclusion, this microfluidic study of the interactions between fluid interfaces and bacterial colonies looks very promising not only for green chemistry and CO_2 sequestration, but it might also help to understand how marine plankton interacts with air bubbles, and for instance why the Sunshine Coast in Australia gets regularly flooded with foam, as described in the introduction.

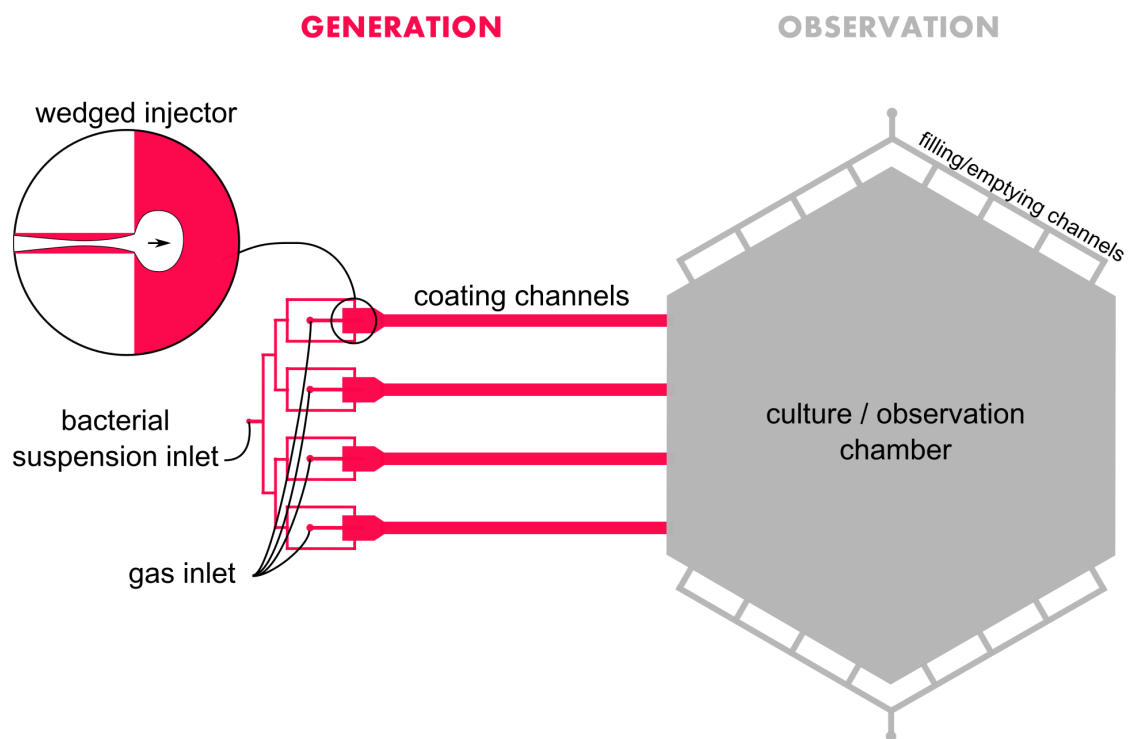


Figure 9.5: Skeeth of a potential microfluidic setup for a biphasic bacterial culture, or 'living foam'. The gas is injected through wedged injectors, and the bubbles formed are pushed toward the culture chamber by a flow of bacterial suspension.

Bibliography

- [1] COHEN-ADDAD S., HÖHLER R., & PITOIS O. Flow in foams and flowing foams. *Annual Review of Fluid Mechanics*, **45**(1):241, 2013
- [2] CAMPBELL G.M. & MOUGEOT E. Creation and characterisation of aerated food products. *Trends in Food Science and Technology*, **10**(9):283, 1999
- [3] EISNER M.D., WILDMOSER H., & WINDHAB E.J. Air cell microstructuring in a high viscous ice cream matrix. *Colloids and Surfaces A: Physicochemical and Engineering Aspects*, **263**(1):390, 2005
- [4] JOHNSON G.H. & HIGGINS R.C. Method of mixing cement composition, 1951
- [5] PETIT P., JAVIERRE I., JÉZÉQUEL P.H., & BIANCE A.L. Generation and stability of bubbles in a cement based slurry. *Cement and Concrete Research*, **60**:37, 2014
- [6] BANHART J. Manufacture, characterisation and application of cellular metals and metal foams. *Progress in Materials Science*, **46**(6):559, 2001
- [7] CANTAT I., COHEN-ADDAD S., ELIAS F., GRANER F., HÖHLER R., PITOIS O., ROUYER F., & SAINT-JALMES A. *Les Mousses : structure et dynamique*. Belin, 2010
- [8] TCHOLAKOVA S., DENKOV N.D., & LIPS A. Comparison of solid particles, globular proteins and surfactants as emulsifiers. *Physical Chemistry Chemical Physics*, **10**(12):1608, 2008
- [9] GONZENBACH U.T., STUDART A.R., TERVOORT E., & GAUCKLER L.J. Ultra-stable particle-stabilized foams. *Angewandte Chemie (International ed. in English)*, **45**(21):3526, 2006
- [10] VOORHEES P.W. The theory of Ostwald ripening. *Journal of Statistical Physics*, **38**(1-2):231, 1985

- [11] LAMBERT J., MOKSO R., CANTAT I., CLOETENS P., GLAZIER J.A., GRANER F., & DELANNAY R. Coarsening foams robustly reach a self-similar growth regime. *Physical Review Letters*, **104**(24):248304, 2010
- [12] PIERANSKI P. Two-dimensional interfacial colloidal crystals. *Physical Review Letters*, **45**(7):569, 1980
- [13] SHEPPARD E. & TCHEUREKDJIAN N. Monolayer studies. *Journal of Colloid and Interface Science*, **28**(3-4):481, 1968
- [14] AVEYARD R., CLINT J.H., NEES D., & PAUNOV V.N. Compression and structure of monolayers of charged latex particles at Air / Water and Octane / Water interfaces. *Langmuir*, **16**(4):1969, 2000
- [15] VELLA D., AUSSILLOUS P., & MAHADEVAN L. Elasticity of an interfacial particle raft. *Europhysics Letters*, **68**(2):212, 2004
- [16] MONTEUX C., KIRKWOOD J., XU H., JUNG E., & FULLER G.G. Determining the mechanical response of particle-laden fluid interfaces using surface pressure isotherms and bulk pressure measurements of droplets. *Physical chemistry chemical physics : PCCP*, **9**(48):6344, 2007
- [17] RAMSDEN W. Separation of solids in the surface-layer of solutions and suspensions. *Proceedings of the Royal Society of London*, **72**:156, 1903
- [18] SUBRAMANIAM A.B., ABKARIAN M., & STONE H.A. Controlled assembly of jammed colloidal shells on fluid droplets. *Nature materials*, **4**(7):553, 2005
- [19] PARK J.I., NIE Z., KUMACHEV A., ABDELRAHMAN A.I., BINKS B.P., STONE H.A., & KUMACHEVA E. A microfluidic approach to chemically driven assembly of colloidal particles at gas-liquid interfaces. *Angewandte Chemie International Edition*, **48**(29):5300, 2009
- [20] SUBRAMANIAM A.B., ABKARIAN M., MAHADEVAN L., & STONE H.A. Mechanics of interfacial composite materials. *Langmuir*, **22**(24):10204, 2006
- [21] ABKARIAN M., SUBRAMANIAM A.B., KIM S.H., LARSEN R., YANG S.M., & STONE H.A. Dissolution arrest and stability of particle-covered bubbles. *Physical Review Letters*, **99**(18):188301, 2007
- [22] TSAPIS N., DUFRESNE E., SINHA S., RIERA C., HUTCHINSON J., MAHADEVAN L., & WEITZ D. Onset of buckling in drying droplets of colloidal suspensions. *Physical Review Letters*, **94**(1):018302, 2005

- [23] GARBIN V., CROCKER J.C., & STEBE K.J. Forced desorption of nanoparticles from an oil water interface. *Langmuir*, **28**(3):1663, 2011
- [24] LABORIE B., LACHAUSSÉE F., LORENCEAU E., & ROUYER F. How coatings with hydrophobic particles may change the drying of water droplets: incompressible surface versus porous media effects. *Soft Matter*, **9**(19):4822, 2013
- [25] LAGUBEAU G., RESCAGLIO A., & MELO F. Armoring a droplet: soft jamming of a dense granular interface. *Physical Review E*, **90**(3):030201, 2014
- [26] STOCCO A., RIO E., BINKS B.P., & LANGEVIN D. Aqueous foams stabilized solely by particles. *Soft Matter*, **7**(4):1260, 2011
- [27] STOCCO A., DRENCKHAN W., RIO E., LANGEVIN D., & BINKS B.P. Particle-stabilised foams: an interfacial study. *Soft Matter*, **5**(11):2215, 2009
- [28] BINKS B.P. & MURAKAMI R. Phase inversion of particle-stabilized materials from foams to dry water. *Nature materials*, **5**(11):865, 2006
- [29] BINKS B.P. & HOROZOV T.S. Aqueous foams stabilized solely by silica nanoparticles. *Angewandte Chemie*, **117**(24):3788, 2005
- [30] FUJII S., IDDON P.D., RYAN A.J., & ARMES S.P. Aqueous particulate foams stabilized solely with polymer latex particles. *Langmuir*, **22**(18):7512, 2006
- [31] DELEURENCE R., PARNEIX C., & MONTEUX C. Mixtures of latex particles and the surfactant of opposite charge used as interface stabilizers - influence of particle contact angle, zeta potential, flocculation and shear energy. *Soft Matter*, **10**(36):7088, 2014
- [32] DANGLA R., LEE S., & BAROUD C.N. Trapping microfluidic drops in wells of surface energy. *Physical Review Letters*, **107**(12):124501, 2011
- [33] DANGLA R., KAYI S.C., & BAROUD C.N. Droplet microfluidics driven by gradients of confinement. *Proceedings of the National Academy of Sciences (PNAS)*, **110**(3):853, 2013
- [34] DUFFY D.C., McDONALD J.C., SCHUELLER O.J.A., & WHITESIDES G.M. Rapid prototyping of microfluidic systems in poly(dimethylsiloxane). *Analytical chemistry*, **70**(23):4974, 1998
- [35] KIM J., CHAUDHURY M.K., OWEN M.J., & ORBECK T. The mechanisms of hydrophobic recovery of polydimethylsiloxane elastomers exposed to partial electrical discharges. *Journal of Colloid and Interface Science*, **244**(1):200, 2001

- [36] EDDINGTON D.T., PUCCINELLI J.P., & BEEBE D.J. Thermal aging and reduced hydrophobic recovery of polydimethylsiloxane. *Sensors and Actuators B: Chemical*, **114**(1):170, 2006
- [37] THORSEN T., ROBERTS R.W., ARNOLD F.H., & QUAKE S.R. Dynamic pattern formation in a vesicle-generating microfluidic device. *Physical Review Letters*, **86**(18):4163, 2001
- [38] ANNA S.L., BONTOUX N., & STONE H.A. Formation of dispersions using "flow focusing" in microchannels. *Applied Physics Letters*, **82**(3):364, 2003
- [39] TABELING P. *Introduction à la microfluidique*. Collection "Échelles". Belin, 2003
- [40] HO C.C., KELLER A., ODELL J.A., & OTTEWILL R.H. Preparation of monodisperse ellipsoidal polystyrene particles. *Colloid & Polymer Science*, **271**(5):469, 1993
- [41] ZOUESHTIAGH F., BAUDOIN M., & GUERRIN D. Capillary tube wetting induced by particles: towards armoured bubbles tailoring. *Soft matter*, **10**(47):9403, 2014
- [42] KOTULA A.P. & ANNA S.L. Probing timescales for colloidal particle adsorption using slug bubbles in rectangular microchannels. *Soft Matter*, **8**(41):10759, 2012
- [43] COLOSQUI C.E., MORRIS J.M., & STONE H.A. Hydrodynamically-driven colloidal assembly in the thin-film entrainment regime. *Physical Review Letter*, **110**(18):188302, 2013
- [44] PITOIS O., BUISSON M., & CHATEAU X. On the collapse pressure of armored bubbles and drops. *The European Physical Journal E*, **38**(5):48, 2015
- [45] BOTTO L., LEWANDOWSKI E.P., CAVALLARO M., & STEBE K.J. Capillary interactions between anisotropic particles. *Soft Matter*, **8**(39):9957, 2012
- [46] LEHLE H., NORUZIFAR E., & OETTEL M. Ellipsoidal particles at fluid interfaces. *European Physical Journal E*, **26**(1-2):151, 2008
- [47] MADIVALA B., VANDEBRIL S., FRANSAER J., & VERMANT J. Exploiting particle shape in solid stabilized emulsions. *Soft Matter*, **5**(8):1717, 2009
- [48] TAJIMA K. The effect of salt on the adsorption of sodium dodecyl sulfate. *Bulletin of the Chemical Society of Japan*, **44**:1767, 1971
- [49] BINKS B.P. & RODRIGUES J.A. Enhanced stabilization of emulsions due to surfactant-induced nanoparticle flocculation. *Langmuir*, **23**(14):7436, 2007

- [50] WARD C., BALAKRISHNAN A., & HOOPER F. On the thermodynamics of nucleation in weak gas-liquid solutions. *Journal of Basic Engineering*, **92**(4):695, 1970
- [51] LANDAU L.D. & LIFSHITZ I.M. *Statistical Physics*. Addison-we edition, 1958
- [52] PRIGOGINE I. & DEFAY R. *Chemical Thermodynamics*. Longman gr edition, 1965
- [53] LEMLICH R. Prediction of changes in bubble size distribution due to interbubble gas diffusion in foam. *Industrial & Engineering Chemistry Fundamentals*, **17**(2):89, 1978
- [54] TCHOLAKOVA S., MITRINOVA Z., GOLEMANOV K., DENKOV N.D., VETHAMUTHU M., & ANANTHAPADMANABHAN K.P. Control of Ostwald ripening by using surfactants with high surface modulus. *Langmuir*, **27**(24):14807, 2011
- [55] LANDAU L.D. & LIFSHITZ I.M. *Theory of elasticity*. Pergamon p edition, 1986
- [56] POGORELOV A. *Bending of surfaces and stability of shells*. American m edition, 1988
- [57] KRALCHEVSKY P.A., IVANOV I.B., ANANTHAPADMANABHAN K.P., & LIPS A. On the thermodynamics of particle-stabilized emulsions: Curvature effects and catastrophic phase inversion. *Langmuir*, **21**(1):50, 2005
- [58] LEWANDOWSKI E.P., CAVALLARO M., BOTTO L., BERNATE J.C., GARBIN V., & STEBE K.J. Orientation and self-assembly of cylindrical particles by anisotropic capillary interactions. *Langmuir*, **26**(19):15142, 2010
- [59] CAVALLARO M., BOTTO L., LEWANDOWSKI E.P., WANG M., & STEBE K.J. Curvature-driven capillary migration and assembly of rod-like particles. *Proceedings of the National Academy of Sciences of the United States of America*, **108**(52):20923, 2011
- [60] ROSSI L., SACANNA S., IRVINE W.T.M., CHAIKIN P.M., PINE D.J., & PHILIPSE A.P. Cubic crystals from cubic colloids. *Soft Matter*, **7**(9):4139, 2011
- [61] HEAD I.M., JONES D.M., & RÖLING W.F.M. Marine microorganisms make a meal of oil. *Nature reviews. Microbiology*, **4**(3):173, 2006
- [62] DRENCKHAN W. & LANGEVIN D. Monodisperse foams in one to three dimensions. *Current Opinion in Colloid and Interface Science*, **15**(5):341, 2010
- [63] MARMOTTANT P. & RAVEN J.P. Microfluidics with foams. *Soft Matter*, **5**(18):3385, 2009

- [64] BARBETTA A., GUMIERO A., PECCI R., BEDINI R., & DENTINI M. Gas-in-liquid foam templating as a method for the production of highly porous scaffolds. *Biomacromolecules*, **10**(12):3188, 2009
- [65] STAVANS J. The evolution of cellular structures. *Reports on Progress in Physics*, **56**(6):733, 1993
- [66] MULLINS W.W. The statistical self-similarity hypothesis in grain growth and particle coarsening. *Journal of Applied Physics*, **59**(4):1341, 1986
- [67] GLAZIER J.A., GROSS S.P., & STAVANS J. Dynamics of two-dimensional soap froths. *Physical Review A*, **36**(1):306, 1987
- [68] RUSKIN H. & FENG Y. Scaling properties for ordered/disordered 2-D dry froths. *Physica A: Statistical Mechanics and its Applications*, **230**(3-4):455, 1996
- [69] DUPLAT J., BOSSA B., & VILLERMAUX E. On two-dimensional foam ageing. *Journal of Fluid Mechanics*, **673**:147, 2011
- [70] LIFSHITZ I. & SLYOZOV V. The kinetics of precipitation from supersaturated solid solutions. *Journal of Physics and Chemistry of Solids*, **19**(1-2):35, 1961
- [71] BRAY D.J., GILMOUR S.G., GUILD F.J., & TAYLOR A.C. Quantifying nanoparticle dispersion by using the area disorder of Delaunay triangulation. *Journal of the Royal Statistical Society: Series C (Applied Statistics)*, **61**(2):253, 2012
- [72] OTSU N. A threshold selection method from gray-level histograms. *IEEE Transactions on Systems, Man, and Cybernetics*, **9**(1):62, 1979
- [73] GELUCK P. *La marque du chat*. Casterman edition, 2007
- [74] TAM W. Evolution of a single defect in an ideal two-dimensional hexagonal soap froth. *Physical Review E*, **58**(6):8032, 1998
- [75] CORDERO M., VERNEUIL E., GALLAIRE F., & BAROUD C.N. Time-resolved temperature rise in a thin liquid film due to laser absorption. *Physical Review E*, **79**(1):011201, 2009
- [76] WEBSTER A.J. & CATES M.E. Osmotic Stabilization of Concentrated Emulsions and Foams. *Langmuir*, **17**(3):595, 2001
- [77] ZHU T., XIE X., LI Z., TAN X., & LU X. Enhancing photosynthetic production of ethylene in genetically engineered *Synechocystis* sp. PCC 6803. *Green Chem.*, **17**(1):421, 2015